Hydrogen effects on the mechanical behaviour of FeCr alloys investigated by in-situ nanoindentation

Dissertation

zur

Erlangung des Grades

Doktor-Ingenieurin

der

Fakultät für Maschinenbau

der Ruhr-Universität Bochum

von

Jing Rao

aus

Jiangxi, China

Bochum, 2023

Dissertation eingereicht am: 09.August.2023

Tag der mündlichen Prüfung: 12.October.2023

Erstgutachter: Prof. Gerhard Dehm

Zweitgutachter: Prof. Astrid Pundt

AFFIDAVIT

I declare in lieu of oath, that I wrote this thesis myself, using only
literature cited in this volume.

08.08.2023

Datum

Rao Jing 瑶

Unterschrift

CRediT author statement

The following manuscripts are embedded in this thesis:

Manuscript 1

Diffusible hydrogen and its impact on nanohardness and dislocation structure in FeCr alloys by *in situ* nanoindentation

Jing Rao: Conceptualization, Methodology, Investigation (*in situ* backside hydrogen loading frontside nanoindentation experiments, SEM, AFM, EBSD, TEM, STEM, ECCI), Formal analysis, Writing – original draft, Writing - review and editing. Subin Lee: Investigation (TEM and STEM), Formal analysis, Writing - review and editing. Eberhard Heinen: Investigation (XPS experiments). Gerhard Dehm: Conceptualization, Writing - review and editing, Supervision. María Jazmin Duarte: Conceptualization, Methodology, Writing - review and editing, Supervision.

Manuscript 2

The effect of microstructural features on the hydrogen diffusion coefficient in ferritic FeCr alloys: a comparison between the Kelvin probe based potentiometric hydrogen electrode method and a nanohardness based method

Jing Rao: Conceptualization, Methodology, Investigation (*in situ* backside hydrogen loading frontside nanoindentation experiments, SEM, EBSD, ECCI), Formal analysis, Writing – original draft, Writing - review and editing. Binhan Sun: Investigation (TDS experiments), Writing - review and editing. Chun-Hung Wu: Investigation (KP-based permeation experiments), Formal analysis. Arulkumar Ganapathi: Investigation (KP-based permeation experiments), Formal analysis. Xizhen Dong: Investigation (TDS experiments), Writing - review and editing. Michael Rohwerder: Conceptualization, Methodology, Writing - review and editing. Gerhard Dehm: Conceptualization, Writing - review and editing, Supervision. María Jazmin Duarte: Conceptualization, Methodology, Writing - review and editing, Supervision.

Manuscript 3

Hydrogen-induced strain hardening effect in ferritic Fe-21Cr alloy (100) orientation with different dislocation density by *in situ* micropillar compression technique

Jing Rao: Conceptualization, Methodology, Investigation (*in situ* backside pillar compression experiments, SEM, EBSD, ECCI), Formal analysis, Writing – original draft, Writing - review and editing. Binhan Sun: Investigation (TDS experiments), Writing - review and editing. Alexandra Vogel: Investigation (SKPFM experiments). Nicolas Peter: Pillar used for SKPFM fabrication. Gerhard Dehm: Conceptualization, Writing - review and editing, Supervision. María Jazmin Duarte: Conceptualization, Methodology, Writing - review and editing, Supervision.

Manuscript 4

Hardening relationship with hydrogen and dislocation structure evolution in FeCr alloys by *in situ* nanoindentation scratch across the Σ3 grain boundary

Jing Rao: Conceptualization, Methodology, Investigation (*in situ* backside scratch experiments, SEM, EBSD, ECCI, confocal microscopy), Formal analysis, Writing – original draft, Writing - review and editing. Katja Angenendt: Investigation (TKD experiments). Gerhard Dehm: Conceptualization, Writing - review and editing, Supervision. María Jazmin Duarte: Conceptualization, Methodology, Writing - review and editing, Supervision.

Acknowledgements

encouragement.

The most profound gratitude goes to my family members. The challenging yet joyful journey of discovery in Germany would be impossible without my father, Nengshun Rao, and my mother, Huixiu Wang. I have been overseas for years and due to the pandemic, I haven't seen them in person for more than three years. It is incredibly hard for them to understand the reason for sticking to this PhD dream as they barely see any researchers around. However, mainly out of trust and unconditional love, they support me as always. I could not express more gratitude to Fuhui Shen, my husband. Having him in my life is my most incredible fortune and luck. During my PhD, he shuttled between Aachen and Düsseldorf by train almost every day. The morning star and the evening mist witness our love. Finally, and most importantly, Linkun Shen, the sunshine of my life. My precious little boy gives me the ultimate courage and determination to overcome all the challenges and potholes. I hope he can live a life without regrets.

From an innocent girl who does not know how to take care of herself to a mom who needs to take care of her baby, PhD for me is not only about the theories and experiments but more about learning how to become a more complete and independent soul. Finishing the PhD is the beginning of a new chapter of my life. No matter what waits ahead, I am ready.

Abbreviations

AFM	Atomic force microscopy
AES	Auger electron spectroscopy
AIDE	Adsorption-induced dislocation emission
APT	Atom probe tomography
BCC	Body centered cubic
BSE	Backscattered electron
CR	Cold rolling
CRSS	Critical resolved shear stress
CSM	Continuous stiffness method
defactant	Defect acting agent
DFT	Density function theory
DS	Davanathan-starchurski
EBSD	Electron backscatter diffraction
ECCI	Electron channeling contrast imaging
ECNI	Electrochemical nanoindentation
EDS/EDX	Energy-dispersive X-ray spectroscopy
EELS	Electron energy loss spectroscopy
EELS	Electron energy loss spectroscopy
FCC	Face centered cubic
FEM	Finite element modelling
GND	Geometry necessary dislocation
HCP	Hexagonal close packing
HD	High dislocation
HE	Hydrogen embrittlement
HEDE	Hydrogen-enhanced decohesion

HELP	Hydrogen-enhanced local plasticity
HER	Hydrogen evolution reaction
HESIV	Hydrogen-enhanced strain-induced vacancies
HIC	Hydrogen-induced crack
HIE	Hydride-induced embrittlement
HMT	Hydrogen microprint technique
HPT	High-pressure torsion
KAM	Kernel average of misorientations
KP	Kelvin probe
LD	Low dislocation
LG	Large grain
LME	Liquid-metal embrittlement
MD	Molecular dynamics
MG	Medium grain
PAS	Positron annihilation spectroscopy
PCTFE	Polychlorotrifluoroethylene
PFIB	Plasma focused ion beam
SE	Secondary electrons
SEM	Scanning electron microscopy
SG	Small grain
SIMS	Secondary ion massspectroscopy
SKPFM	Scanning Kelvin probe force microscopy
SSC	Sulfide stress cracking
SSD	Statistically stored dislocation
STEM	Scanning transmission electron microscopy
TDA	Thermal desorption analysis
TDS	Thermal desorption spectroscopy

TEM	Transmission electron microscope
TKD	Transmission Kikuchi diffraction
TPD	Temperature programmed desorption
TWIP	Twinning-Induced Plasticity steel
WDS	Wavelength-dispersive X-ray spectroscopy
WECs	White-etching-cracks
XPS	X-ray photoelectron spectroscopy
ZA	Zone axis

Nomenclature

A	Evaluated area
α	Empirical constant
a_0	Lattice constant
a_{PZ}	Radius of the plastic zone
a_c	Radius of the contact zone
C	Tabor's factor
C_0	Original concentration
$c(H_{Pd})$	Hydrogen concentration in Pd
D	Diffusion coefficient
D_{app}	Apparent hydrogen diffusion coefficient
D_{mix}	Mixed hydrogen diffusion coefficient
d	Distance of two diffraction points
E	Elastic modulus
E_a	Activation energy
E_{bp}	Binary phase/reference potential
$E_{SHE}^{*'}$	Standard hydrogen electrode potential

$\dot{\varepsilon}$	Strain rate
ε	Strain
f	Ratio between the radius of the plastic zone and the contact area
G	Shear stress
$\varGamma_H$	Formation energy of hydrogen
H	Hardness
$\varDelta H$	Hardness variation
H_0	Original hardness
H_i	Final hardness
H_{abs}	Hydrogen absorbed on the metal surface
H_{ads}	Hydrogen adsorbed on the metal surface
$\dot{h}$	Depth rate
i	Current density
I_0	Integral of zero-loss peak counts
I_t	The integral of total spectrum counts
J	J integral
k	Slope
K	Constant
l	Total length of dislocations
L	Length for hydrogen permeation
λ	Inelastic mean free paths
m	Mass
M	Taylor factor
μ_H	Chemical potential of hydrogen
n	Strain hardening exponent
n_H	Number of hydrogen
v	Poisson's ratio

P	Hydrogen gas pressure
$Pmax$	Maximum load point
$P_H{}^2$	Partial pressure of hydrogen gas
$\dot{P}$	Load rate
ρ	The density of the defect per volume
ρ_{dis}	Dislocation density
ρ_{GND}	Geometrically necessary dislocation density
ρ_{SSD}	Statistically stored dislocation density
rpl	Plastic zone size
θ	Tip angle
σy	Yield strength
σ_{Taylor}	Taylor's stress
σ_{Fric}	Lattice friction
T	Temperature
t_f	Thickness of TEM foil
t_{lag}	Lag time
V	Volume
V_{Ref}	Potential with respect to the reference electrode
x	Position
Ze	Electron charge

Abstract

This work aims to shed light on the underlying mechanism of hydrogen embrittlement, a critical issue for metallic materials in industries that rely on hydrogen storage, transportation, and application. Here we focus on investigating the mechanical response and microstructural evolution of single-phase ferritic model alloys to hydrogen by using a novel *in situ* backside electrochemically nanoindentation setup, enabling nanoindentation-related mechanical tests to be conducted during hydrogen charging. As the top surface of the specimen examined by mechanical experiment is not contaminated by the corrosive electrolyte after hydrogen charging, post-mortem microstructural characterizations by different techniques are feasible.

We first performed the *in situ* nanoindentation tests with Berkovich diamond tip in three ferritic alloys of Fe-4Al, Fe-16Cr and Fe-21Cr to investigate the effect of diffusible and lightly trapped hydrogen (i.e. mobile hydrogen). A hardening effect exhibits a specific dynamic tendency for the initial transient charging and the hydrogen release stages are discerned, while the Young's modulus remains constant. The increase in hardness follows the sigmoidal curve corresponding to the diffusion behavior of hydrogen which permeates through the specimen and can be well-fitted to the model based on the non-steady state. Besides, the hardness increases linearly with increasing hydrogen content until a quasi-equilibrium state between hydrogen absorption and desorption is reached. Above this transient region, the slope of the absolute hardness experiences a drastic decrease and hardness remains on a constant level. The hardness variation for a given composition is orientation dependent as determined for (100), (110) and (111) oriented grains. Higher content of Cr results in a more pronounced hardening effect within (100) orientation: a 16.7 % hardness increase is observed in Fe-21Cr, while Fe-16Cr, shows an increment of 10.8 %. A Fe-4Al alloy increases slightly in hardness by only 4.3 % at the applied current density of 3 mA/cm^2. The hardening effect is caused by an enhancement in dislocation density in the hydrogen charged condition during nanoindentation. This is revealed in the cross-section underneath the nanoindentation imprints by the bright field scanning transmission electron microscope (STEM). Applying the measured dislocation density and the plastic region evaluated from the electron channelling contrast image (ECCI) to the elastoplastic range of the load-displacement curve, an increase of 50 MPa in the lattice friction caused by the hydrogen is found. This study suggests that hydrogen initially facilitates dislocation nucleation following the "defactant" concept; afterwards, Cottrell clouds form and increase the resistance force for dislocation propagation according to the solute drag theory.

The Kelvin probe (KP)-based potentiometric hydrogen electrode method was performed to investigate the hydrogen diffusion coefficient on ferritic FeCr alloys with different chromium content, dislocation density, and grain size. The measured hydrogen diffusion coefficients are classified into apparent and mixed diffusion coefficients depending on whether deep hydrogen traps are involved. The nanohardness-based diffusion coefficients obtained from the *in situ* backside hydrogen loading frontside nanoindentation setup are $(3.12\pm0.04)\times10^{-6}$ cm^2/s for Fe-16Cr with large grain (LG) size $(1.13\pm0.09$ mm) and low dislocation (LD) density $(2.6\times10^{12}$ m$^{-2})$, higher than $(1.79\pm0.01)\times10^{-6}$ cm^2/s for Fe-21Cr with also large grain size $(1.05\pm0.05$ mm) and low dislocation density $(2.4\times10^{12}$ m$^{-2})$. The nanohardness-based diffusion coefficients are comparable to the diffusion coefficients acquired from the KP-based potentiometric hydrogen electrode method of $(5.98\pm0.11)\times10^{-6}$ cm^2/s for Fe-16Cr (LG, LD) and $(3.64\pm0.03)\times10^{-6}$ cm^2/s for Fe-21Cr (LG, LD), verifying the viability of this apparatus in measuring the mechanical properties and hydrogen diffusion coefficient simultaneously. Combined with the thermal desorption spectroscopy (TDS) measurements, the dislocation density, grain boundaries and Cr atoms introduced interstitials are proposed to be the reversible hydrogen trapping sites.

By micropillar compression tests performed with the *in situ* backside hydrogen setup, the enhancement of apparent strain hardening rate in Fe-21Cr-HD with high dislocation (HD) density $(8.7\times10^{13}$ m$^{-2})$ is 6.2 ± 1.4 GPa, around three times the Fe-21Cr-LD with low dislocation (LD) density $(1.3\times10^{12}$ m$^{-2})$ of 1.8 ± 0.9 GPa in the strain range of 0.02 to 0.03. As quantified by TDS measurements, the uptake of hydrogen by Fe-21Cr-HD is about three times (22.60 at.ppm) that of Fe-21Cr-LD (6.58 at.ppm). The scanning Kelvin probe force microscopy (SKPFM) potential mapping on the pillar surface confirmed the existence of sufficient hydrogen in pillars during cathodic hydrogen charging. In alloys with lower dislocation density, the strain is compensated by several slip lines that are visible on the pillar surface with its barrel shape instead of one sharp slip band in the hydrogen-charged pillar. In alloys with higher dislocation density, the micropillar exposed to hydrogen exhibits more slip traces than the H-free reference samples.

As a means of gaining a better understanding of hydrogen impact on the grain boundary, the nanoscratch experiments were performed in reversible directions perpendicular to the Σ3 grain boundary. Combined with the confocal microscopy analysis of the lateral profile, a hydrogen-induced hardening effect consistent with the previous nanoindentation and micropillar compression tests was observed. The wear tracks affected by hydrogen exhibit a higher slip trace density than the reference condition as noticed in the vicinity of the grain boundary. A

more extensive deformation region confined within a smaller plasticity region was discerned through transmission Kikuchi diffraction (TKD) analysis. The reduction in the shift distance of the grain boundary during hydrogen charging compared to the reference condition is postulated to stem from the locking effect of hydrogen, which retards the mobility of the $\Sigma 3$ grain boundary.

Kurzfassung

Diese Arbeit soll den zugrundeliegenden Mechanismus der Wasserstoffversprödung beleuchten, ein kritisches Problem für metallische Werkstoffe in Branchen, die auf die Speicherung, den Transport und die Anwendung von Wasserstoff angewiesen sind. Hier konzentrieren wir uns auf die Untersuchung der mechanischen Reaktion und der mikrostrukturellen Entwicklung von einphasigen ferritischen Modelllegierungen auf Wasserstoff unter Verwendung eines neuartigen *in situ* elektrochemischen Nanoindentationsaufbaus auf der Rückseite, der es ermöglicht, mechanische Tests im Zusammenhang mit Nanoindentation während der Wasserstoffbeladung durchzuführen. Da die Oberfläche der mechanisch untersuchten Probe nach der Wasserstoffbeladung nicht durch den korrosiven Elektrolyten verunreinigt wird, ist eine post-mortem mikrostrukturelle Charakterisierung mit verschiedenen Techniken möglich.

Zunächst führten wir *in situ* Nanoindentationstests mit einer Berkovich-Diamantspitze an drei ferritischen Legierungen (Fe-4Al, Fe-16Cr und Fe-21Cr) durch, um die Auswirkungen von diffundierenden und leicht eingeschlossenem Wasserstoff (d. h. mobilem Wasserstoff) zu untersuchen. Es wird ein Verfestigungseffekt mit einer spezifischen dynamischen Tendenz für die anfängliche transiente Aufladung und die Wasserstofffreisetzungsphasen festgestellt, während der Elastizitätsmodul konstant bleibt. Der Härteanstieg folgt einer sinusförmigen Kurve, die dem Diffusionsverhalten des Wasserstoffs durch die Probe entspricht und sich gut in das auf dem nicht-stationären Zustand basierenden Modell anpassen lässt. Außerdem steigt die Härte mit zunehmendem Wasserstoffgehalt linear an, bis ein Quasi-Gleichgewichtszustand zwischen Wasserstoffabsorption und -desorption erreicht ist. Oberhalb dieses Übergangsbereichs nimmt die Steigung der absoluten Härte drastisch ab und bleibt annähernd konstant. Die Härtevariation für eine bestimmte Zusammensetzung ist orientierungsabhängig, wie für (100), (110) und (111) orientierte Körner festgestellt wurde. Ein höherer Cr-Gehalt führt zu einem ausgeprägteren Härtungseffekt innerhalb der (100)-Orientierung: bei Fe-21Cr wird ein Härteanstieg von 16,7 % beobachtet, während Fe-16Cr einen Zuwachs von 10,8 % aufweist. Bei einer Fe-4Al-Legierung steigt die Härte bei einer Stromdichte von 3 mA/cm^2 nur geringfügig um 4,3 % an. Der Härtungseffekt wird durch eine Erhöhung der Versetzungsdichte während der Nanoindentation unter Wasserstoffbeladung verursacht. Dies konnte im Querschnitt unterhalb der Nanoindentationseindrücke mit dem Hellfeld-Rastertransmissionselektronenmikroskop (STEM) sichtbar gemacht werden. Wendet man die gemessene Versetzungsdichte und den aus dem Elektronen-channelling-Kontrastbild (ECCI)

ermittelten plastischen Bereich auf den elastoplastischen Bereich der Last-Verschiebungskurve an, so ergibt sich eine Erhöhung der durch den Wasserstoff verursachten Gitterreibung um 50 MPa. Diese Studie deutet darauf hin, dass Wasserstoff zunächst die Versetzungskeimbildung nach dem "Defactant"-Konzept erleichtert; anschließend bilden sich Cottrell-Wolken und erhöhen die Widerstandskraft für die Versetzungsausbreitung nach der Solute-Drag-Theorie.

Mit der potentiometrischen Wasserstoff-Elektroden-Methode auf Kelvin-Sonden-Basis wurde der Wasserstoff-Diffusionskoeffizient an ferritischen FeCr-Legierungen mit unterschiedlichem Chromgehalt, Versetzungsdichte und Korngröße untersucht. Die gemessenen Wasserstoffdiffusionskoeffizienten werden in scheinbare und gemischte Diffusionskoeffizienten unterteilt, je nachdem, ob tiefe Wasserstoffsenken beteiligt sind. Die auf der Nanohärte basierenden Diffusionskoeffizienten, die mit dem In-situ-Nanoindentationsaufbau auf der Rückseite ermittelt wurden, betragen $(3,12\pm0,04)\times10^{-6}$ cm^2/s für Fe-16Cr mit großer Korngröße (LG) $(1,13\pm0.09$ mm) und niedriger Versetzungsdichte (LD) $(2,6\times10^{12}$ m$^{-2})$, höher als $(1,79\pm0,01)\times10^{-6}$ cm^2/s für Fe-21Cr mit ebenfalls großer Korngröße $(1,05\pm0,05$ mm) und niedriger Versetzungsdichte $(2,4\times10^{12}$ m$^{-2})$. Die auf der Nanohärte basierenden Diffusionskoeffizienten sind vergleichbar mit den Diffusionskoeffizienten, die mit der potentiometrischen Wasserstoff-Elektroden-Methode auf KP-Basis ermittelt wurden: $(5,98\pm0,11)\times10^{-6}$ cm^2/s für Fe-16Cr (LG, LD) und $(3,64\pm0,03)\times10^{-6}$ cm^2/s für Fe-21Cr (LG, LD). Dies bestätigt die Eignung dieses Messaufbaus zur gleichzeitigen Messung der mechanischen Eigenschaften und des Wasserstoffdiffusionskoeffizienten. In Verbindung mit den Messungen der thermischen Desorptionsspektroskopie (TDS) werden die Versetzungsdichte, die Korngrenzen und die in die Zwischengitterplätze eingebrachten Cr-Atome als reversible Wasserstoffeinfangstellen vorgeschlagen. Durch Mikropillardruckversuche, die mit dem *in situ* Wasserstoffaufbau auf der Rückseite durchgeführt wurden, beträgt die Erhöhung der Verfestigungsrate in Fe-21Cr-HD mit hoher Versetzungsdichte $(8,7\times10^{13}$ m$^{-2})$ $6,2\pm1,4$ GPa, etwa das Dreifache von Fe-21Cr-LD mit niedriger Versetzungsdichte $(1,3\times10^{12}$ m$^{-2})$ von $1,8\pm0,9$ GPa im Verformungsbereich von 0.02 bis 0.03. Wie durch TDS-Messungen quantifiziert, ist die Wasserstoffaufnahme von Fe-21Cr-HD etwa dreimal so hoch (22,60 at.ppm) wie die von Fe-21Cr-LD (6,58 at.ppm). Die Rasterkraftmikroskopie mit Kelvinsonde (SKPFM) an der Säulenoberfläche bestätigte die Existenz von ausreichend Wasserstoff in den Säulen während der kathodischen Wasserstoffbeladung.

In Legierungen mit geringerer Versetzungsdichte entstehen bei der Verformung viele

Gleitlinien, die auf der tonnenförmigen Oberfläche der Säule sichtbar sind, anstatt durch ein scharfes Gleitband in der wasserstoffbeladenen Säule. In Legierungen mit höherer Versetzungsdichte weist die mit Wasserstoff beladene Mikrosäule mehr Gleitspuren auf als die H-freien Referenzproben.

Um die Auswirkungen des Wasserstoffs auf die Korngrenze besser zu verstehen, wurden die Nanoscratch-Experimente in reversiblen Richtungen senkrecht zur Σ3-Korngrenze durchgeführt. In Kombination mit der konfokalen Mikroskopanalyse des lateralen Profils wurde ein wasserstoffinduzierter Härtungseffekt beobachtet, der mit den vorangegangenen Nanoindentations- und Mikropillardruckversuchen übereinstimmt. Die von Wasserstoff beeinflussten Verschleißspuren weisen in der Nähe der Korngrenze eine höhere Schleifspurendichte auf als im Referenzzustand. Die Analyse der Transmissions-Kikuchi-Diffraktion (TKD) ergab einen ausgedehnteren Verformungsbereich, der auf einen kleineren Plastizitätsbereich beschränkt ist. Die Verringerung des Verschiebungsabstands der Korngrenze während der Wasserstoffbeladung im Vergleich zum Referenzzustand ist vermutlich auf die Sperrwirkung des Wasserstoffs zurückzuführen, die die Mobilität der Σ3-Korngrenze verzögert.

Content

1. Introduction

1.1 Motivation

As overexploitation of fossil fuels has emitted abundant greenhouse gases into the atmosphere, drastically impairing the environment and threatening the future of human beings, efforts have been put into implementing clean energy sources in our society. According to the "European green deal", 55 % of emissions of greenhouse gases are aimed to be reduced by 2030. As a type of clean energy, the only byproduct of hydrogen consumption is water, which is a plentiful resource on the earth.

However, a severe issue, so-called "hydrogen embrittlement (HE)", demonstrates a sudden brittle failure of materials, inevitably occurring during hydrogen production, transportation and applications [1]. With only few ppm amounts, hydrogen can already cause catastrophic issues as it prefers to diffuse into the stress-concentration locations of metallic materials. In unraveling the mechanism of HE, three essential factors need to be considered: material characteristics, mechanical properties and the presence and diffusion of hydrogen atoms or ions [2].

The HE mechanism was first discussed by Johnson in 1875 [3]. Afterward, numerous mechanisms have been brought up to elucidate the hydrogen-induced detrimental phenomena. Some of the widely accepted ones are listed as follows: Hydride-induced embrittlement (HIE) [4, 5]; Hydrogen-enhanced decohesion (HEDE) [6-8]; Hydrogen-enhanced local plasticity (HELP) [9]; Adsorption-induced dislocation emission (AIDE) [10-14]; Defect acting agent ("defactant") concept [15-17]; Hydrogen-enhanced strain-induced vacancies (HESIV) [18]. However, although it has been comprehensively explored, none of the above models can exclusively unveil the underlying principles of HE as enormous controversial findings are disclosed. The combination and overlapping of theories are favored and more reasonable in clarifying the HE failures. For instance, the accelerated activity of dislocations found in HELP and AIDE mechanisms might lead to the generation of micro-/nano-voids as described in HESIV mechanism [14, 18]. When enormous densities of dislocations are formed owing to the HELP mechanism piling up in the vicinity of the interfaces, take grain boundary as an example, the presence of HEDE-induced crack formation is inevitable [19]. This dislocation-grain boundary interaction is a potential cause for hydrogen-induced intergranular fracture, as the impingement of a dislocation pile-up in the vicinity of the grain boundary might be facilitated

as proposed by Novak et al. [20].

Cathodic and gaseous charging are the typical methods of introducing hydrogen into the system. The entry of gaseous hydrogen into metals usually consists of three steps: physisorption, chemisorption and final absorption. High-temperature heating and a certain pressure are necessary for gaseous hydrogen charging, so it has more strict requirements to facilities [21]. In the present study, we use a relatively small apparatus to charge the materials cathodically, which is based on the redox electrochemical reaction [22]. Once charged into the materials, hydrogen can be trapped and move through various types of microstructure features, such as vacancies that can be stabilized by hydrogen, dislocations, grain boundaries, interfaces between inclusions (carbides or oxides) to the matrix, precipitates, void, micro-and nano cracks et cetera. [23]. Those microstructure imperfections in materials are identified as different hydrogen trapping sites, which can be classified into reversible/flat and irreversible/deep hydrogen trapping sites depending on whether extra thermal energy is needed [24-28]. Unlike the deeply trapped hydrogen that has a limited impact on cracks as it tends to stay still inside the traps, the mobile hydrogen (diffusive or reversibly trapped hydrogen) has a higher risk for materials, as it tends to diffuse into the strain/stress concentrated regions around room temperature, where the HE is found more frequently. Therefore, more attention has been paid into investigating the mobile hydrogen instead of deeply trapped hydrogen in the current study.

The ferritic stainless steels studied in the present work have a wide range of applications in industry and daily life. Among them, FeCr alloys occupy an indispensable position in fusion reactors and automotive exhaust systems with high radiation and corrosion resistance [29]. However, in those harsh circumstances, exposure to hydrogen is unavoidable. Based on the classical diffusion model, hydrogen has relatively high diffusivity in ferritic iron alloys of $10^{-5} \sim 10^{-4}$ cm^2/s at ambient temperature [26, 30]. Furthermore, the small atomic radius of hydrogen (31 ± 5 pm) makes it readily absorbed and easy to penetrate through the materials [18]. Consequently, even with a low hydrogen solubility of less than 3 at. ppm for pure iron at room temperature, α-Fe is susceptible to HE [14, 31-33].

Therefore, this study mainly investigates the single-phase ferritic FeCr model alloys produced in-house with Cr content varying from 8-20 wt.%, reducing the complexity to a single-phase material, ideal for comparison with simulation works. As mentioned above, ferritic alloys have high hydrogen diffusivity and low hydrogen solubility, which are unsuitable for testing with the conventional external hydrogen charging methods as abundant hydrogen is released from

2

the metals during the sample transfer. Instead, we applied a novel and reliable *in situ* backside hydrogen charging approach, ideal for studying such material as hydrogen charging and the mechanical tests can be conducted in a nanoindentation machine simultaneously. Besides, hydrogen is electrochemically charged into the specimens from the backside, enabling thorough and high-resolution post-mortem characterizations of the microstructure in the unaffected top surface. Moreover, as a more comprehensive understanding of hydrogen interactions with microstructural features is critical to preventing hydrogen-induced damage and promoting a hydrogen-based environment-friendly economy, we studied the effect of dislocation density by micropillar compression experiments and the influence of Σ3 grain boundary by nanoscratch tests with the *in situ* apparatus.

1.2 Objective

This study aims to gain a deeper insight into the HE mechanisms that occur in the body-centered cubic (BCC) FeCr alloys by using the *in situ* backside hydrogen charging nanoindentation approach. We are attempting to answer the following questions:

1) What mechanical and microstructural effects does the mobile hydrogen cause in ferritic FeCr alloys? What is the role of the substitutional elements in these alloys regarding the hydrogen effect?

2) How does hydrogen diffuse through the FeCr alloys during *in situ* hydrogen charging from the back to the frontside of the specimen?

3) How do microstructural features like a substitutional element, dislocations or a grain boundary influence the response of FeCr alloys to hydrogen?

1.3 Strategy

We investigate the hydrogen effects on mechanical and microstructural response in the ferritic FeCr alloys, aiming to understand the HE mechanism comprehensively. The hydrogen content is quantified by thermal desorption spectroscopy (TDS) in a Hiden TPD Workstation. With a 100 nm Pd layer deposited on the sample surface using a by Leybold Univex 450 physical vapor deposition machine, hydrogen diffusivity is obtained by the Kelvin probe (KP)-based potentiometric hydrogen electrode method and the hydrogen distribution mapping is achieved by the scanning Kelvin probe force microscopy (SKPFM). The mechanical tests of

nanoindentation, nanoscratch and micropillar compression are conducted using the *in situ* backside electrochemical hydrogen charging setup assembled inside a G200 nanoindentation machine, enabling the acquirement of the mechanical data during hydrogen charging. Micropillars are fabricated on an FEI Helios plasma-focused ion beam (PFIB) machine with a Xe source. The crystal orientations of grains and grain boundaries are determined by electron backscatter diffraction (EBSD) and transmission Kikuchi diffraction (TKD) techniques. The dislocation density in bulk materials is detected utilizing the electron channelling contrast image (ECCI) technique in a field-emission crossbeam MERLIN scanning electron microscopy (SEM). Dislocation density underneath the nanoindentation imprints is investigated by applying the bright-field scanning transmission electron microscope (STEM) technique in a Jeol JEM 2200FS machine. The analyzed transmission electron microscope (TEM) foil is manufactured by a Scios dual-beam FIB with a Ga-ion source. The lateral profile of the wear tracks was measured by the confocal microscopy. The sample surface roughness is acquired from atomic force microscopy (AFM). The chemical composition of the specimen before and after the hydrogen charging is investigated by X-ray photoelectron spectroscopy (XPS).

1.4 Structure of the thesis

Following this introduction (Chapter 1), the fundamental theoretical background closely related to the current research is summarized in Chapter 2. Chapter 2 consists of the investigated materials, hydrogen interaction with metallic materials, techniques effectively applied to evaluate the hydrogen behavior and the *in situ* methods in obtaining micromechanical properties during hydrogen charging. Chapter 3 describes the treatments for the materials and experimental procedures, including mechanical tests and microstructural characterizations. In Chapter 4, the influence of mobile hydrogen on Fe alloys with different Cr and Al content is investigated with the *in situ* nanoindentation technique. In Chapter 5, emphasis is put on the effect of microstructural features like dislocations, grain boundaries and different Cr contents, on the hydrogen diffusion behavior. A new concept based on nanohardness in acquiring the hydrogen diffusion coefficient is brought up, compared with the conventional KP-based method. In Chapter 6, the focus lies on the mechanical and microstructural response of materials with different dislocation density to hydrogen. Instead of *in situ* nanoindentation test, *in situ* micropillar compression test with a simpler stress state is performed. Chapter 7 investigates the interaction of hydrogen with Σ3 grain boundary by a *in situ* nanoscratch experiment. The final Chapter 8 summarizes the findings of this thesis and

provides some insights on future works.

2. Fundamental background and literature review

2.1 Ferritic FeCr alloy

Fe and Cr are the main elements for ferritic stainless steel, which is cost-effective, has low thermal expansion, magnetism and competitive technical characteristics. Therefore, it is extensively utilized in the industry as structural components for fusion reactors and daily life as automotive exhaust systems and washing-machine drums [34, 35]. The ferritic steel is exposed to severe radiation, humidity and corrosion environments under the above circumstance, respectively [34, 36, 37]. Among all 5 grades of ferritic stainless steels, the group 2 with Cr content between 14-18 wt.%, which occupies 48 % production with high radiation and corrosion resistant, is the most commonly used grade (Fig. 2.1) [34]. Moreover, it is an ideal model ferritic binary alloy for simulation in general [35]. Therefore, we investigated the model FeCr alloys to study the hydrogen-induced embrittlement to this type of steel.

Group 1	Group 2	Group 3	Group 4	Group 5
10%-14%	14%-18%	14%-18% stabilised	Added Mo	Others
30%	48%	13%	7%	2%
Types 409, 410, 420 Cr content: 10%-14%	Type 430 Cr content: 14%-18%	Types 430Ti, 439, 441, etc. Cr content: 14%-18%. Include stabilising elements such as Ti, Nb, etc.	Types 434, 436, 444, etc. Mo content above 0.5%	Cr content of 18%-30% or not belonging to the other groups

Fig. 2.1 The five standard groups of ferritic stainless steel grades in the industry (ASTM A 240 - 06C, Nov. 2006). Adopted from [34].

The standard Fe-Cr phase diagram calculated thermodynamically is shown in Fig. 2.2, edited by Massalski [36]. With Cr content less than 20 wt.%, a homogeneous ferritic phase can be attained without the influence of the σ-phase. Sigma phase is an intermetallic compound that usually exist in transition-metal alloy system without precise stoichiometric composition [38]. It is hard and brittle, hence harmful during the production and service of the material, a few percent of which would cause a drastic degradation of the material. Among all the sigma

phases, only σ-FeCr and σ-FeV display evident magnetic properties [39]. As exhibited in Fig. 2.2, σ-phase is a close-packed tetragonal (P4$_2$/mnm) with 30 atoms per unit cell. It forms at ~830 °C, and decomposes at ~460 °C to Fe-rich (α) and Cr-rich (α') phases as reported by Kubaschewski [40]. The single-phase σ only forms in binary alloy with Cr content above 40 %, depending on the purity, mechanical state and annealing temperature [41]. Both σ-phase and decomposition of Fe-rich (α) and Cr-rich (α') phases for FeCr alloy (Cr ≥ 15 wt.%) can be avoided by reheating above ~800 °C and cooling rapidly [34].
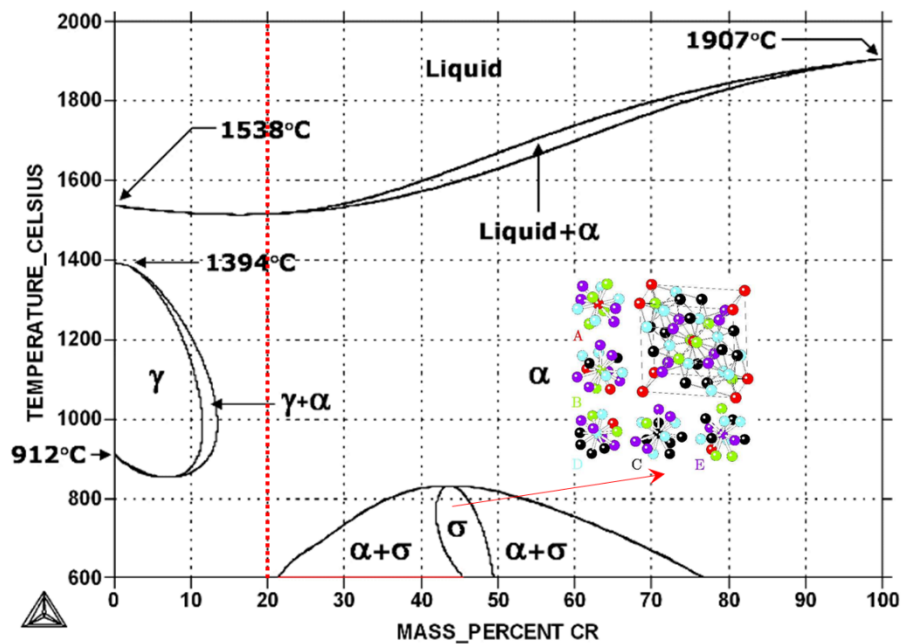
Fig. 2.2 Standard thermodynamic Fe-Cr binary phase diagram adapts from Massalski with the unit cell of σ-phase with sub-lattice A-E with their nearest neighbor shell atoms. Redrawn from [39, 42].

2.2 Hydrogen in metals

2.2.1 Basic properties of hydrogen

Hydrogen element ranks first place of the periodic table of elements. The hydrogen atom ^{1}H is composed of one electron outside the nucleus and the nucleus containing one proton. There are seven hydrogen isotopes discovered so far ([1]H ~ [7]H), among which deuterium with one more neutron and tritium with two more neutrons compared to ^{1}H are the most employed isotopes tracer elements for scientific research, especially in the atom probe tomography (APT) analysis [43, 44]. Hydrogen has an atomic weight of 1.0079, with a boiling point of -252.87 °C and a

melting temperature of -259.14°C. The basic properties of hydrogen are listed in Table 2.1. It has a higher energy density of 120 MJ/kg than diesel (45.5 MJ/kg) and gasoline (45.8 MJ/kg) [45]. However, as the ignition energy for hydrogen mixture with air (0.017 mJ) and hydrogen mixed with oxygen (0.0012 mJ) is low and the ignition range for a volumetric fraction of hydrogen to air is 4-75 %, caution must be taken when getting access to hydrogen [45].

Table 2.1 Basic properties of hydrogen (taken from [18])

Atomic weight	1.00794 g/mol	First ionization energy	1312 kJ/mol
Oxidation state	+1, -1	Covalent radius	(31 ± 5) pm
Electronic configuration	$1s^1$	van der Waals radius	120 pm
Electronegativity (Pauling)	2.20	Electron affinity	73 kJ/mol

High-pressure hydrogen gas (20-70 MPa), low-temperature hydrogen liquid and solid-state hydrogen are standard formats for hydrogen storage. Among all the methods, solid-state hydrogen storage possesses the advantages of high energy density within a small volume and enhanced security during transportation, hence reducing transit expenses. Hydrogen can be absorbed physically by metal-organic frameworks and carbonaceous material such as carbon nanotubes, graphite nanofiber and carbon nanofiber as they have a large specific surface area, the absorbed amount of which reckons on both temperature and pressure. In addition, hydrogen can be chemically preserved as metal hydrides (alkaline earth metal, rare-earth element, Ti, Zr, Mg and V, Nb, Ta based alloys), complex coordinate hydrides with alkali metal ($NaAlH_4$, $LiAlH_4$, $NaBH_4$, $LiBH_4$ etc.) and liquid organic hydrides (NH_3BH_3) [46].

2.2.2 Hydrogen embrittlement mechanisms

The overexploitation of fossil fuels has already caused many severe consequences nowadays, accelerating the environmental degradation, deforestation and distinction of animals, putting overwhelming threats to human society. Water is one of the basic requirements for life, and it can be decomposed into hydrogen and oxygen. For decades, we have endeavored to use hydrogen as energy as its consumption will only generate water and heat. The residual clean energy sources, such as solar, wind and tidal energy, have been exploited to produce hydrogen by electrolysis of water. Therefore, implementing the hydrogen-based economy would be environmentally friendly and reduce the emission of greenhouse gases as settled in the "European green deal", which aims to reduce the 55 % emissions of greenhouse gases by 2030.

Hydrogen has various applications in industry, agriculture, transportation, power plants and aeronautical technologies. However, hydrogen-related procedures, such as production, conservation, transportation, and consumption, still face a severe problem: the so-called hydrogen embrittlement (HE). This concept was first discussed by Johnson in 1875 [3].
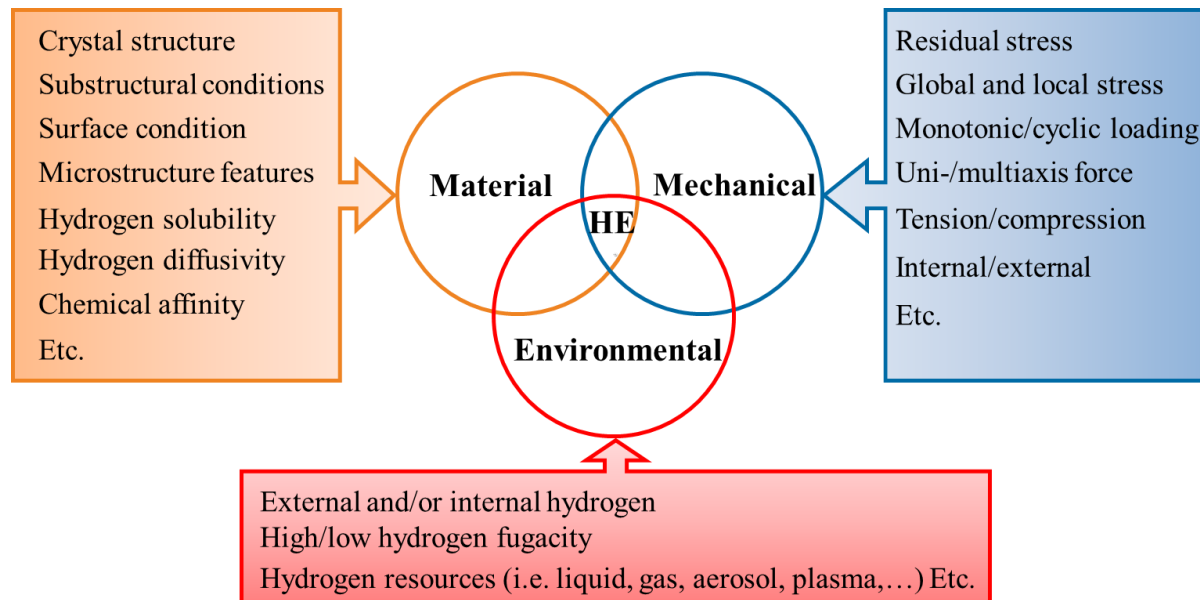

Fig. 2.3 Three essential factors in describing HE. Redrawn and revised from [2].

Hydrogen can be introduced in different metallurgical processes during steel production, such as melting, casting, pickling, galvanization and welding. When inevitably absorbed into metallic materials, hydrogen prefers to diffuse into the stress-concentration locations under tensile stress, causing a sudden brittle failure of the material, especially for high-strength steel such as manganese and nickel steel with few ppm amounts [1]. When it occurs to the critical linkage part of a construction, it will lead to catastrophic failure of the construction. Three essential factors that need to be considered in unraveling the mechanism of HE are material characteristics, mechanical properties and the presence and diffusion of hydrogen atoms or ions, as displayed in Fig. 2.3 [2].

Commonly observed degradation phenomena related to hydrogen embrittlement are: a) hydrogen-induced cracking (HIC) that originates from the H_2S without stress; b) sulfide stress cracking (SSC) that leads to the corrosion of material in the oil and gas industry, where a considerable amount of hydrogen sulfide exists under stress; c) high-temperature hydrogen attack that material like turbine upon exposure to the high temperature, the carbon steel combines hydrogen and generates methane (CH_4) accumulation in micropores, initiating

cracks; d) hydrogen blistering that forms subsurface cavities by accumulated hydrogen gas; e) white-etching-cracks (WECs) that might be accelerated by the hydrogen generated from the lubricant, which in return further promote the absorption of hydrogen; f) hydrogen introduced hardening/ softening.

Numerous mechanisms have been raised to explain those mentioned above hydrogen-introduced detrimental phenomena and some of the widely accepted mechanisms are in-depth described in the following chapters, which mainly include: Hydride-induced embrittlement (HIE); Hydrogen-enhanced decohesion (HEDE); Hydrogen-enhanced local plasticity (HELP); Adsorption-induced dislocation emission (AIDE); Defect acting agent ("defactant") concept; Hydrogen-enhanced strain-induced vacancies (HESIV); etc.

2.2.2.1 HIE

Fig. 2.4a shows the hydride-induced embrittlement (HIE) mechanism, which is generally utilized in materials containing typical hydride-forming elements such as V, Nb, Ti, Hf, Ta and Zr, which is the element of the group Vb. The generation and coalescence of the brittle hydride phase to a critical dimension tend to facilitate the initiation of the cleavage, especially under stress with the absorbed hydrogen due to hydrostatic stress in the vicinity of the cracks [4, 5]. This type of crack frequently presents within hydrides and occurs within a specific strain rate region, providing sufficient time for hydrogen diffusion and an appropriate temperature range that maintains the stable hydride. An example is the titanium hydride in Ti-4 wt.%Al that is detected by the transmission electron microscopy (TEM) [47, 48]. In addition, multiscale simulations demonstrate the potential of the local nano-hydrides formation in Ni with the combined effect of pre-existing dislocation (tensile stress field) and the highly populated hydrogen, which leads to the reduction in the line energy of dislocation [5].

2.2.2.2 HEDE

The hydrogen-enhanced decohesion (HEDE) mechanism as shown in Fig. 2.4b was first introduced by Pfeil in 1926 [6] and later developed by Oriani [7] and Troiano [8]: The HEDE mechanism explains the crack initiation in the interface region (such as grain boundary or phase boundary) as the hydrogen weakens the interatomic metal-metal bonding by insertion of the 1s electron from hydrogen to the available electronic hole in the 3d shell of iron, thus reducing the strength of atomic planes [8]. Therefore, a high enough hydrogen amount attracted by the hydrostatic stress field ahead of the crack tip area is the prerequisite to verify the concept.

Direct experimental evidence is unavailable so far as quantifying accumulated hydrogen concentration in the crack tip, which deviates orders of magnitude from the maximum bulk hydrogen content and evaluating the extent of reduction in the cohesive energy is complex [5]. Instead, numerical analysis, especially ab-initio calculation, can support the mechanism as a reduction in the cohesive energy is deduced with enhanced hydrogen concentration captured by a high elastic stress field ahead of the crack tip region [19, 49]. Moreover, a synergic activity of hydrogen and other deleterious elements such as P, S, Si and Mn has been suggested as the hydrogen-induced crack upon this mechanism occurs typically at the interfaces, the preferable positions for those elements [50].
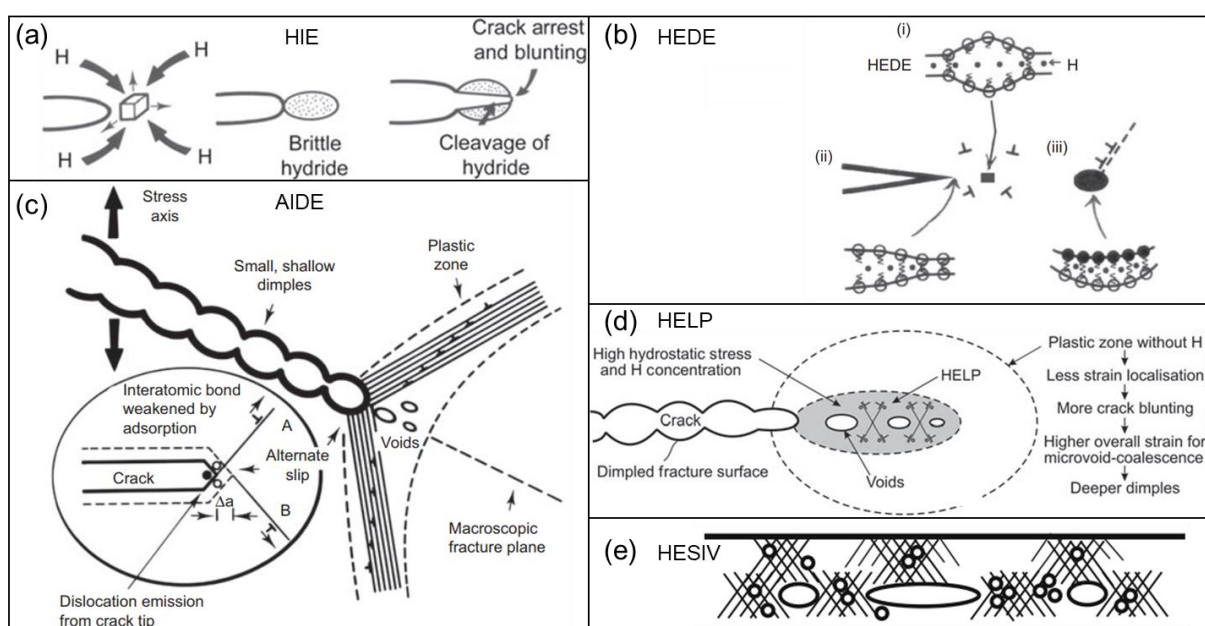

Fig. 2.4 Schematic diagram of four models commonly applied for explaining HE phenomena: (a) HIE; (b) HEDE; (c) AIDE; (d) HELP; (e) HESIV. Adopted and revised from [14] and [18].

2.2.2.3 HELP

First illustrated by Beachem when comparing the fractured surface and flow stresses of steels, the hydrogen-enhanced local plasticity (HELP) mechanism (Fig. 2.4d) suggests that the ingress of hydrogen facilitates the localized dislocation activity near the crack tip, leading to the stress localization and confined plastic fracture [9]. The outburst crack could exhibit intergranular or transgranular, correlating with the hydrogen concentrated location. In the presence of hydrogen, the mobility of dislocations is enhanced in materials subjected to stress in the format of increased dislocation density or/and moving velocity of dislocation. The alteration in the localized stress and strain fields resulting from the modified microstructure is treated as the

extended scope of the damage, which leads to the decay of the mechanical properties of materials. The accelerated activities of dislocation are mainly supported by the following evidence.

I) Based on the elasticity theory, the hydrogen atmosphere generates the shielding effect surrounding the dislocations. This causes a reduction in the repulsive force among the dislocations and obstacles, resulting in a confined plastic region filled with dislocation pile-ups with smaller spacing and prone to damage [51, 52].

II) Atomistic studies like density function theory (DFT) calculation in iron manifest the reduction in Peierls stress originating from the decreased dislocation core energy [29]. In addition, the first principle numerical work reveals a decreased kink nucleation energy leading to the enhanced mobility of screw dislocations within a particular temperature range with the introduction of hydrogen [53].

III) With the introduction of electron beam dissociated hydrogen, observation of enhanced moving velocity of dislocations (more than ten times) was achieved by *in situ* TEM studies [52].

IV) From the macroscopic perspective of embrittlement, the enhanced dislocation activity causes a ductile mode failure in a limited region, with dimples appearing in the fractured surface in hydrogen-affected samples [9].

V) Mechanical softening, manifested as the reduction in the flow stress, was observed in tensile tests upon the introduction of hydrogen [54, 55]. Other signals observed macroscopically, such as a higher density of slip traces, coarser slip bands due to inhibited cross-slip and activation of some extra slip systems, are also suggested to indirectly prove the higher dislocation activity attributed to the HELP mechanism.

However, controversies arise as localized plastic deformation, detected in materials that HE fractures, can also be accredited to the hindrance of hydrogen to the dislocation motion, which will be explicitly described in the section on the hydrogen-dislocation interaction.

2.2.2.4 AIDE

As a mechanism that attempts to clarify HE phenomena explained by HEDE and HELP concepts separately, adsorption-induced dislocation emission (AIDE) was first put forward by

Lynch in 1976 [10-14]. AIDE mechanism includes two steps: Firstly, the absorbed hydrogen at the crack tip weakens the interatomic bonds of crystalline over several atomic distances; The subsequent step involves the hydrogen-facilitated nucleation of dislocations to the different slip planes readily for cracks, promoting the movement of the dislocations away from the crack tip and further propagation of the crack, as illustrated in Fig. 2.4c. The dislocation nucleation encompasses both the dislocation core formation and the shearing of atoms. In contrast to the HELP mechanism, emphasis has been put on the enhanced emission of dislocations instead of increased dislocation mobility in AIDE. Besides, the interaction between hydrogen and surface (i.e. sample, cracks or voids surface) is essential in this failure mechanism. The supporting evidence is that the crack propagation velocity is far higher than the hydrogen diffusion rate (ratio of hydrogen diffusivity and crack propagation velocity $< 10^{-8}$). However, the hydrogen-leading crack still presents, which indicates the existence of the beforehand hydrogen adsorption procedure [1]. This failure has similar fractured features to liquid-metal embrittlement (LME) ascribed to the solute accumulation at the crack tip as indirect support for the AIDE concept [14].

Moreover, not only the excessive emitted dislocations ahead of crack tips assist the further development of the cracks under external stresses. The facilitated micro-/nano-voids nucleation and coalescence also contribute to either the crack in the matrix of materials or the ductile failure with large deep dimples decorated with small, elongated dimples. The observed crack tip angle is supposed to be small as the micro-voids inhibit the crack opening (Fig. 2.4c). Depending on dislocation/void nucleation location, both intergranular and transgranular failures can be noticed [10, 13].

2.2.2.5 HESIV

Fig. 2.4e displays the hydrogen-enhanced strain-induced vacancies (HESIV) developed by Nagumo et al. [18], supposing that hydrogen facilitates the generation of vacancies initiated from the strain-concentrated region. Vacancy clusters result from the agglomeration of vacancies retarded and stabilized by hydrogen, leading to the formation of voids that causes the present of microcracks or a reduction in stress-absorbing capacity. Instead of hydrogen itself, the vacancies play a more essential role in the deterioration of materials, which follows the general crack burst process of void nucleation, growth and coalescence. This mechanism was brought up based on a thermal desorption analysis (TDA) test in the pre-strained low-carbon ferritic steel. As a tracer element, tritium detected by TDA is drastically decreased with

annealing treatment at a low temperature of 200 °C, alluding that the vacancies play a more critical role in trapping tritium instead of dislocation in this case [56]. Afterward, an enhanced amount of hydrogen was measured by TDA in pre-charged Inconel 625 alloy and iron with increased strain up to 0.025, supporting the HESIV mechanism that hydrogen facilitates the generation of strain-induced vacancies [57]. The vacancy nature of introduced defects is further verified through positron annihilation spectroscopy (PAS) by Sakaki et al. [58], indicated by the enhancement of mean positron lifetime in charged pre-strained pure α-Fe.

Moreover, the retardance of hydrogen to dislocation motion has been experimentally noticed by environmental TEM and attributed to the hydrogen- vacancy complex as numerally verified by atomistic simulation in aluminium, showing a drastically increased critical shear stress compared with the case without exposure to hydrogen [59].

2.2.2.6 "Defactant" concept

Based on the thermodynamic calculation, the "defactant" concept was first brought up by Kirchheim [15-17]. The concept originates from the fact that the introduction of solute molecules called "surfactants" (i.e. surface acting agents) reduces the surface energy of water. Analogous to this phenomenon, Kirchheim [15-17] suggested that the introduction of hydrogen ("defactant") to crystalline defects, such as dislocation and vacancies, can also decrease the formation energy of these imperfections. Developed from the Gibbs equation, the theory can be quantitatively expressed as follows [17]:

$$\Gamma_H \equiv \frac{1}{V} \frac{\partial n_H}{\partial \rho} \bigg|_{V,T,\mu_H,n_B} \tag{2.1}$$

where μ_H is the chemical potential of excess Γ_H with the number of n_H at the defects (e.g. amount of vacancies, dislocation length, grain boundary area) upon a constant temperature T in a material B with a constant number of atoms n_B. ρ is the density of the defect and V the volume. This concept provides theoretical support for the above-mentioned HELP and AIDE mechanisms as the introduction of hydrogen reduces the dislocation formation energy, thus enhancing the dislocation activities [17]. The reduction in the homogeneous dislocation nucleation energy has been verified by *in situ* nanoindentation experiments, showing the reduction in the pop-in loads, which correlates with the critical shear stress of materials [60, 61]. The increase in the dislocation motion can also be explained as the hydrogen reduces the formation energy for kink pairs in BCC materials [62]. In addition, the "defactant" concept can

14

also shed light on HESIV, which involves both facilitated emission of dislocations and generation of vacancies.

However, although it has been comprehensively explored, none of the above-mentioned models can exclusively unveil the underlying principles of HE as enormous controversial findings are disclosed. The combination and overlapping of theories are favored and more reasonable in clarifying the HE failures. For instance, the accelerated activity of dislocations found in HELP and AIDE mechanism might lead to the generation of micro-/nano-voids as described in HESIV mechanism [14, 18]. When enormous dislocations formed owing to the HELP mechanism piling up in vicinity to the interfaces area, take grain boundary as an example, the presence of HEDE induced crack is inevitable [19]. This dislocation-grain boundary interaction is a potential cause for hydrogen-induced intergranular fracture as the impingement of dislocation pile-up in the vicinity of the grain boundary might be facilitated as proposed by Novak et al. [20].

### 2.2.3 Entry of hydrogen into the metals

2.2.3.1 Gaseous hydrogen

It usually requires three steps for gaseous hydrogen to enter the material: physisorption, chemisorption and final absorption [21]. As a common hydrogen charging method for experimental investigations, it can also occur during the manufacturing procedure, like molten metal exposed to a hydrogen-containing atmosphere. The hydrogen experiences a transition from the "adsorbed" in the initial two steps to the final "absorbed" state in the third step. The van der Waals forces play an essential role in this long-range physisorption process that is reversible. Upon the contact of the molecular hydrogen with the surface of the targeted material, a multilayer fluid comes into existence instantly, along with an enthalpy alteration due to the condensation of the gaseous adsorbent (≤ 20 kJ/mol) [21].

Afterward, short-range chemisorption takes place between the material and molecular hydrogen. It is either a slowly reversible or an irreversible process as the energy barrier for breaking down metal-metal, hydrogen-hydrogen and the generation of a polarized covalent hydrogen-metal bond is required (20-150 kJ/mol) [63].

In the end, the final absorption occurs, incorporating the product (hydrogen atom/ion) of the previous chemisorption into the lattice of the metal. The amount of absorbed hydrogen depends on the intrinsic properties like the microstructure or chemical state of the metal [64]. The whole

procedure can be interpreted by the following chemical formula and the hydrogen amount in an equilibrium state can be quantitatively evaluated by Sieverts' law [65]:
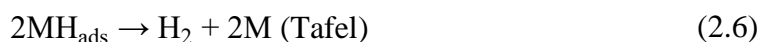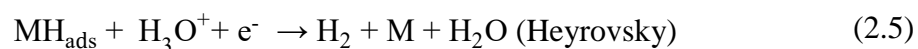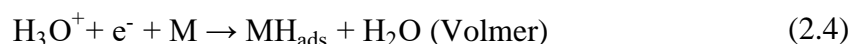
$$\frac{1}{2}H_{2(g)} + M = MH_{abs} \tag{2.2}$$
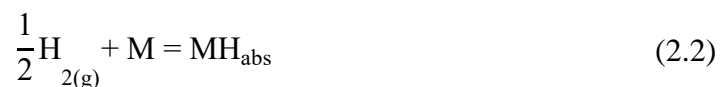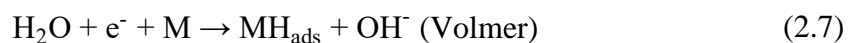
$$C = KP_{H^2}^{1/2} \tag{2.3}$$

where M represents the metal; H_{abs} is the hydrogen absorbed on the metal surface; C is the equivalent solubility of hydrogen in a metal; K is a constant; P_H^2 is the partial pressure of hydrogen gas. Although gaseous hydrogen has not been applied in this study, the results of literature involving this experimental method have been utilized.

2.2.3.2 Cathodic hydrogen charging

Besides hydrogen gas exposure, cathodic hydrogen charging based on the redox electrochemical reaction has commonly been found during the metallurgy process, such as the pickling, galvanization and cathodic protection [22]. Proportional relation between the applied current density and hydrogen activity was noticed in pure α-Fe [66, 67]. The cathodic hydrogen evolution reaction (HER) occurs on the metal surface through multiple processes, which basically involves the generation of MH_{ads} (adsorbed hydrogen atom) and the hydrogen recombination reaction leading to the formation of molecular hydrogen [68]. In the acidic solution, the first step is achieved by discharging a hydronium ion (Eq. (2.4)) and the subsequent step includes the electrochemical Heyrovsky and/or the chemical Tafel reaction.

$$H_3O^+ + e^- + M \rightarrow MH_{ads} + H_2O \text{ (Volmer)} \tag{2.4}$$

$$MH_{ads} + H_3O^+ + e^- \rightarrow H_2 + M + H_2O \text{ (Heyrovsky)} \tag{2.5}$$

$$2MH_{ads} \rightarrow H_2 + 2M \text{ (Tafel)} \tag{2.6}$$

Differing from the acidic solution, in the case of alkaline/neutral solution, the intermediates (MH_{ads}) are produced by dissociating H_2O. Besides, the hydroxide ion is generated in the Volmer and Heyrovsky steps, while the Tafel step is identical to the acidic condition.

$$H_2O + e^- + M \rightarrow MH_{ads} + OH^- \text{ (Volmer)} \tag{2.7}$$

$$H_2O + e^- + MH_{ads} \rightarrow H_2 + M + OH^- \text{ (Heyrovsky)} \tag{2.8}$$

16

$$2MH_{ads} \rightarrow H_2 + 2M \text{ (Tafel)} \tag{2.9}$$

Some of the adsorbed hydrogen on the metal surface will eventually be absorbed by the material via the diffusion of MH_{ads} into the lattice as shown in the following reaction:

$$MH_{ads} \rightarrow MH_{abs} \tag{2.10}$$

Besides the hydrogen charging methods previously interpreted, hydrogen can also be introduced through plasma charging or the hydrogen gas dissociated by the high-voltage electron beam, enabling the direct investigation of microstructure evolution under high-resolution microscopy (e.g. scanning electron microscopy (SEM) or TEM) [59, 69]. However, unlike the cathodic charging method, hydrogen activity cannot be controlled easily. Some specific types of active metals can be indirectly charged with hydrogen by water vapor in a moisture atmosphere, such as aluminium-containing metallic alloys [70]. The chemical reaction can be written as:

$$3H_2O + 2Al \rightarrow Al_2O_3 + 6H^+ + 6e^- \tag{2.11}$$
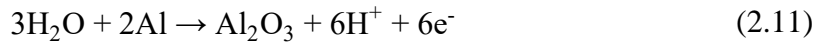
In addition, the hydrogen adsorption process can be affected by many factors, such as the intrinsic physical/chemical properties and surface and/or subsurface microstructure of metals, externally applied strain, temperature et cetera [71].

2.2.3.3 Diffusion of hydrogen

The accumulated absorbed hydrogen atoms on the metal surface tend to diffuse into the matrix of the bulk metal. The driving force is the gradient of the chemical potential across the specimens. The mathematical description of this molecular transfer process was first interpreted by Fick in 1855 [72], adopting the concept of heat conduction. The amount of substance passing through the unit area within unit time J [cm^2/s] in an isotropic matrix has a positive relation with the concentration gradient in the direction normal to the diffusion path, which can be depicted by the classical Fick's 1st law.

$$J = -D\frac{dc}{dx} \tag{2.12}$$

where D represents the diffusion coefficient [cm^2/s], and c is the concentration. x is the position [cm]. The difference between input and output flux equals the changes in concentration within

the volume element as shown in the following continuity equation:

$$\frac{\partial c}{\partial t} + \frac{\partial J}{\partial x} = 0 \tag{2.13}$$

Combining Eq. (2.12) and Eq. (2.13), Fick's 2nd law can be derived:

$$\frac{\partial c}{\partial t} = D \frac{\partial^2 c}{\partial x^2} \tag{2.14}$$

This fundamental partial differential equation can be solved and applied to numerous diffusion occasions by adopting variant initial and boundary conditions.

2.2.4 Different trapping sites for hydrogen

Hydrogen can be trapped at and move through various types of microstructure features, such as vacancies that can be stabilized by hydrogen, dislocations, grain boundaries, phase boundaries, interfaces between inclusions (carbides or oxides) to the matrix, precipitates, void, micro-and nano cracks et cetera as shown in Fig. 2.5 [23]. Those microstructure imperfections in materials are therefore identified as different hydrogen trapping sites.
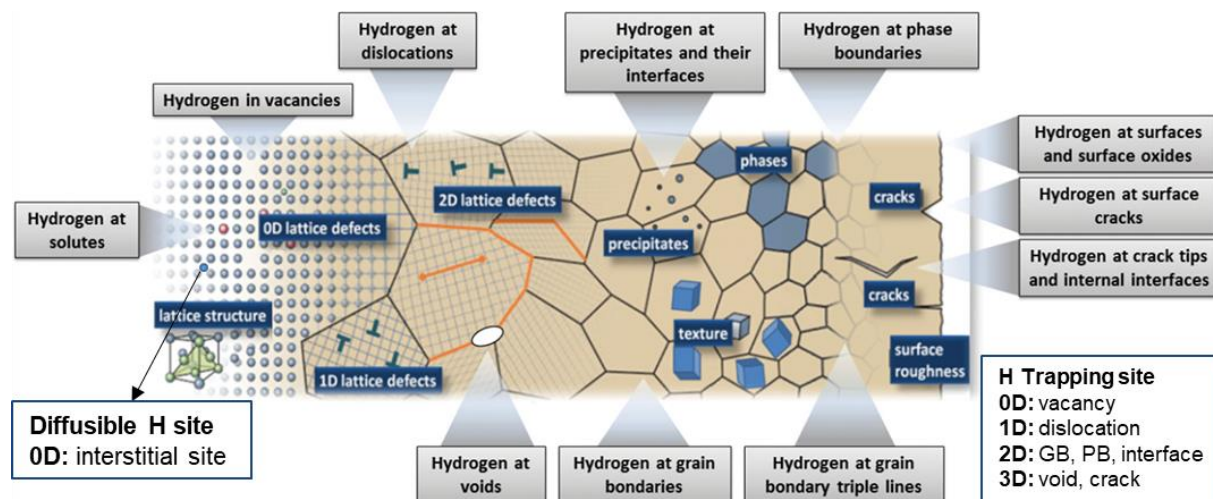

Fig. 2.5 The interaction of hydrogen with various microstructural features in the materials. Adopted and revised from [23].

As schematically illustrated in Fig. 2.6, different activation energies (E_a) are required for hydrogen to migrate either via the interstitial sites referred to as the diffusive hydrogen or various hydrogen traps. Although the specific threshold energy is unable to be defined as the intrinsic microstructure and external environmental conditions (e.g. temperature) vary between

18

systems, a rough value of ~50 kJ/mol can be generally utilized to distinguish the reversible/flat and irreversible/deep hydrogen trapping sites [24-28]. Extra thermal energy is necessary for releasing hydrogen from the deep traps at ambient temperature while releasing hydrogen from the reversible trapping sites is a matter of duration [73]. The existence of hydrogen trapping sites sluggish the hydrogen motion, attracting a higher amount of hydrogen inside the materials. The deeply trapped hydrogen shows a limited impact on cracks from a practical perspective as it stays still inside the traps, which is supported by the experiment conducted in 13Cr stainless steel [74]. For the diffusion of hydrogen in pure Fe jumps between the interstitial lattices, the activation energy of 4-8 kJ/mol is needed [24]. The mobile hydrogen (diffusive or reversibly trapped hydrogen) has a higher risk for materials, as it tends to diffuse into the strain/stress concentrated regions around room temperature, where the HE is found more frequently. Therefore, more effort has been put into investigating mobile hydrogen (slightly trapped hydrogen) instead of deeply trapped hydrogen in this PhD thesis.
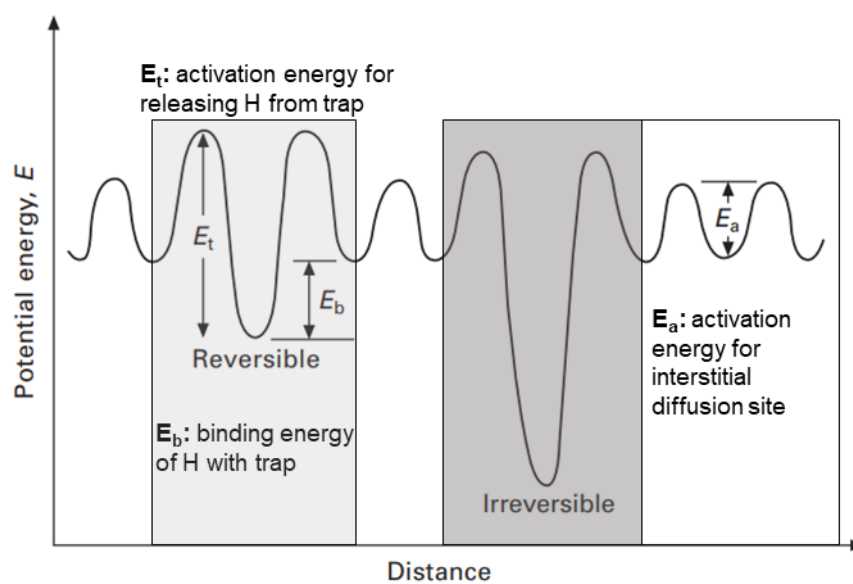

Fig. 2.6 Schematic interpretation of the activation energy for interstitial hydrogen diffusion site (E_a) and hydrogen trapping site (E_t), as well as the binding energy for hydrogen traps (E_b). Adopted and revised from [73].

Hydrogen adsorption is an endothermic reaction, and higher temperature hence leads to the higher solubility of hydrogen in iron, as shown in Fig. 2.7 [18, 42]. The diffusivity and solubility behavior of hydrogen within BCC and FCC materials differ greatly, attributed to different lattice structures. Body-centered cubic (BCC) lattice owes a larger tetrahedral interstitial site (0.36×10^{-10} m) than the octahedral interstitial site (0.19×10^{-10} m), taken a lattice

constant of 2.86×10^{-10} m measured at ambient temperature [31]. On the contrary, the Face-centered cubic (FCC) structure has a larger octahedral interstitial site (0.53×10^{-10} m) compared to the tetrahedral interstitial site (0.28×10^{-10} m), assuming the lattice constant of 3.64×10^{-10} m measured at 911 °C [31]. Therefore, hydrogen prefers to stay at the tetrahedral site for BCC metals, as confirmed by the nuclear reaction channeling technique at room temperature [75]. However, at elevated temperatures, the occupation ratio of hydrogen is enhanced in the octahedral sites in BCC metals [18].

The experimental quantification of hydrogen amount is rather complicated as the hydrogen diffusivity is high ($10^{-5} \sim 10^{-4}$ cm^2/s) in ferritic steel at room temperature [26, 30]. The theoretical relation of solid hydrogen solubility (θ) with temperature T [K] and hydrogen gas pressure P in α-iron was brought up by Hirth [76]. This relation is based on Sieverts' law and is expressed as follows:

$$\theta = 0.00185\sqrt{P} \exp\left(-3440/T\right) \tag{2.15}$$

The equilibrium hydrogen concentration in ferritic steels at ambient temperature is small (ca. 2×10^{-8} in atomic ratio) under hydrogen gas of 1 bar, as calculated from Eq. (2.15). Therefore, commonly observed hydrogen concentrations of ~0.5-3 at.ppm in α-iron as measured by experiments are mainly attributed to the various hydrogen traps [14, 31-33, 77, 78]. The following paragraphs will describe the representative hydrogen traps (vacancy, dislocation and grain boundary) that are thoroughly investigated in this PhD thesis.

2.2.4.1 Vacancy

As the simplest defect in the metal, vacancy possesses a relatively large volume and can act as a free surface to attract hydrogen [79]. The binding energy of hydrogen-vacancy is intense, even comparable to the chemisorption affinity of hydrogen [64]. Plenty of vacancies can be generated through radiation. A moderate vacancy concentration is generally produced by cold working or quenching from the elevated temperature, as experimentally verified by Zehtbauer et al. [80] through positron annihilation investigation in severely plastic deformed materials. They are treated as dominant hydrogen trapping sites verified via the positron annihilation technique [81]. Without the presence of hydrogen, the vacancies induced by low-temperature irradiation were annihilated after external heating. However, when hydrogen appeared, the annihilation procedure was delayed [64]. In addition, simulation from Lu et al. [82] demonstrated the accelerated generation of vacancies by hydrogen to an enhancement of 23 %.

They also claimed that 3-6 H-atoms can be contained in one vacancy. The content depends on the size of the octahedral sites in BCC and FCC lattices.
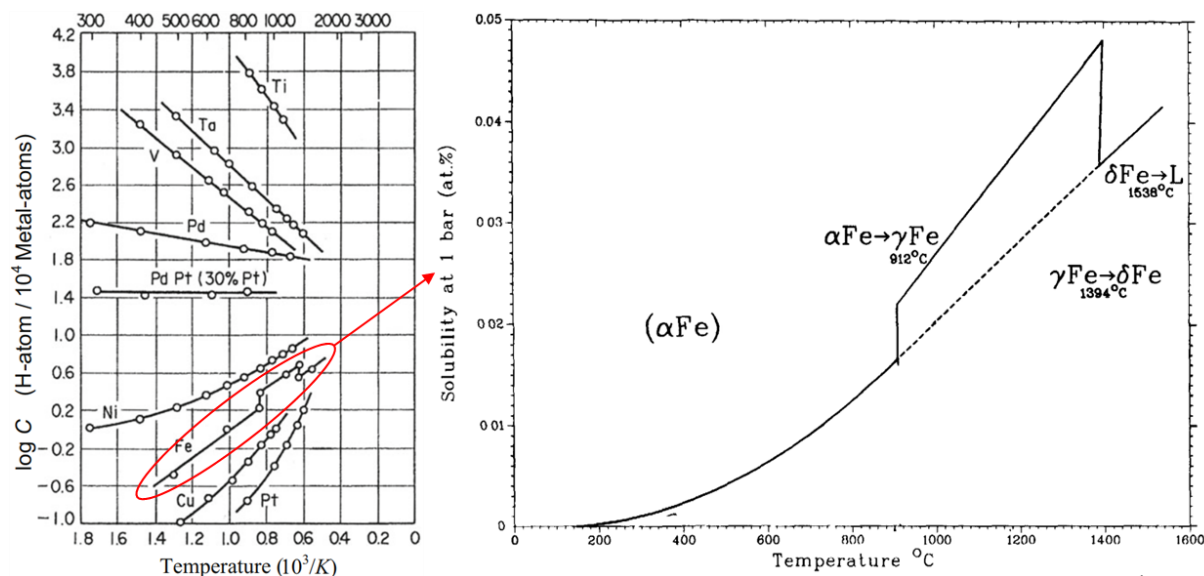

Fig. 2.7 Hydrogen solubility evolution at different temperatures in various metals at 1 bar hydrogen atmosphere. Adapted and revised from [18] and [42].

2.2.4.2 Dislocation

As has been extensively discussed in the previous section of the HELP mechanism, dislocations play a critical role in the plastic deformation of metallic alloys. Therefore, thoroughly investigating and unraveling the localized interaction between interstitial hydrogen and dislocation stress/strain field is significant for understanding HE. In the theoretical prospective, with an excessive concentration of hydrogen in the vicinity of dislocation, an extra chemical potential term must be added based on the mean-field approximation. [64, 83]. In this case, the segregation of the accumulated hydrogen cloud to the dislocation was predicted. The stronger binding energy of 0.6 eV between dislocation core and hydrogen than the hydrogen-hydrogen binding energy of 0.2 eV was calculated in Pd [84, 85]. The computed core radius of dislocation is roughly one Burgers vector and can trap about one to two hydrogen atoms per metal atom. In addition, the potential occurrence of dense packed hydrogen within the stress field region over several nanometer was predicted and called "Fermi-Dirac cloud" [85].

Experimental evidence of the reduced dislocation motion by hydrogen was supported by Xie et al. [59], utilizing the *in situ* environmental TEM during the cyclic compression test in a delicately fabricated pillar made from a single crystal Al. They claimed that the formed

hydrogenated vacancies are responsible for the reduced dislocation motion, describing it as a dislocation locking effect. An indirect observation of deuterium trapping at dislocations and grain boundaries in bcc martensitic steel was also achieved by the cryogenic APT [43]. From a macroscopic and quantitative perspective, it is noticed that dislocation and vacancies are the main trapping sites observed by SKPFM and TDS in bcc Fe-5 wt.% Ni [81]. Furthermore, Ono and Meshii [86] detected by applying a quadrupole mass spectrometer that dislocations are the leading hydrogen trapping sites in single alpha iron. Besides, the hydrogen-induced yield strength enhancement was supported by Matsui et al. [54], who performed the tensile tests in pure iron at a temperature below 190 K.

Molecular dynamics (MD) simulations also found this hydrogen-induced hardening effect by deploying numerical uniaxial loading tests in a plastically pre-deformed single crystal iron, exhibiting that hydrogen prefers to stay around dislocation (i.e. reversible trapping site of strain around dislocation plus deep trapping dislocation core), especially edge dislocations [87]. The yield strength enhancement is stated as the result of the pinning/dragging effect of hydrogen atoms to the motion of edge dislocations. Moreover, atomistic simulations conducted by Song et al. [88] in α-Fe show that hydrogen attracted by the stress-concentrated region might form the Cottrell atmosphere following the moving dislocations, retarding the dislocation mobility consistent with the solute drag theory. The author declares that the phenomena can be applied to FCC metals like Ni or Al, with easy, non-thermally activated gliding. Even the local nano-hydride formation is postulated by multiscale numerical work to be possible in Ni with surrounding superabundant hydrogen and the dislocation under tensile stress field [5].

2.2.4.3 Grain boundary

As a prerequisite for the HEDE mechanism, the hydrogen absorption of grain boundary has been explored extensively. As generally elucidated in the literature, hydrogen interstitials can be segregated and trapped by grain boundaries [86, 89-91]. Controversial arguments about the hydrogen affinity to the grain boundaries with different characters have been addressed in simulation works. They can either act as the reversible hydrogen trapping site as the $\Sigma 3$ twist grain boundary or the deep hydrogen trapping sites as found in the $\Sigma 9$, $\Sigma 11$ and $\Sigma 17$ boundaries according to the simulation of Eunan et al. [92] in α-Fe at room temperature based on the tight-binding model. In addition, according to the first-principles simulation in alpha-iron, Du et al. [89] have classified grain boundaries into two categories, the close-packed grain boundary and the open grain boundary, based on different behaviors of grain boundaries when exposed to

hydrogen. The close-packed grain boundary (e.g. the $\Sigma3[1\text{-}10](112)$ grain boundary in BCC metal) attracts more hydrogen, acting as the barrier for hydrogen diffusion and reducing the strain required for fracture with hydrogen exposure, which is attributed to the unique interstitial sites with higher coordination at the interface between grain boundary and matrix. On the contrary, the more open grain boundary (e.g. $\Sigma5[001](310)$ grain boundary in BCC metal) favors the diffusion along the grain boundary direction.

Regarding the experimental perspective, in the polycrystalline nickel, Oudriss et al. [93] recognized a hydrogen trapping behavior around the "special" $\Sigma3^n$ grain boundaries by performing secondary ion mass spectrometry in combination with the electron backscatter diffraction (EBSD) analysis of microstructure. In the direction parallel to the grain boundary, the grain boundary may act as the short diffusion pathway for hydrogen depending on the atomic distribution [89, 94, 95], and the diffusivity of hydrogen along grain boundaries is proposed to be faster than across the normal direction of the grain boundaries according to density functional theory calculations [96].

2.3 Characterization of hydrogen

2.3.1 Microstructural characterization of materials

Scanning electron microscopy (SEM) is a certain kind of microscopy commonly used to characterize the microstructural features of bulk material in the surface/near-surface regions. The convergent electron beam irradiates the sample and interferes with the matter, resulting in an emission of various signals from the waterdrop-shaped interaction volume (Fig. 2.8a). The magnitude of the interaction volume is mainly depend on factors, such as the acceleration potential, the incident angle of the electron beam and the atomic number [97]. The most frequently investigated signals for SEM are secondary electrons (SE), backscattered electrons (BSE), and characteristic X-rays.

SE are generally detected to demonstrate the topography of the sample surface. SE usually contain energy of less than 50 eV (usually within the range of 2-5 eV) and they are ejected from the near-surface depth of ~5-50 nm. Consequently, it enables a high spatial resolution of less than 1 nm. Different SEs are generated, classified as SE1, SE2 and SE3. Fig. 2.8b shows that the representative SE1 are secondary electrons emitted when struck out directly by the primarily incident electron from the atomic orbital. SE2 are electrons ejected from the sample surface by the final collide with the electron that has experienced inelastic scatterings several

times. SE3 are electrons originating from the chamber components that the BSE knock out. The location of the sample, surface roughness, atomic number, and energy of the injection beam can all influence the quality of the SE images.
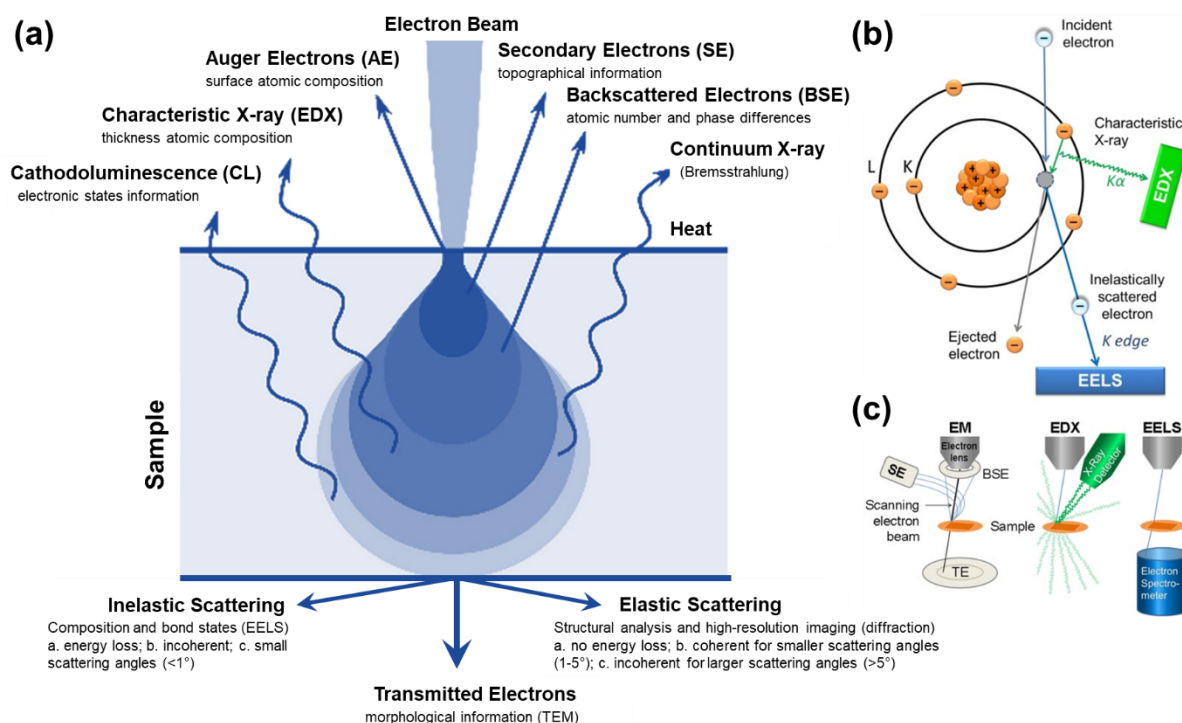

Fig. 2.8 (a) Schematic of incident electron beam interacting with the sample, emitting signals from the waterdrop-shaped interaction volume for sample characterization; (b) Generation of energy-dispersive X-ray spectroscopy (EDS/EDX) and electron energy loss spectroscopy (EELS) signals in electron orbital; (c) Positions for detectors of secondary electrons (SE), backscattered electrons (BSE) and energy loss electrons. Adapted and revised from [97, 98].

With an energy of more than 50 eV, BSE penetrate deeper than SE into the bulk and are reflected out from the surface by the electromagnetic field of the nucleus upon the injection of the primary electron beam [99]. BSE, exempted from the influence of the acceleration voltage, are mainly categorized into two kinds: the directly elastically scattered BSE without energy loss and the backscattered BSE after several inelastic scatterings [99]. The yielding of BSE depends on the tilt angle with respect to the incident beams and the atomic number of the specimen. Therefore, they are utilized for identifying and differentiating between multiple phases, exhibiting brighter images for elements with higher atomic numbers. Besides, the BSE yielding coefficient is enhanced with increasing tilt angle away from the direction of the primary incident beam. That is why the technique EBSD, based on the BSE, requires a good

sample quality, which means a flat surface with low roughness and no deformation layer.

Braking X-rays (also called "Bremsstrahlung x-rays") are generated when the primary electrons decelerate, which are noticed as the background signal with a continuum energy distribution in the spectrum. Another type of characteristic X-ray crucial in the EDS/EDX are formed when the incoming electron ejects the electron from the inner atomic shell and creates the electron hole. An electron from a higher energy shell would fill the hole and emit different energy and number of X-rays correlated with the species of the element. The emitted characteristic X-rays (Fig. 2.8b) are gathered by an energy-dispersive spectrometer (Fig. 2.8c) to analyze the chemical composition of the microstructural features as well as the relative quantity of the elements by investigating the unique set of peaks on its electromagnetic emission spectrum. Wavelength-dispersive X-ray spectroscopy (WDS) measures the characteristic X-rays within a small wavelength range that fulfills the Bragg's law.

Instead of the emission of characteristic X-rays, if an electron from a further outer shell absorbs the extra energy and prompts the ejection, it is the Auger electron. It occurs more frequently in light element with a lower atomic number than X-rays. The method that analyzes this auger electron is named auger electron spectroscopy (AES), which can also be applied to chemical analysis. In analogous to AES, in X-ray photoelectron spectroscopy (XPS), the kinetic energy and the number of eject electrons are adopted to measure the characteristic binding energy for further determination of the chemical status of the element.

2.3.2 Microstructural characterization of hydrogen

Various microstructural characterization techniques have been applied to investigate hydrogen, some of which are demonstrated as follows. The silver decoration and reduction method can visualize the spatial distribution of hydrogen on the metal surface by analyzing the surface deposited with silver that is reduced by the hydrogen. Therefore, the preferential hydrogen reversible/irreversible trapping sites can be identified readily. By combing with different microscopy, the *in situ* analysis of the silver decorated surface is possible, enabling investigation of the hydrogen diffusion kinetic [100]. This technique is based on the principle of the redox reaction between the diffusible hydrogen atom and the silver ions, as shown in the following formula:

$$Ag^{+} + H \rightarrow Ag\downarrow + H^{+} \tag{2.16}$$

Another similar method is called the hydrogen microprint technique (HMT) [101]. A specific monogranular nuclear AgBr emulsion coating has been deposited on the sample surface, acting as a reaction and observable layer. Reduced silver particles can be noticed after the reducing reaction, while the residuals will be eliminated by the subsequent illumination step [101].

Secondary ion mass spectroscopy (SIMS) was generally utilized to collect chemical information by bombarding the surface with an ion beam [102]. The intensity of hydrogen or its isotope ions embedded within the material could then be obtained by investigating the ejected species with a mass spectrometer, within which the element is distinguished based on the mass/charge ratio (m/Ze). By conducting this technique, a spatially resolved hydrogen map along the depth of the specimen could be captured. Analogous to this technique, a higher spatial chemical resolution in a near-atomic range can be achieved by the APT, although the analyzed volume is small (<1 μm^3). The evaporation of ions collected by a time-of-flight mass spectroscopy is achieved by applying an intense electric field to a sharp needle-shaped specimen. Afterwards, the 3D map can be constructed through this destructive method using a position-sensitive detector [43]. Another way of precisely characterizing hydrogen widely deployed is TEM. Coupling with the electron energy loss spectroscopy (EELS) technique, it is capable of visualizing hydrogen columns and hydride in atomic resolution [103].

As the present studies put more emphasis on the macroscopic mechanical and diffusion behavior of hydrogen in bulk alloys, a more detailed description will be applied to TDS, SKPFM [104] and KP-based potentiometric hydrogen electrode methods [105].

2.3.2.1 Thermal desorption spectroscopy (TDS)

Understanding the effect of hydrogen in steels is critical to thoroughly investigating the interaction of hydrogen with material and hydrogen trapping within all the microstructural features. One of the main methods is TDS, also known as temperature programmed desorption (TPD) or termed thermal desorption analysis (TDA), which is essential in investigating the thermodynamic and kinetic behavior of desorption/decomposition procedures [18]. Different hydrogen traps (e.g. dislocations, grain boundaries, interfaces and carbides, oxides) can be identified through a specific heating ramp as it is a microstructural constituent sensitive technique [81]. The thermally activated desorbed hydrogen is captured by a quadrupole mass spectrometer/pressure gauge within an ultra-high vacuum atmosphere. By analyzing the characteristic hydrogen desorption rate curves, which correlate with factors like specimen

dimension and heating rate, the amount of hydrogen within those traps can be quantitatively calculated. The binding energy for various hydrogen traps can be calculated applying different models of Oriani, McNabb & Foster or Kissinger [106].

However, the diffusive hydrogen is difficult to collect as the majority of it is leaked out during the transfer and setup of the machine, making it inappropriate for investigating the hydrogen diffusion behavior. This drawback can be compensated by deploying the KP-based potentiometric hydrogen electrode method with an *in situ* hydrogen electrochemically charging part to generate the constant hydrogen flow during the measurement. Besides, the visualization of the local distribution of hydrogen in various microstructural constituents is impossible, which can be achieved by the SKPFM.

2.3.2.2 KP-based technique

The standard Devanathan-Starchurski (DS) double cell (Fig. 2.9), conventionally applied for studying the permeation behavior of materials based on Fick's law, can accurately quantify the hydrogen content and deduce the hydrogen diffusion coefficient by measuring the hydrogen oxidation current, enabling analysis of the material with low hydrogen solubility and high hydrogen diffusivity [107]. However, as the deposited palladium layer for absorbing hydrogen is immersed in the electrolyte, damage caused by chemical and electrical erosion to this layer is unavoidable. Therefore, the non-destructive KP-based potentiometric technique is implemented in this PhD study, which can quantitatively measure the hydrogen content variation with a high spatial resolution (i.e. micro- and sub-microscale) by sensing the potential evolution originating from the formed hydrogen electrode on the sample surface [104, 105, 108-110]. Besides, the detected surface is exposed directly to a dry nitrogen-protective atmosphere, minimizing the instability for measurements conducted in the aqueous electrolyte for the DS double cell.

The principle of the KP-based potentiometric hydrogen electrode method is to measure the chemical potential variation rate of the hydrogen electrode generated on the surface of Pd; hence, the corresponding variation of hydrogen amount is determined. With higher hydrogen content, the corresponding potential is reduced [109]. The concentration of hydrogen in Pd is constrained up to around 2.4 at.%, above which the binary region is reached [105]. At this critical point, the potential stays static as well as the hydrogen potential in Pd due to the coexistence of hydrides α-Pd-H and β-Pd-H [109]. The KP-based potentiometric has

advantages: a) high hydrogen detection resolution and sensitivity; b) availability for the in-situ measurements; c) non-destructive characterization method without corrosive electrolyte contamination on the surface. The drawbacks of the method are the limited time window for measurements and the limited amount of absorbed hydrogen due to the formation of palladium hydride [111]. Based on the comparison with the TDS measurements in 5 wt. % Ni steel, Wu et al. [105] have verified that the analyzed potential was not influenced by the microstructure of the Pd layer (i.e. grain size, shape and orientation).
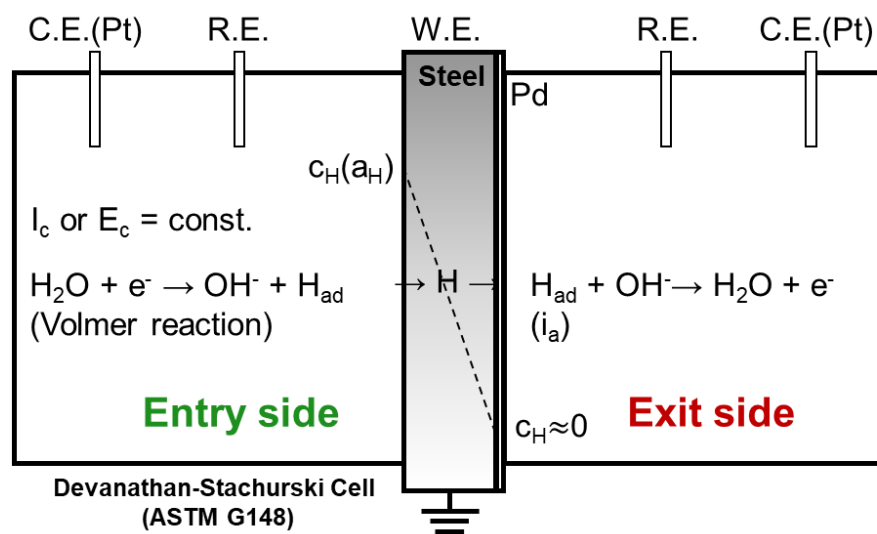
Fig. 2.9 Schematic of the standard Devanathan-Starchurski permeation double cell. Adapted and revised from [107, 111].

Atomic force microscopy (AFM)-based SKPFM has been applied in this PhD study. This technique has a higher spatial resolution lies in the tens of nanometer range depending on the SKP tip radius, enabling detection of the hydrogen distribution on the more delicate microstructural features [104, 108, 110, 112]. In addition, AFM-based SKPFM can detect the accumulated hydrogen with a low scale (<0.01 at.ppm) as the Pd layer with FCC nanocrystalline structure stores hydrogen by hydride formation [112]. This buffer function of Pd coating also mitigates the influence of the underlying inhomogeneous intrinsic oxide layer from the material. However, it is infeasible for hydrogen kinetic investigation as it takes some time to initiate the first scanning and the interval duration is relatively long, unable to resolve the diffusion procedure.

2.3.3 *In situ* **micromechanical techniques for HE investigation**

Conventionally, mechanical tests are conducted on the externally hydrogen-charged sample to

investigate the hydrogen effect. Due to the interval transfer step, the direct link between the hydrogen concentration and the hydrogen-introduced mechanical microstructure degradation phenomenon is difficult to build. Hydrogen outgassing is unavoidable, which causes the hydrogen concentration gradient along the depth. In most cases, the experiments are usually conducted in FCC materials with more considerable hydrogen reserving capacity and only the effects from the deeply trapped hydrogen can be observed [113]. Besides, the macroscopic tests are inappropriate for mechanically revealing the complex hydrogen effects on subtle crystalline imperfections like dislocation with the nanometer scale.

Therefore, *in situ* hydrogen charging methods have been applied recently in conjunction with high-resolution microscopy (e.g. SEM, AFM and TEM) investigation to unravel the hydrogen effect on the individual constituent. For example, plasma charging inside a SEM chamber has been brought up to study the fatigue crack evolution in ferritic alloys combined with *in situ* tensile tests [114]. However, the intensity of plasma is hard to control and quantify. In addition, it can introduce surface damage. Another technique is the environmental TEM, coupled with the cyclic compression device, which enables the *in situ* analysis of dislocation motion under compressive stress [59]. Nonetheless, quantifying the electron beam dissociated hydrogen is complicated, and the dimension of the TEM specimens restricts the analysis field.

Therefore, a promising *in situ* electrochemical nanoindentation (ECNI) technique was introduced by Barnoush and Vehoff in 2006 [60]. Nanoindentation is applied to obtain the mechanical response (e.g. hardness, elastic modulus, surface friction etc.) of the material in a small volume where HE takes place with a high lateral resolution of nano-/micrometer scale. Therefore, it can investigate the localized properties without the influence of other microstructural features (e.g. grain boundary interfaces, dislocations, pores, second phases) and the inhomogeneities area, even resolving the homogeneous dislocation nucleation. In addition, the post-characterization for the probed volume can be conducted by means of non-destructive, high-resolution electron microscopy techniques like EBSD, electron channeling contrast imaging (ECCI) or TEM [13–16]. A hydrogen-induced pop-in load reduction was observed by applying this technique in single-crystal Ni (111), Fe-40 at.% Al, Fe-3 wt.% Si, Al and Cu, indicating a reduction in the energy required for homogeneous dislocation nucleation supported by the "defactant" concept [2, 60, 62, 115]. However, as the electrolyte directly contacts the sample surface, surface erosion and stress localization are inevitable, which can be alleviated but not eliminated using a glycerol-based solution [116-119]. Besides, distinguishing the effect

of deeply trapped and diffusible hydrogen is challenging, as hydrogen charging and outgassing occur simultaneously. The test duration window is also limited as the surface condition is altered due to the electrochemical polarization [2, 60, 120].

New analysis tools are needed, combining high enough spatial and temporal resolution where the hydrogen effects initiate. In this PhD work, a novel *in situ* device has been applied for electrochemical backside hydrogen charging while performing time-resolved nanomechanical tests by nanoindentation to track independent hydrogen-metal interaction mechanisms on a small scale [61]. The electrochemically produced hydrogen is generated beneath the sample and reaches the testing (upper) surface by bulk diffusion. Therefore, the sample surface remains intact after hydrogen charging, which allows the post-mortem investigation of hydrogen effects by different characterization techniques without the second preparation of the sample surface. Using the hydrogel format electrolyte ensures that the generated hydrogen does not accumulate as bubbles, avoiding the detachment between the electrolyte and the specimen. The long-duration hydrogen charging of above 5 h with constant current density can be guaranteed as the electrolyte contact area remains constant. Thus, enough mechanical and electrochemical data can be collected for further studies with statistical reliability. It is worth mentioning that the setup is more appropriate to track the mechanical response of materials in a deeper depth as the hydrogen concentration is relatively low in the utmost surface region (tens of nanometers). The promising solution is keeping the whole system in an inert atmosphere, for example, assembling the backside hydrogen charging setup in an environmental nanoindentation machine with Ar atmosphere.

3. Materials and Experimental methods

3.1 Materials synthesis

The wet chemical measured elemental compositions of the studied ferritic alloys Fe-8 wt.% Cr, Fe-15 wt.% Cr, Fe-20 wt.% Cr and Fe-2 wt.% Al (denoted as Fe-9Cr, Fe-16Cr, Fe-21Cr and Fe-4Al in the whole PhD manuscript according to their composition in at.%) are displayed in Table 3.1. Experiencing hover melting, casting to a Cu mold, hot rolling at 1100 °C to a thickness of 4 mm, and the homogenization annealing at 1300 °C for four hours surrounded with an inert Ar protective atmosphere, the FeCr alloys are quenched in water after additional annealing at 800 °C for one hour to remove the Widmannstätten structure. After the heat treatment, the final single BCC phase material has a large grain (LG, with grain size larger than 500 µm) size and low dislocation (LD, with dislocation density less than 10^{13} m^{-2}) density. The grain sizes measured based on the EBSD images and the dislocation densities calculated from the ECCI images are listed in Table 3.2.

Table 3.1 Chemical composition of the materials investigated (in at.%). (The samples are called Fe-9Cr, Fe-16Cr, Fe-21Cr and Fe-4Al refering to at.%.)

Element	Fe	Cr	Al	C	O
Fe-9Cr	Balance	8.604	0.002	0.083	0.094
Fe-16Cr	Balance	15.924	0.002	0.010	0.072
Fe-21Cr	Balance	20.943	0.002	0.008	0.093
Fe-4Al	Balance	0.009	4.420	0.043	0.228

With only two weight percent of Al to stabilize the BCC lattice structure, Fe-4Al is utilized as the reference alloy with low content of the substitutional element. The Fe-4Al alloy, grown at MPIE by the modified Bridgman method (details are illustrated in [121]), owes a bicrystal structure with only one Σ5 (3 1 0)[0 0 1] grain boundary in the region near the middle of the sample. In FeCr alloys, various unique metallurgical and mechanical treatments were applied to obtain a sample with different dislocation densities and grain sizes for different research purposes. High dislocation (HD) density was achieved by cold rolling (CR) with different thickness reductions (i.e. 5 %, 10 % and 20 %) from the as-annealed FeCr alloy.

The specific sample with a small grain (SG, with grain size less than 1 µm) and LD density can be attained by high-pressure torsion (HPT) technique in combination with the following annealing treatment at 600 °C for 10 min. The Fe-9Cr alloy has a medium grain (MG, with grain size larger than 1 µm and less than 500 µm) size and low dislocation density.

Table 3.2 Grain sizes and dislocation densities for different materials. (The CR5 and CR10 alloys refer to the Fe-21Cr (LG, LD) alloys that have undergone cold rolling, with a thickness reduction of 5 % and 10 %, respectively.)

Alloy	Abbreviation representative	Grain size	Dislocation density (m^{-2})
Fe-9Cr (MG, LD)	MG: medium grain LD: low dislocation	(0.10±0.03) mm	(2.3±1.8)×10^{12}
Fe-16Cr (LG, LD)	LG: large grain LD: low dislocation	(1.13±0.09) mm	(2.6±1.9)×10^{12}
Fe-21Cr (LG, LD)	LG: large grain LD: low dislocation	(1.05±0.05) mm	(2.4±1.9)×10^{12}
Fe-21Cr (LG, CR5)	LG: large grain HD: high dislocation	(0.96±0.27) mm	(1.3±0.1)×10^{14}
Fe-21Cr (LG, CR10)	LG: large grain HD: high dislocation	(0.96±0.27) mm	(1.4±0.1)×10^{14}
Fe-21Cr (SG, LD)	SG: small grain LD: low dislocation	(0.30±0.14) µm	(3.7±0.6)×10^{13}
Fe-21Cr-LD	LD: low dislocation	(1.20±0.10) mm	(1.3±1.2)×10^{12}
Fe-21Cr-HD	HD: high dislocation	(1.10±0.10) mm	(8.7±0.5)×10^{13}

3.2 *In situ* electrochemically backside charging tests

3.2.1 Sample dimension and surface preparation

The sample applied to the *in situ* electrochemically backside charging nanoindentation setup was shaped by electrical discharge machining to a disk with a diameter of 12.4 mm and a thickness of 2.4 mm as displayed in Fig. 3.1. The sample surface deployed in nanoindentation and microstructural characterization using EBSD and ECCI has high surface requirements. The surface roughness needs to be less than 10 nm/µm. The surface was prepared by sequentially grinding with SiC papers (1000-4000 grit), mechanical polishing with diamond suspension until 1 µm, and chemo-mechanical polishing. To get rid of the remaining surface deformation layer of the sample introduced by machining and grinding preparation procedures, a V_2A agent etching agent was applied for 10 s on the surface before the final polishing for about one hour with a 0.25 µm colloidal silica suspension (OP-S, Struers). The surface roughness measured by AFM (Dimension^{TM} 3000) was < 1 nm/µm^2, analyzed by the Gwyddion software.
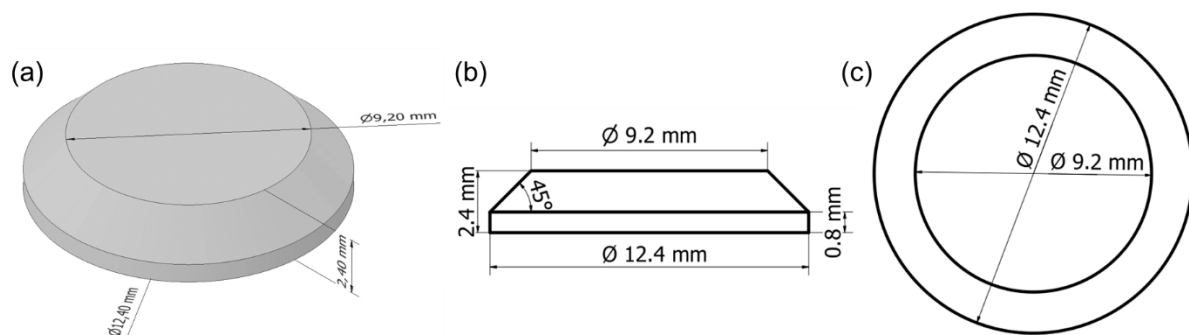
Fig. 3.1 (a) The three-dimensional sketch of the specimen. (b) The lateral view and (c) the top view of the specimen used in the *in situ* electrochemically backside charging setup.

3.2.2 Cathodic hydrogen charging

The *in situ* backside hydrogen charging setup was assembled inside the nanoindentation chamber for the mechanical tests as displayed in Fig. 3.2b. Hydrogen was produced by a three electrodes electrochemical system (details are presented in [61]), employing a hydrogel format electrolyte that was synthesized from the 0.1 M NaOH solution with 20 mg/L As_2O_3 to limit the hydrogen recombination reaction [122]. The bottom of the specimen (working electrode) is in contact with the solution. The electrolyte-contacted circular region has a diameter of 8 mm, less than the bottom diameter of the specimen (12.4 mm as shown in Fig. 3.1), avoiding the leaking out of the electrolyte. The counter electrode applied was a Pt plate with 1 cm^2 area

(99.9 % purity, Goodfellow). The transformation of the electrolyte from the liquid to hydrogel state occurs within a narrow temperature range of 70-80 °C after adding 10 wt.% Agar at around 50 °C to the solution. The appropriate potential was selected based on the cyclic sweep voltammetry tests, conducted commonly within the range of -1.7-0.3 V_{Ref} with respect to the Ag/AgCl reference electrode (World Precision Instruments, DRI-REF-2SH) at a speed of 50 mV/s (Fig. 3.2a). The monitoring and recording of the electrical data were accomplished by the Reference 600™ Potentiostat (Gamry Instruments). The potential was selected such that the current density reached the designated region of -0.5 to -5.5 mA/cm^2, where the hydrogen evolution reaction (HER) took place. Excessive hydrogen bubble generation was inhibited by the hydrogel format electrolyte in the meantime, ensuring the stability of the setup for more than five hours (Fig. 3.2c) [123, 124]. In addition, the body of the device was manufactured with Polychlorotrifluoroethylene (PCTFE), which has high stiffness, low water absorption rate and high corrosion resistivity, guaranteeing the feasibility of conducting mechanical testing by nanoindentation. The amount of hydrogen purged into the specimens is adjusted through the potential variation as a proportional relation was found between the polarized current density and the hydrogen activity [66, 67]. To inhibit the dissipation of the hydrogen and diminish the growth of the oxidation layer, an Ar flow via a pipe with a speed of 3.5 l/min was constantly blown to the sample surface.
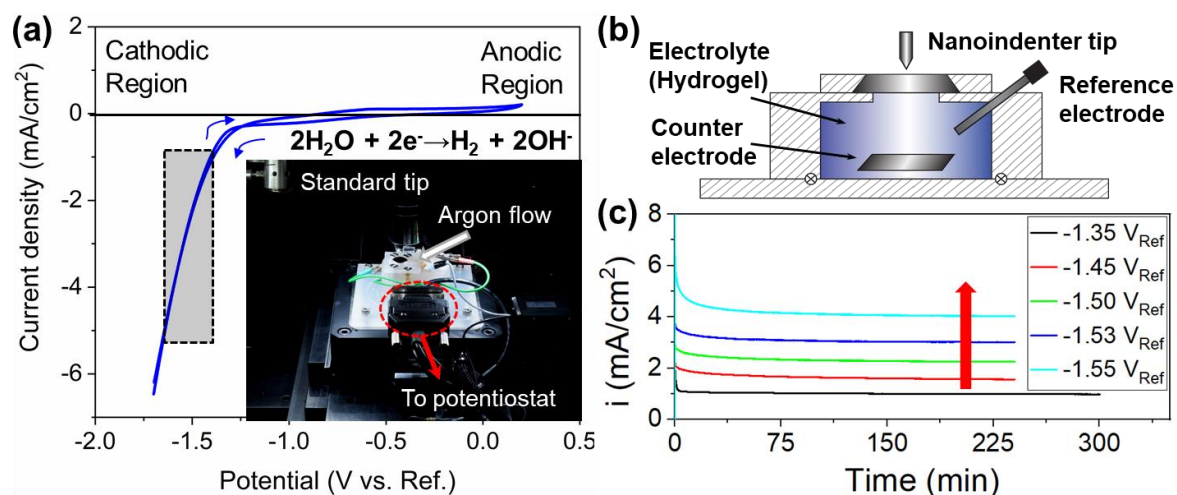
Fig. 3.2 (a) Cyclic voltammetry curve (-1.7-0.2 V_{Ref}) and picture of the cell in a standard nanoindentation device. (b) Schematic diagram of the electrochemical *in situ* backside hydrogen charging nanoindentation setup (reproduced from [61]). (c) Evolution of current density during potentiostatic charging at different cathodic potentials.

3.2.3 Mechanical tests

3.2.3.1 Nanoindentation

The mechanical tests in this PhD study were all carried out in a nanoindentation machine controlled by load (KLA/Agilent/Keysight Technologies, G200) based on the classical Oliver and Pharr's theory [125, 126]. The diamond indentation tips with Poisson's ratio of 0.3 and elastic modulus of 1140 GPa were purchased from the Synton-MDP company (Switzerland). This study also assumes a Poisson's ratio of 0.3 for steels. The creep effect is diminished by the holding segment of 5 s at the maximum loading in the load-displacement curve. Besides, the thermal-induced unexpected displacement has been compensated by the final 60 s holding at 90 % of the maximum load [127].

Two types of indentation experiments were conducted utilizing different indenter tips. Berkovich diamond indenter with a radius of around 400 nm simulated by the Hertzian model has been applied to acquire the hardness and Young's modulus evolution curves along the depth with continuous stiffness method (CSM) [128, 129]. With a maximum load of 10 mN, a harmonic displacement of 2 nm with 45 Hz frequency was adopted to the method. During the whole loading and unloading procedure, a strain rate of 0.1 s^{-1} was employed (defined by $\dot{\varepsilon}=\dot{h}/h\approx\dot{P}/2P$) [130]. The hardness and elastic modulus were extracted between the depth range of 250-350 nm.

A spherical tip with a radius of ~750 nm by Hertzian fitting was used to measure pop-in load, a sudden displacement burst in the load-displacement curve. The pop-in load is intimately correlated with the homogeneous dislocation nucleation for single crystal structured metals with low density of defects without phase transformation, crack initiation or oxide layer rupture, like in our case. The pop-in load can be used to compute the maximum shear stress [131]. The maximum indentation load of 3 mN was set with the strain rate of 0.1 s^{-1}. The pop-in load decreases with the pre-existing dislocations nearby as they promote the onset of plasticity [132]. To obtain good statistics for the maximum shear stress values of homogeneous dislocation nucleation, more than 50 indentations for one condition were performed for homogeneous dislocation nucleation investigation.

3.2.3.2 Micropillar compression

Micropillar compression tests were utilized to study the hydrogen effect on the FeCr alloys with a uniaxial stress state. The relatively large 5 µm pillars with a height-to-diameter aspect

ratio of 2 for reserving more hydrogen were manufactured on a plasma focused ion beam system (PFIB, FEI Helios), operating with a Xe source. Milling was achieved by applying a 30 kV Xe^+ ion beam from initial coarse milling with a current of 60 nA until final fine milling of 0.3 nA to reduce the taper angle of the pillars. The compression tests for the pillars were conducted with a strain rate of 7.5×10^{-3} s^{-1} by the G200 nanoindentation machine using a flat punch indenter (10 µm in diameter). The maximum aiming strain was 0.06 for samples with low dislocation density and 0.08 for the ones with high dislocation density, respectively. The strain was chosen when the first shear band was activated in pillars with the hydrogen-uncharged condition. After the pre-charge and release of the weakly trapped hydrogen, the continuous hydrogen charging was applied to the specimen until reaching the dynamic equilibrium state for the applied potential. The compression tests were conducted on pillars with different hydrogen-charged conditions. More than three pillars were tested in each condition to verify the reproducibility. For both conditions of LD and HD, the pillar compression was conducted with a current density of 3.6 mA/cm^2.

3.2.3.3 Nanoscratch

The hydrogen effect on the grain boundary has been analyzed through the nanoscratch tests. The scratch was conducted using a 5 µm spherical tip along the direction perpendicular to the grain boundary. Forward and backward wear track pairs were made for investigation. In each condition, at least two pairs of wear tracks were made to check the reproducibility of the experiments. The total length of the wear track is 200 µm, separated by the grain boundary into two 100 µm parts within each grain. With a passing velocity of 1 µm/s, a scratch with a maximum load of 20 mN was performed. The recognition of the profile in the z-axis was achieved by a final profiling procedure with a minor load of 20 µN. Before hydrogen charging, the reference wear tracks were made. Afterward, the nanohardness was collected with the Berkovich tip for both the reference stage without hydrogen charging and the hydrogen charging stage with a continuously applied constant current density of 1.67 ± 0.09 mA/cm^2. After reaching the dynamic equilibrium state, as elucidated in [133], the indenter was switched to the 5 µm spherical one to perform the nanoscratch tests. The final scratches were conducted after discharging for 7 hours to release the residual diffusive hydrogen. The applied binary ferritic alloy Fe-21Cr has a large grain size of around 1.2 mm with a low dislocation density ($<10^{13}$ m^{-2}) as measured by ECCI technique (see details in [133]). With the application of the confocal microscopy (VK-X1000, Keyence), the lateral profile of the wear tracks was measured and analyzed by the software MultiFileAnalyzer.

3.3 Hydrogen characterization

3.3.1 Thermal desorption spectroscopy (TDS)

Hydrogen quantification of the studied alloys has been fulfilled by the TDS measurements conducted in a Hiden TPD Workstation. Disk specimens with a thickness of around 1.1 mm and a diameter of 10 mm were mechanically ground with SiC papers until 2000 grit to remove the oxide layer. The thickness was measured three times by optical microscopy for each sample to assure reproducibility. Much thinner samples guarantee homogeneous heating for hydrogen release. After external electrochemical hydrogen charging with a current density of 2 mA/cm^2 for four hours, ensuring the thorough filling of hydrogen within the materials, samples were immediately taken out from the solution containing 3 wt.% NaCl and 0.3 wt.% NH$_4$SCN. The NH$_4$SCN is also a hydrogen recombination poison, inhibiting the formation of molecular hydrogen and enhancing the uptake of hydrogen in the materials [113]. The intermediate preparation time required for the machine and samples, like rinsing with acetone and deionized water, recording the weight by the electronic scale, as well as evacuating the TDS chamber till ultra-high vacuum of ~10^{-6} Pa, has been shortened to roughly 20 min. The hydrogen released from the sample at various temperature regions can be collected and calculated with a heating rate of 16 °C/min from room temperature to 750 °C.

3.3.2 KP-based potentiometric analysis of hydrogen

Fig. 3.3a shows the schematic diagram of the KP-based *in-situ* permeation setup used to measure the hydrogen diffusion coefficient through the steel based on the potential variation of the surface hydrogen electrode. This PhD study investigated two kinds of hydrogen diffusion coefficients, the apparent diffusion coefficient (D_{app}) and the mixed diffusion coefficient (D_{mix}), as exhibited in Fig. 3.3b. The apparent diffusion coefficient evolves the effects from irreversible hydrogen, reversible hydrogen and interstitial diffusive hydrogen, while the mixed diffusion coefficient takes only the mobile hydrogen into account (i.e. diffusive and reversibly trapped hydrogen). Two kinds of samples were cut to fulfill different purposes. Samples for measuring the mixed hydrogen coefficient owe the same dimension as that used in the *in situ* backside charging setup. The other type of disk sample has a thickness of around 1.1 mm and a diameter of 10 mm as applied in TDS experiments. Both sides of the sample were mechanical ground firstly with a 2000 paper, followed by a 4000 grit SiC paper to ensure the removal of the oxide layer and the flatness of the sample surface for further Pd physical vapor deposition (Leybold Univex 450).

The setup mainly comprises the upper part for hydrogen generation and the bottom part for measuring the potential on the exit side of the targeted material by KP microscope from the Wicinski & Wicinski Surface Scanning System. The sample is electrochemically charged with hydrogen from the top part of the cell, which contains three electrodes of 12.5 cm reference electrode Ag/AgCl produced from the Metrohm company, sample working electrode and platinum foil counter electrode (99.99 %, 25 µm thick, 12.5 cm^2). The electrolyte applied has the same composition as in the *in situ* backside hydrogen loading frontside nanoindentation setup, containing 0.1M NaOH and 20 mg/L As$_2$O$_3$. During the hydrogen charging with an applied potential of -1.52 V_{Ref} to achieve a current density of around 2 mA/cm^2, dry nitrogen (with a humidity of 0 rh%) is continuously purged into the electrolyte as well as the bottom chamber that encounters the exit side of the sample [104]. The tested material, the exit side covered with a 100 nm layer of Pd, is sealed by an O-ring with a diameter of 4 mm from the electrolyte (12.57 mm^2 contact area). The KP tip is fabricated by Ni80Cr20 alloy with further electropolishing to the final diameter of 100 µm.
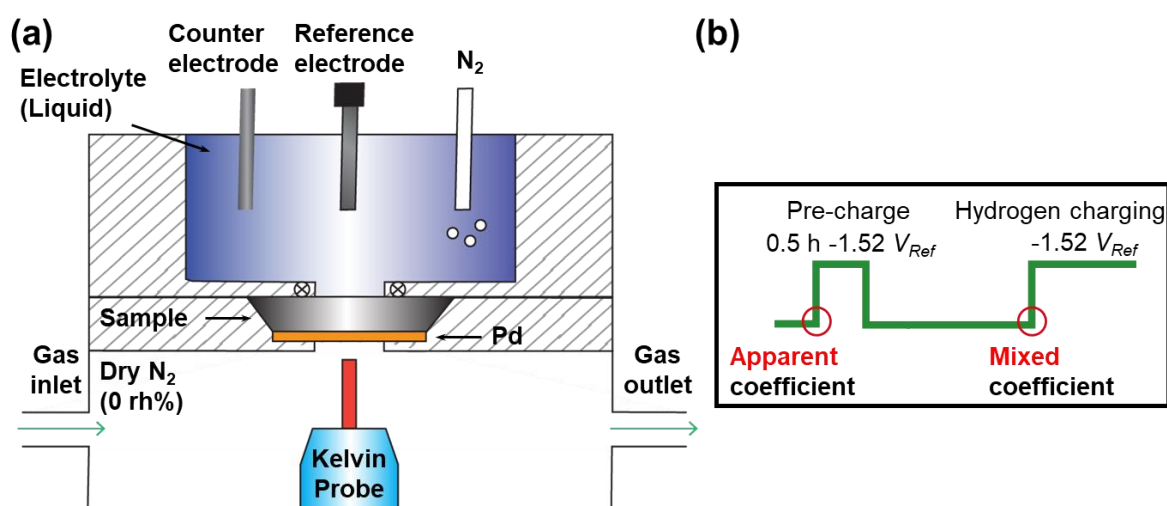
Fig. 3.3 (a) Schematic of the KP-based potentiometric hydrogen electrode permeation setup (Kelvin probe with a diameter of 100 µm made from Ni80Cr20). Adapted and revised from [134]. (b) Procedure for obtaining the apparent diffusion coefficient and the mixed diffusion coefficient.

Once the induced hydrogen exceeds ~2.4 at.% at room temperature, a Pd hydride (i.e. β-H-Pd) will form, coexisting with the soluble α-Pd-H [109]. The potential at this state is treated as the reference potential for KP microscope calibration. The total potential in this material,

depending mainly on the surface condition and preexist hydrogen content, alters between 0.3 to 0.6 V. Therefore, after several trials and tries, the hydrogen pre-charge duration to fill reversible hydrogen traps is set to 0.5 h when the system reaches roughly half of the saturation potential.

3.3.3 SKPFM

The existence and spatial distribution of hydrogen on the micropillar surface have been visualized by the SKPFM. Besides, the hydrogen desorption procedure was investigated through the KP potential variation. The dimension of the sample was the same as the one applied to the *in situ* backside hydrogen charging device. After final chemical mechanical polishing with colloidal silica suspension, the sample was coated with 100 nm Pd by physical vapor deposition (Leybold Univex 450), followed by the PFIB milling (FEI Helios) of the 5 µm pillars. The measurement was realized by a Keysight Technologies 9500 Scanning probe microscope and the data analysis was conducted by the software Keysight Nano Navigator (version 1.8.2). The SKPFM detected the potential changes in the targeted area of the specimen, with a high resolution of nanometer range depending on the scanning tip radius and non-contact mode of AFM [135]. Before being assembled into the environmental SKPFM chamber with a dry nitrogen atmosphere (0 rh%), the sample was continuously backside hydrogen charged for 4 hours with a current density of ~2 mA/cm^2, which was analogous to the charging conditions during the nanoindentation tests. Afterward, the first SKPFM potential mapping was obtained within one hour after taking the sample from the set-up.

3.4 Material characterization

3.4.1 SEM & ECCI & EBSD

The microstructure features were characterized by SEM, ECCI and EBSD. The dislocation content was analyzed using a field-emission crossbeam MERLIN SEM produced by Carl Zeiss AG company, applying the ECCI technique with an accelerating voltage of 30 kV and a beam current of 4 nA. The high resolution imaging for dislocation observation was achieved by a working distance of around 7 mm in the sample with a fresh, well-polished surface as it is oxide layer sensitive. EBSD was conducted in a Jeol JSM 6490 machine with an accelerating voltage of 15 kV to grasp the crystallographic information. The post-analysis of the data (e.g. the Euler angle and crystal structure) obtained from EBSD was realized by the TSL-OIM software (EDAX). Combo-scanning was applied to acquire EBSD mapping over a few millimeter range.

The mismatch lines between segments of EBSD images originate from the minor shift occurring once the stage position changes, as stage movement is necessary during one combo EBSD scanning.

3.4.2 TEM sample preparation and imaging

The TEM lamella lifted out from the cross-section region underneath the nanoindentation imprints was prepared by a dual-beam FIB with a Ga-ion resource (Scios 2, Thermo Fisher Scientific). The coarse milling was operated at 30 kV with a current of 5 nA, followed by the stepwise reduced current density to obtain a TEM foil with a thickness of 100-150 nm. Before the TEM analysis, a final polishing was required with a voltage of 2 kV and a current of 27 pA for 5 min to remove the oxide layer. In this study, images were taken by employing bright-field scanning transmission electron microscopy (STEM) at a voltage of 200 kV in a Jeol JEM 2200FS machine supplied with an omega energy filter. By adjusting the slot to a width of ~20 eV, low-loss energy-filtered images were captured. Combining with the unfiltered images captured without applying the filter, the foil thickness can be computed by the log-ratio method [136]. Images were processed by the software Fiji [137].

3.4.3 Transmission Kikuchi diffraction (TKD)

The spatial resolution of TKD, also called transmission EBSD (i.e. t-EBSD), has improved one order of magnitude compared with the conventional EBSD technique [138]. The cross-section of the wear tracks was examined through the TKD technique with a tilt angle of around 20° towards the detector as the specimen is transparent to the electron beam. Lamella with the same thickness as the TEM foil in a perpendicular direction underneath the grain boundary was taken out by the Scios 2 equipment, as mentioned in the TEM foil preparation section. The TKD scanning was performed by the MERLIN SEM at an accelerating voltage of 30 kV, a current of 2 nA, a working distance of around 5.5 mm, and a sample-to-detector distance of around 17 μm. A resolution of ~10 nm was achieved as characterized by the Bruker Quantax EDS software, embedding with EBSD analyzing kit. An advanced investigation of EBSD data has been conducted with the MTEX toolbox built in MATLAB.

3.4.4 X-ray photoelectron spectroscopy (XPS)

The chemical composition of the oxide film was measured by X-ray photoelectron spectroscopy (XPS, Physical Electronics, PHI Quantera II spectrometer). The X-ray source is a monochromatic Al Kα with an energy of 1486.74 eV. For each condition, the experiments

were performed in 3 different regions to check for reproducibility. The Ar^+ sputtering rate was kept at 3.48 nm/min with an X-ray beam size of 100×100 µm^2. The XPS data were explored with the software CasaXPS [139]. The binding energy for the chemical elements was referenced to the C-C signal (284.8 eV).

4. Diffusible hydrogen and its impact on nanohardness and dislocation structure in FeCr alloys by *in situ* nanoindentation

<u>This section is based on Manuscript 1:</u>

J. Rao, S. Lee, G. Dehm, M.J. Duarte, *Hardening effect of diffusible hydrogen on BCC Fe-based model alloys by in situ backside hydrogen charging.*

4.1 Introduction

The understanding of diffusive hydrogen is critical in ferritic iron as hydrogen has a high diffusivity and low solubility in bcc Fe alloys, which are therefore highly susceptible to hydrogen embrittlement [14, 31-33]. The diffusivity of hydrogen in undeformed α-Fe is between 10^{-5} to 10^{-4} cm^2/s [26]. Unlike the trapped hydrogen, the mobile hydrogen tends to diffuse into the stress localized region, resulting in the failure of the material.

Many *Ex situ* hydrogen charging experiments have already been adopted in investigating the mechanical properties and microstructural changes in materials with high hydrogen solubility and low hydrogen diffusivity, such as fcc-structured austenitic steel AISI 304L [140]. However, the hydrogen concentration gradient is inevitable using the external hydrogen charging methods [113]. The development of *in situ* hydrogen charging apparatus to studying bcc material become rather critical in exploring the hydrogen effects in those materials with high hydrogen diffusivity. As introduced by Barnoush and Vehoff [60], *in situ* hydrogen charging combined with nanoindentation method has been widely employed. With hydrogen charging and nanoindentation take place on the same side of the specimens, Barnoush and Vehoff [60, 115] found a pop-in load decrease in single-crystal Ni (111), Fe-40 at.% Al, Fe-3 wt.% Si, Al and Cu during hydrogen charging. They attributed this phenomenon to the reduction of the dislocation line energy by hydrogen ("defactant theory" [62]), causing a easier homogeneous dislocation nucleation [2]. However, the occurrence of chemical reactions is unavoidable, which might alter the microstructure chemistry or surface topography of the specimen, introducing stress localization [118, 119].

A hydrogen-induced hardening effect was observed by Zhao et al. [141, 142] in a high-entropy alloy and austenitic stainless steel. Besides, in Ni-based alloy [143], super duplex [144], Fe-22Mn-0.6C [145] and AISI 316L stainless steels [146], Fe–26Al–xCr intermetallics [147] and

nickel alloy 718 [148], the hardening effect correlated with hydrogen are also noticed. The hardness increase was explained by increased lattice friction and solid solution strengthening.

In this study, we have applied a novel *in situ* backside hydrogen loading frontside nanoindentation setup to systematically investigate the hydrogen effects on the deformation and mechanical properties of single-phase ferritic Fe-16Cr, Fe-21Cr and Fe-4Al alloys. Without contacting the electrolyte, the sample surface remains unaltered throughout the experiment, allowing for further microstructural characterization with high resolution techniques. With designed experimental procedure, we are able to exclude the influence from trapped hydrogen, only impact from mobile hydrogen can be studied. The dynamic effect of hydrogen charging on mechanical properties as a function of time has been fully investigated.

4.2 Results and interpretation

4.2.1 Microstructure of the materials
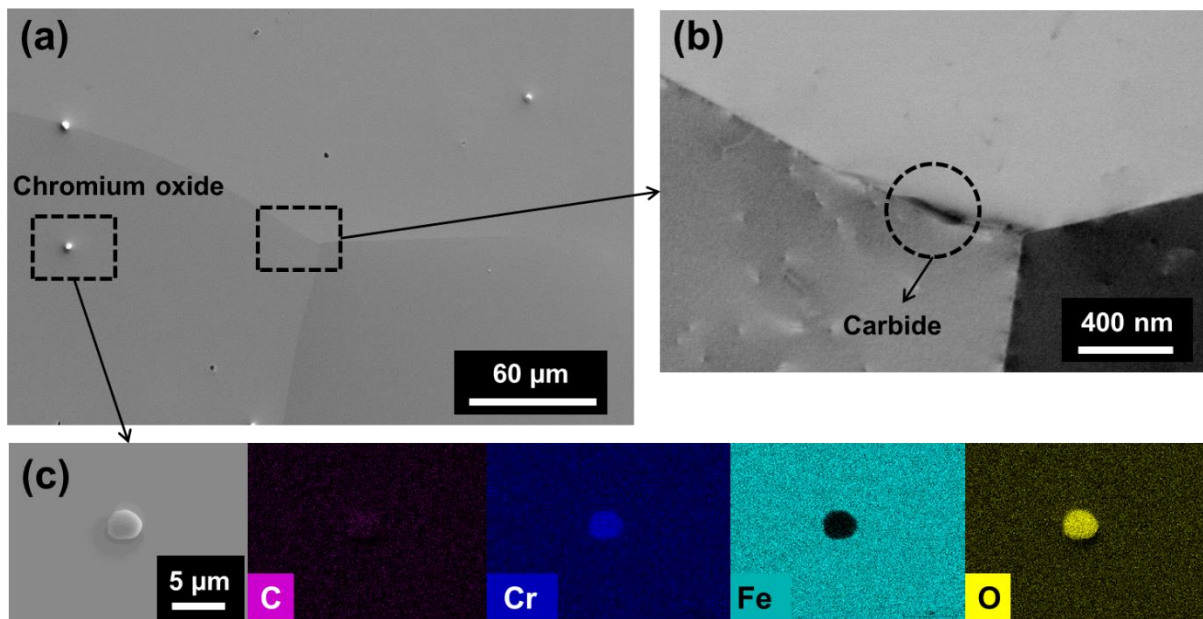
Fig. 4.1 (a) Representative SEM images of Fe-21Cr microstructural features. (b) Carbide sits along the grain boundary with size of ~40×200 nm^2. (c) EDS analysis of the chromium oxide with size of ~4 µm locates in the grain matrix.

Fig. 4.1 shows the microstructure of the sample surface characterized by SEM and electron dispersive spectroscopy (EDS), chromium oxides (~4 µm) locate within the grain matrix, and

carbides (~40×200 nm^2) sit along the grain boundary. The diameter of the indentation imprint is smaller than the average dislocation spacing so that indenting a region with no preexisting dislocations is possible.
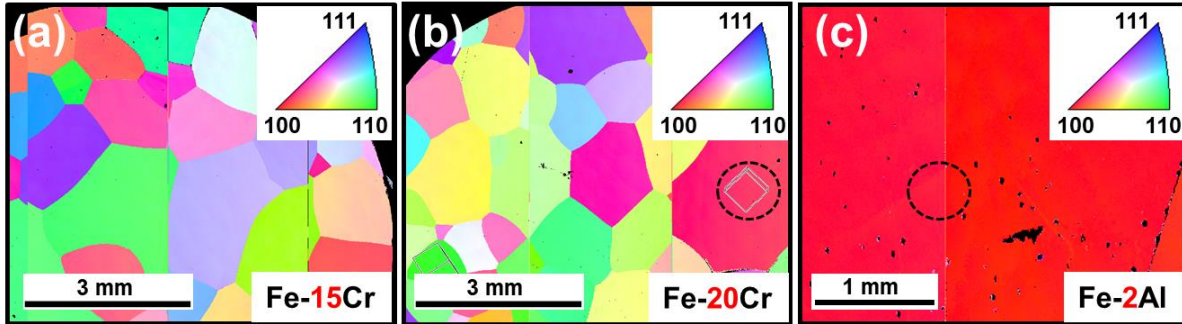
Fig. 4.2 Representative EBSD ND-IPF maps of (a) Fe-16Cr, (b) Fe-21Cr and (c) Fe-4Al, used to select specific grain orientations for nanoindentation tests.

The orientation map was generated using the TSL software. Three defined grains with misorientation of less than 8° to (100), (110) and (111) (i.e. [001], [110], [111]//ND, respectively) in Fe-16Cr and Fe-21Cr were chosen as shown in the normal direction-inverse pole figure (ND-IPF) in Fig. 4.2. The measured Euler angles (φ1, Φ, φ2) of the chosen grains are listed in Table 4.1.

Table 4.1 Crystallographic orientations of the investigated grains.

Sample		φ1 (deg)	Φ (deg)	φ2 (deg)
Fe-4Al	(100)a	120.1	91	178.5
Fe-16Cr	(100)(a,b)	244.4	172.9	138.2
	(100)a	245.5	88.3	1.7
	(100)(b,c)	124.2	95.1	177.4
Fe-21Cr	(110)a	121.7	133.0	268.5
	(111)a	102.3	124.4	41.5

4.2.2 Influence of hydrogen on the mechanical properties

Reference (black) and during hydrogen exposure (red), load-displacement representative

curves for Fe-4Al (100), Fe-16Cr (100) and Fe-21Cr (100) are shown in Fig. 4.3a, b and c, respectively. Hardness and Young's modulus were averaged at depth values between 250-350 nm, highlighted by the grey area and magnified in the corresponding insets. The top curves in Fig. 4.3d-f show the hardness (red) and Young's modulus (blue) evolution as a function of time. Each dot corresponds to a single nanoindentation test. The bottom curves (green) show the corresponding average current density recorded during potentiostatic hydrogen charging at a given potential (examples of these curves were given in Fig. 3.2c).
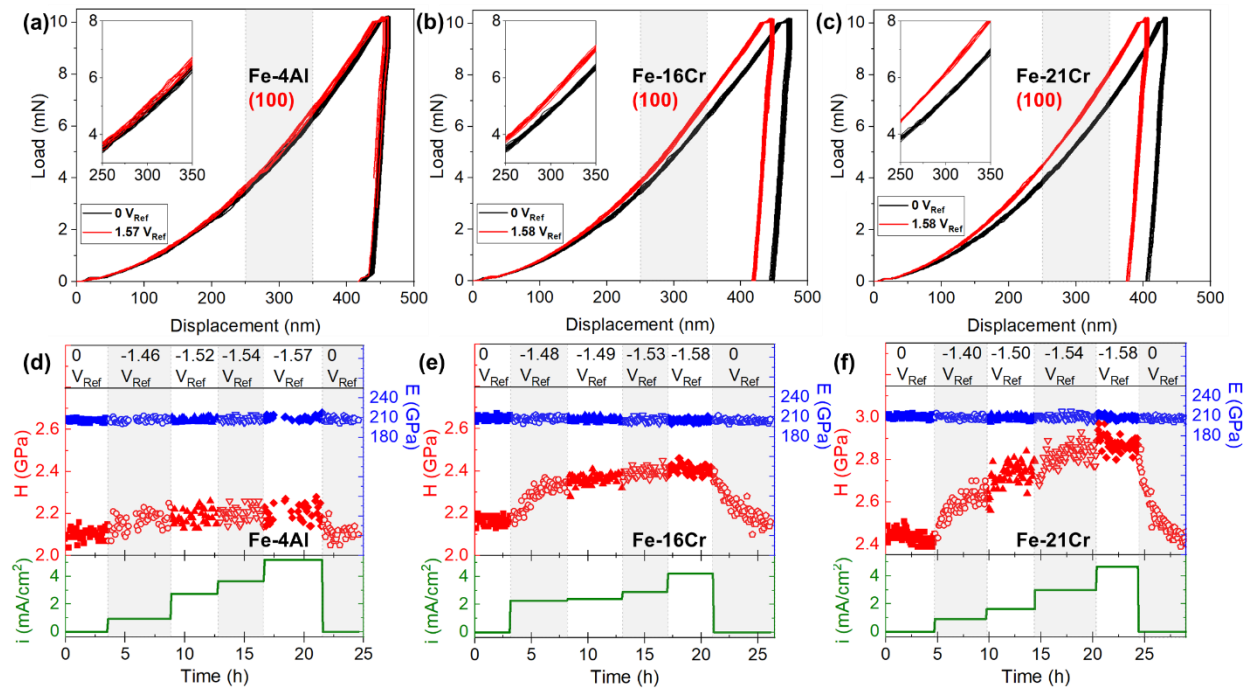
Fig. 4.3 Representative nanoindentation load-displacement curves of reference data (black) and during hydrogen charging (red) at the specified potential for (a) Fe-4Al (100)a, (b) Fe-16Cr (100)b and (c) Fe-21Cr (100)c. Labels *a*, *b* and *c* after the grain orientations refer to specific grains presented in Fig. 4.5 and Table 4.1. Hardness (red) and Young's modulus (blue) evolution and average current density (green) measured for different potentials in (d) Fe-4Al, (e) Fe-16Cr and (f) Fe-21Cr. Different symbols in the hardness and Young's modulus data represent different charging potentials.

A gradually increased hardness due to hydrogen is visible in the three studied alloys. During the first hydrogen charging stage, the hardness increased following a sigmoidal shape that correlates with the hydrogen diffusion behavior and stabilized in a plateau at which the quasi-equilibrium state of the absorbed and desorbed hydrogen permeation flux is reached. Because of the Fe-base bcc structure with high hydrogen diffusivity, the difference in the diffusion

coefficient of three studied alloys is expected to be minor, and on the order of magnitude of $\times 10^{-10}$ m^2/s as reported in [61]. To consider these differences in the diffusion behavior during the initial charging, the averaged hardness and Young's modulus shown hereafter are thus collected after hydrogen distributes homogeneously in the sample surface (i.e. when reaching the plateau), which contains more than 20 data points for each polarization condition. Stabilizing the hardness values upon hydrogen release requires about 60 % longer time than hydrogen charging. The hardness value takes ~2.6 h to reach the first plateau for the Fe-16Cr alloy; this time varies depending on the composition (Fig. 4.3e). A longer duration of ~4.2 h is required for hydrogen release from the specimen until the hardness drops back to the initial reference value. The longer duration for hydrogen releasing can be explained by a slower release of hydrogen from flat trapping sites and deeply trapped hydrogen.
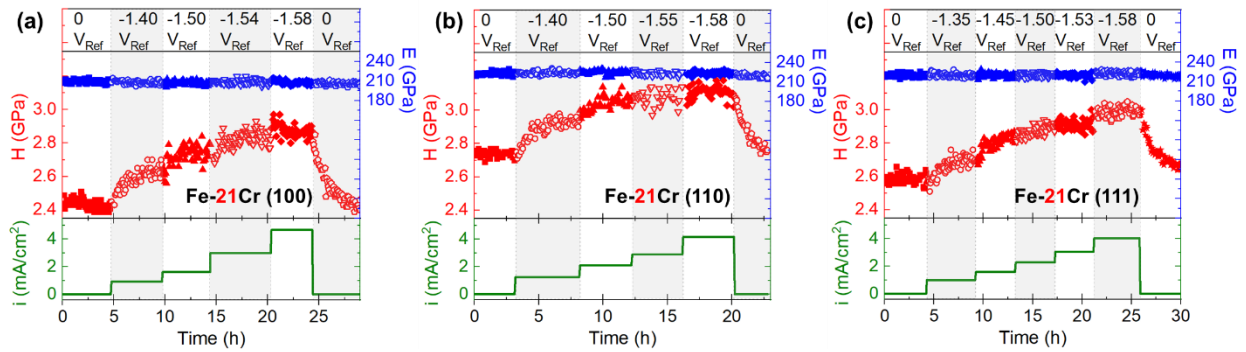
Fig. 4.4 Hardness (red) and Young's modulus (blue) evolution and average current density (green) for different potentials in Fe-21Cr with different grain orientations of (a) (100), (b) (110) and (c) (111). Different symbols in the hardness and Young's modulus data represent different charging potentials.

The Fe-4Al (100) alloy in Fig. 4.3d shows that during the first hydrogen charging stage, with a current density of 0.93 ± 0.04 mA/cm^2, the hardness turns to a constant value of 2.19 ± 0.03 GPa. Compared with the reference condition of 2.10 ± 0.03 GPa without hydrogen, the hardness increased by 4.3 %. The hardness rises only to 2.20 ± 0.04 GPa (4.7 % rise) when the charging current density reaches the maximum value of 5.21 ± 0.03 mA/cm^2, which shows that an increased hydrogen supply does not affect further the mechanical behavior and that the effect of hydrogen is small in the Fe-4Al alloy. The measured Young's modulus stays unchanged considering the error bars, with 206 ± 2 GPa for the reference state and 209 ± 3 GPa for the hydrogen charged conditions (Fig. 4.3d). Similar behaviors are observed for the Fe-Cr alloys. For Fe-16Cr (100) (Fig. 4.3e), the hardness increases from the reference condition

2.17 ± 0.02 GPa to 2.42 ± 0.02 GPa (11.5 % enhancement) during charging with the highest current density used of 4.21 ± 0.05 mA/cm^2. In contrast to the hardness, Young's modulus remains constant with values of 208 ± 3 GPa (reference state) and 205 ± 2 GPa (during hydrogen charging). The most pronounced hardening effect is observed in Fe-21Cr (100), where the hardness increases by 17.8 %, from 2.43 ± 0.03 GPa in the reference state to 2.86 ± 0.02 GPa by applying a potential of -1.58 V_{Ref}, that corresponds to a current density of 4.66 ± 0.02 mA/cm^2 (Fig. 4.3f). Again, the Young's modulus remains invariable at 208 ± 2 GPa.

The hydrogen effect on different grain orientations is investigated by applying the same hydrogen charging procedure to Fe-21Cr with different grain orientations of (100), (110) and (111), respectively in Fig. 4.4a-c; note that the range of hardness variation is the same for the three figures. Fe-21Cr (100) (Fig. 4.4a) is the same as Fig. 4.3f. Regarding the Fe-21Cr (110) alloy (Fig. 4.4b), the hardness enhanced from the initial 2.74 ± 0.02 GPa to 3.13 ± 0.02 GPa at a current density of 4.18 ± 0.02 mA/cm^2 (14.2 % increase) and the Young's modulus keeps at 224 ± 2 GPa. For the orientation of (111) in Fe-21Cr (Fig. 4.4c), an increase from 2.59 ± 0.03 GPa without hydrogen charging to a hardness of 2.99 ± 0.03 GPa is achieved by charging the sample reaching a current density of 4.04 ± 0.02 mA/cm^2 (15.5 % rise in hardness).
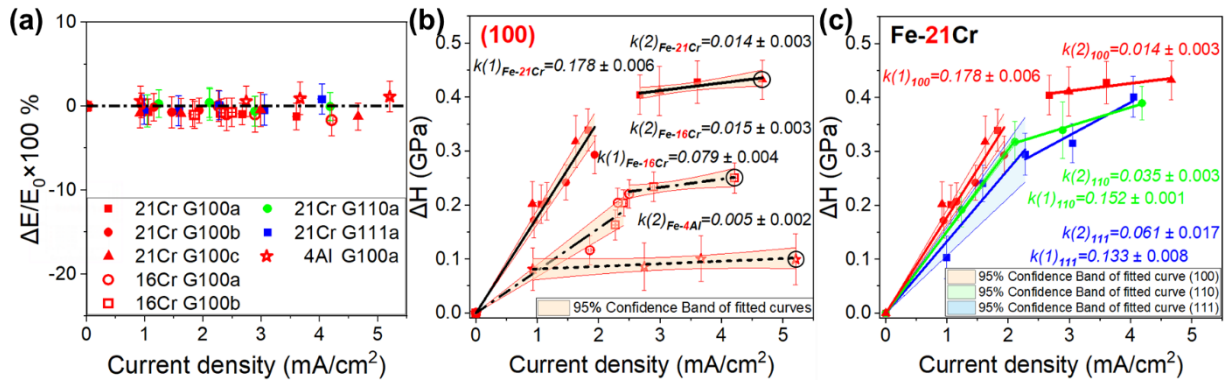
Fig. 4.5 (a) Relative variation of Young's modulus, $\Delta E = E_i - E_0$, normalized by the reference value E_0 of the hydrogen-free Fe-4Al, Fe-16Cr and Fe-21Cr samples. Different numbers indicate different grain orientations: G100 are (100) oriented grains (red data points), G110 (110) (green), and G111 are (111) grains (blue). For each orientation, up to three grains were measured, indicated by the letters *a*, *b* and *c*. (b) Comparison of relative hardness, $\Delta H = H_i - H_0$, normalized by the reference H_0 of the hydrogen-free Fe-4Al, Fe-16Cr and Fe-21Cr samples within the same grain orientation of (100). (c) $\Delta H/H_0$ evolution tendency in three grain orientations of (100), (110) and (111) in Fe-21Cr. *k* denotes the slope of the fitting curves, *k(1)* stands for the initial stage, while *k(2)* represents the second stage of hardness evolution.

Fig. 4.5 summarizes the data of the three alloys, including different grain orientations. For all cases, the elastic modulus remains constant with a maximum deviation of 1.7 % (Fig. 4.5a), which is within the accuracy of the measurements. The corresponding symbols for the specific three conditions displayed in Fig. 4.3d-f are circled with solid black lines in Fig. 4.5b. Fig. 4.5b shows the hardening effect obtained in (100) oriented grains for Fe-4Al, Fe-16Cr and Fe-21Cr during hydrogen charging. ΔH is defined as $\Delta H = H_i - H_0$, with H_i being the hardness at a given current density and H_0 the reference hardness without hydrogen charging. The hardness initially increases linearly upon increasing the current density, corresponding to a higher amount of hydrogen introduced into the samples. There exists a turning point for the increasing tendency with applied current density between the range of 2-3 mA/cm^2, above which the slope of the absolute hardness experiences a drastic decrease, indicating an establishment of a quasi-equilibrium state for introduced and releasing hydrogen flux. An increase of flow stress was also shown experimentally in Fe-17wt.%Cr steel at room temperature by a tensile test conducted on an electrochemically charged sample [149]. Additionally, the material with a higher Cr content exhibits a higher hardening effect with the same current density applied. The magnitude of the hydrogen effect for different alloy compositions can be compared by calculating the slope of the initial linear increase in hardness with increasing charging current density. With the grain orientation of (100), the slope of Fe-21Cr for the first stage $(k(1)_{Fe-21Cr})$ is 0.178 ± 0.006, which is almost twice the value of Fe-16Cr $(k(1)_{Fe-16Cr})$ that is 0.079 ± 0.004. Above the transient region of 2-3 mA/cm^2, the second stage slope approaches a similar value of 0.014 ± 0.003 $(k(2)_{Fe-21Cr})$ and 0.015 ± 0.003 $(k(2)_{Fe-16Cr})$ in Fe-21Cr and Fe-16Cr, respectively. Although only a couple of values could be collected for Fe-4Al, the $k(2)_{Fe-4Al}$ can be calculated as 0.005 ± 0.002. The increase in hardness change (ΔH) when charged with hydrogen above the turning region (> 2-3 mA/cm^2) at 3 mA/cm^2 based on Fig. 4.5b for Fe-4Al, Fe-16Cr and Fe-21Cr with (100) grain orientation was calculated from the fitting curves. Fe-21Cr possesses the highest enhancement of 16.7 ± 0.3 %, while Fe-4Al has the lowest increase of 4.3 ± 0.1 %. The intermediate incremental of hardness occurs in Fe-16Cr with 10.8 ± 0.1 % increase.

The anisotropy on the hydrogen-induced hardening effect for different grain orientations of (100), (110) and (111) was investigated for the Fe-21Cr alloy (Fig. 4.5c). The initial slope of the (100) grain has the highest value of 0.178 ± 0.006, while the (111) grain owns the lowest slope of 0.133 ± 0.008, with an intermediate value for the (110) grain of 0.152 ± 0.001.

4.2.3 Influence of hydrogen on the microstructure beneath the imprint

Since an advantage of the backside charging setup is that the top surface of the specimen used for indentation testing stays pristine even after hydrogen charging, the change in hardness must be reflected by the deformation structure underneath the indent. Here, pristine means free from the influence of effects other than hydrogen, such as surface contamination due to the elements contained in the electrolyte in contact with the surface, as well as increased surface roughness and possible corrosion caused by other hydrogen charging methods. Therefore, the front surface roughness of Fe-21Cr before and after the experiments during hydrogen charging stays unaltered (< 1 nm/μm² on average) as measured by atomic force microscopy in Duarte et al. [61]. The chemical composition of the specimen before and after the hydrogen charging has been investigated by X-ray photoelectron spectroscopy (XPS)* as shown in Fig. 4.6.
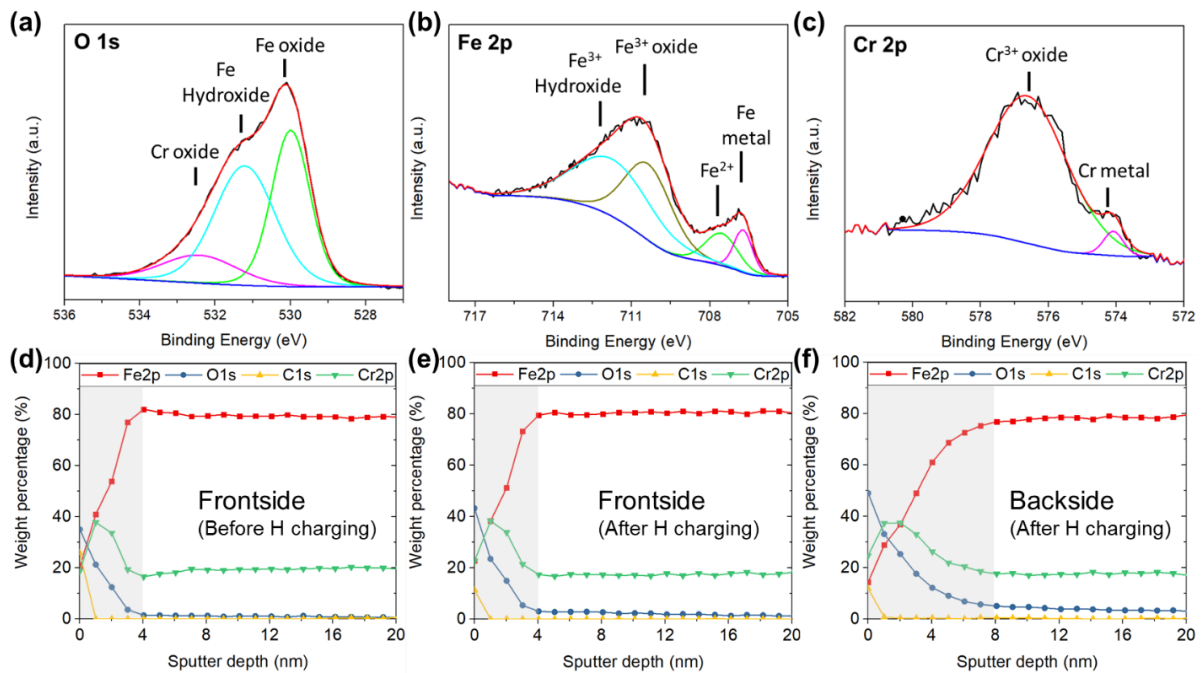
Fig. 4.6 XPS spectra of Fe-21Cr before hydrogen charging: (a) O 1s; (b) Fe 2p; (c) Cr 2p. XPS sputter profile of Fe-21Cr: (d) the frontside before hydrogen charging; (e) the frontside after hydrogen charging; (f) the backside, in contact with the electrolyte, after hydrogen charging.

The chemical state of the sample surface characterized by XPS surface spectra is exhibited in Fig. 4.6a-c for the reference (uncharged) specimen. The oxide layer thickness of the frontside (without contacting the electrolyte) both before and after hydrogen charging, as well as of the backside (contacting with the electrolyte) after hydrogen charging, is determined by XPS sputter profile (Fig. 4.6d-f). The surface of Fe-21Cr is mainly composed of Cr oxide, Fe

hydroxide and Fe oxide (Fig. 4.6a). In accordance with database [150], Fe $2p_{3/2}$ XPS data shown in Fig. 4.6b could be deconvoluted into 4 components of metallic Fe (706.8 eV), Fe^{2+} (708.2 eV), Fe^{3+}-O (711.1 eV) and Fe^{3+}-OH (713.2 eV). Cr $2p_{3/2}$ XPS data (Fig. 4.6c) is composed of 2 parts, Cr metal (574.3 eV) and Cr^{3+}-O (~576 eV).
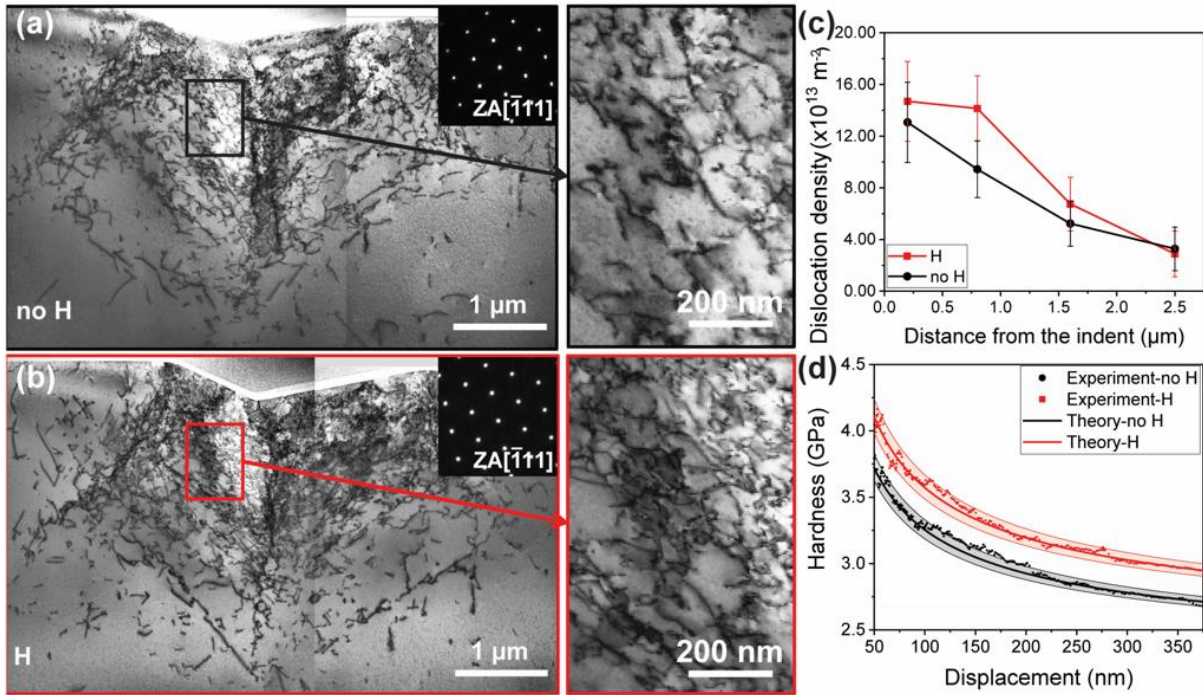
Fig. 4.7 BF-STEM analysis of the dislocation structure underneath nanoindentation imprints in Fe-21Cr imaged in $[\bar{1}11]$ zone axis (ZA): (a) Without hydrogen; (b) Post-mortem after charging with a current density of 2.11 mA/cm^2 at -1.5 V_{Ref} during nanoindentation. (c) Comparison of dislocation density with and without hydrogen. (d) Experimental and theoretical hardness curves with respect to the indentation depth based on Eq. (4.9) and (4.10) for the sample with and without hydrogen, respectively.

Before hydrogen charging, the initial surface of Fe-21Cr consists of a layer of air-formed oxide (~4 nm) after being freshly mechanically polished by OPS (a 40 nm colloidal silica suspension). After hydrogen charging with the backside charging setup for ~6h, the sample was immediately investigated by XPS. The frontside measurements were conducted directly after taking out the specimens, while the measurements for the backside in contact with the electrolyte were conducted after rinsing with deionized water and ethanol, followed by drying with hot air. These data shows that the chemical composition of the indented surface after backside hydrogen charging remains the same as the reference (uncharged) surface, consisting of a native oxide layer of about 4 nm. However, the side that was in contact with the electrolyte

shows an increased oxide layer with a thickness of 8 nm and higher Cr content while Fe is depleted.

A representative condition was chosen for further microstructural analysis as the hydrogen-induced hardening effect is found in all different materials. FIB cross-sections were extracted from the residual nanoindentation imprints and analyzed by BF-STEM*. Fig. 4.7a and b show the dislocation structure after indentation in the hydrogen-free and hydrogen-charged Fe-21Cr samples within (110) orientation, respectively. The hydrogen charged sample was indented while exposed to a current density of 2.11 mA/cm^2 at -1.5 V_{Ref}. A comparison of Fig. 4.7a and b reveals a higher dislocation density for the hydrogen charged sample, as quantitatively displayed in Fig. 4.7c. Details on the calculations of the dislocation density and thickness of the TEM foil are found in Fig. 4.8. The lattice constant a_0 is calculated based on the diffraction pattern with zone axis of [$\bar{1}$11] direction (Fig. 4.8c and d), combing with the formula shown as follows:

$$\frac{1}{d} = \frac{a_0}{\sqrt{h^2+k^2+l^2}}$$ (4.1)

where d is the distance of two diffraction points for a specific orientation. h, k, and l are the miller indices.

Fig. 4.8 displays the procedure of Fiji analysis of dislocations from the bright field STEM images [137]. The plastic zone is divided into 4 regions underneath the indent, taking the region closest to the imprint as an example (Fig. 4.8a and b). The thickness of the foil t_f was calculated according to the log-ratio method [136]:

$$\frac{t_f}{\lambda} = -\ln(\frac{I_0}{I_t})$$ (4.2)

where λ is the inelastic mean free paths for the investigated material, 102 nm was chosen at the incident kinetic energies of 200 kV for α-Fe material [151], I_0 is the integral of zero-loss peak counts, I_t is the integral of total spectrum counts. Fig. 4.8e and f show the lamella thickness distribution with and without hydrogen charging (-1.5 V_{Ref}). In each region, the dislocation density ρ is calculated as follows:

$$\rho = \frac{1}{A \times t}$$ (4.3)

51

---

* The TEM measurements were performed by Subin Lee

where l is the total dislocation line length, and A is the analyzed area.
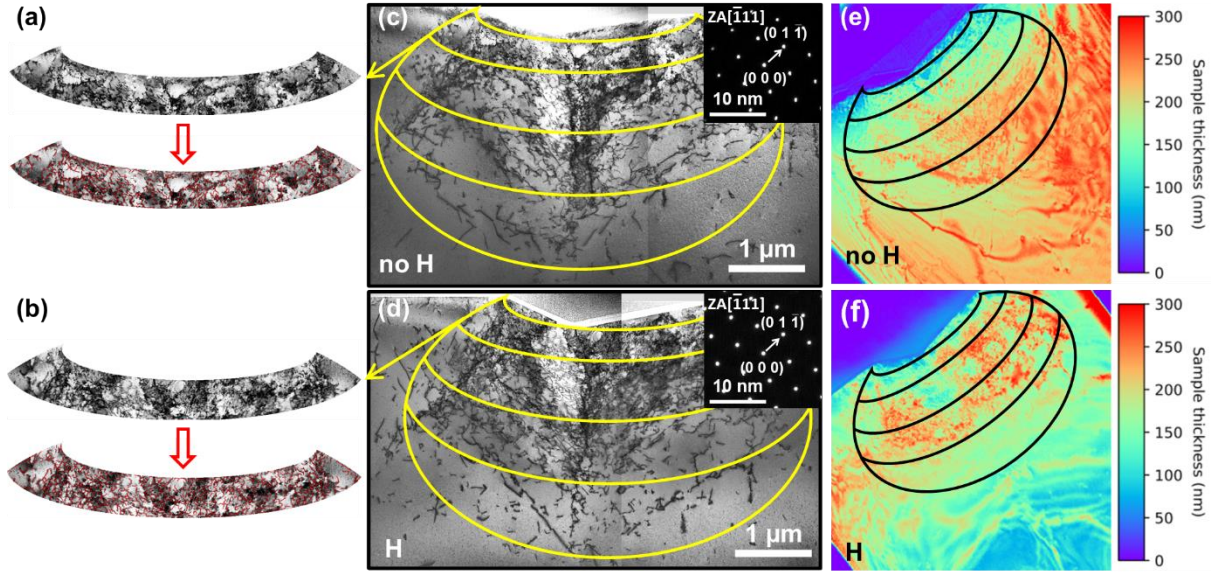
Fig. 4.8 Dislocation and thickness analysis by bright-field STEM images underneath nanoindentation imprints in Fe-21Cr near normal orientation $[\bar{1}11]$: (a), (c) and (e) without hydrogen; (b), (d) and (f) correspond to indents performed during hydrogen charging with a current density of 2.11 mA/cm^2 (-1.5 V_{Ref}).

Throughout the plastic zone, an increase in dislocation density of 24 % is observed in the presence of hydrogen ($\rho_{dis, H}$= 9.6x10^{13} m^{-2}) compared to the hydrogen-free reference ($\rho_{dis, noH}$=7.8x10^{13} m^{-2}). The following formula was used to calculate the dislocation density:

$$\rho_{dis} = \frac{1}{t_f \times A} \tag{4.4}$$

where ρ_{dis} is the dislocation density, l is the total length of dislocations measured by image filtering, A is the evaluated area, t_f is the thickness of TEM foil.

A high density of tangled dislocations was also found in TEM by Wang et al. [29] after cathodically charging pure Fe while conducting a stress relaxation test. In our post-mortem dislocation analysis, we observe that the difference in dislocation density becomes less pronounced with increasing the distance from the indent.

4.3 Discussion

4.3.1 Hardening effect of principal substitutional elements

The higher hardness for the FeCr alloy with 21 at.% Cr compared to 16 at.%Cr can be attributed to substitutional solid solution strengthening (Fig. 4.5b). The larger atomic radius of Cr creates a strain field around Fe atoms interacting with dislocations [152-154]. By characterization upon *in situ* TEM with Fe-14 wt.%Cr (95-300 K), Caillard [155] reported that the screw dislocation mobility is strongly affected by the local pinning of solute at superjogs, causing the solid solution hardening. Matijasevic and Almazouzi [156] report in their studies a linear increase of yield stress with increased Cr content, which fits well to our hardness observation.

4.3.2 Diffusive hydrogen-induced hardening mechanism

We can follow the concept of Wang et al. [145] to further unravel the hardening effect of hydrogen in Fe-21Cr using our nanoindentation data. Based on the Tabor's model, the elastoplastic range of the CSM hardness curve can be interpreted as shown by Durst et al. [157]:

$$H_0 = C\sigma \tag{4.5}$$

Where H_0 is the hardness obtained from indentation tests. C is the Tabor's factor assumed to be 3 in this case, when simplifying the nanoindentation complex stress state to uniaxial stress state [158]. As the indentation was conducted within a single crystal, σ contains the Taylor's stress (σ_{Taylor}) and lattice friction (σ_{Fric}) that play an essential role in bcc materials [159].

$$\sigma = \sigma_{Taylor} + \sigma_{Fric} \tag{4.6}$$

The term σ_{Taylor} represents the mutual interaction between dislocations and can be elucidated as [160]:

$$\sigma_{Taylor} = M\alpha Gb\sqrt{\rho_{dis}} \tag{4.7}$$

where M is the Taylor factor, which is 3.06, averaged for different grains in bcc materials [161-163], α is an empirical constant depending on the dislocation structure, taken as 0.22 for this bcc material, considering the complicated stress state for indentation [157, 164]. The shear stress G used here is 83 GPa, conjectured from α-Fe studies [165].
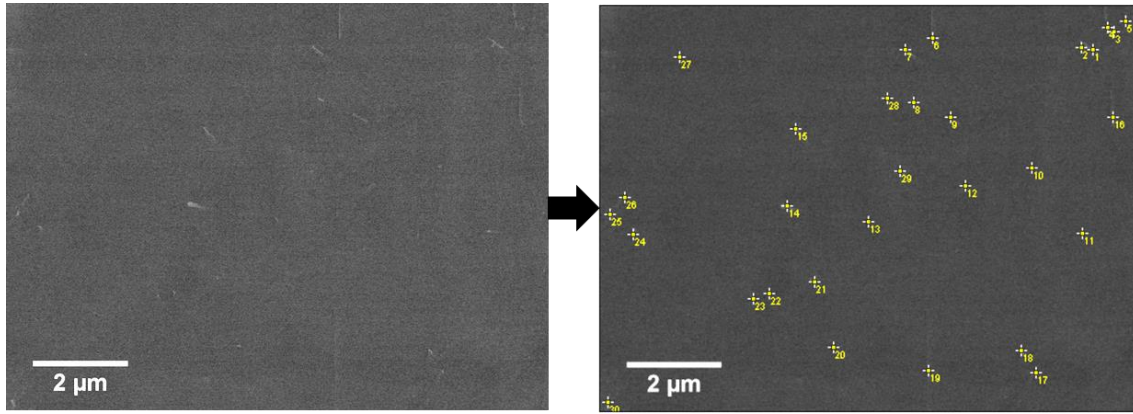
Fig. 4.9 Measurement of dislocation density by ECCI.

The dislocation density ($\rho_{dis} = \rho_{GND} + \rho_{SSD}$) contains both statistically stored dislocations (SSD) and geometrically necessary dislocations (GND). The specimen is long time annealed and without pre-deformation. Therefore, it is reasonable to assume that the ρ_{dis} value of 2.4×10^{12} m^{-2} measured by ECCI (Fig. 4.9) is closely related to the SSD density (ρ_{SSD}) for our material [145]. The GND can be then calculated in this case according to the Nix-Gao model [160]:

$$\rho_{GND} = \frac{3}{2} \frac{\tan^2 \theta}{f^3 bh} \qquad (4.8)$$

where θ is 24.63° for the Berkovich tip [126], f is the ratio between the radius of the plastic zone and the contact area, calculated based on the ECCI images of Fe-21Cr (Fig. 4.10). When the force of the nanoindentation is as large as 10 mN, microstructure features of pronounced slip lines and pileups appear in the vicinity of the indents, which enhances the topographic contrast of the ECCI images drastically [166]. This contrast combines with the orientation and defect contrast, making it complicated to identify the contour of the contact and plastic zone of the imprints with such a high load. A spherical indenter is applied as the plastic zone is more homogeneous for deformation investigations. In addition, the radius ratio f of the plastic zone (a_{PZ}) to the contact zone (a_c) is verified to be indenter geometry independent in single crystal bcc Fe-3 wt.% metal [167]. Therefore, a lower maximum load of 3 mN was applied using a spherical indentation tip to obtain f, which is 2.82 ± 0.12 for indents without hydrogen charging (f_{noH}) as shown in Fig. 4.10a and 2.57 ± 0.12 for the ones done during hydrogen charging (f_H) as shown in Fig. 4.10b. The plastic zone is assumed to be the area with deformation larger than 1-2 %, according to Durst et al. [168]. Therefore, the area with few dislocations is excluded, where the contribution to plasticity is negligible. The shrinkage of the plastic zone is the

verification of hydrogen hindering the motion of dislocations in indents performed during hydrogen charging. The decreased *f* value that indicates a contraction of the plastic zone by the introduction of hydrogen was also observed by Wang et al. [145], implying that hydrogen dragged the dislocation motion.
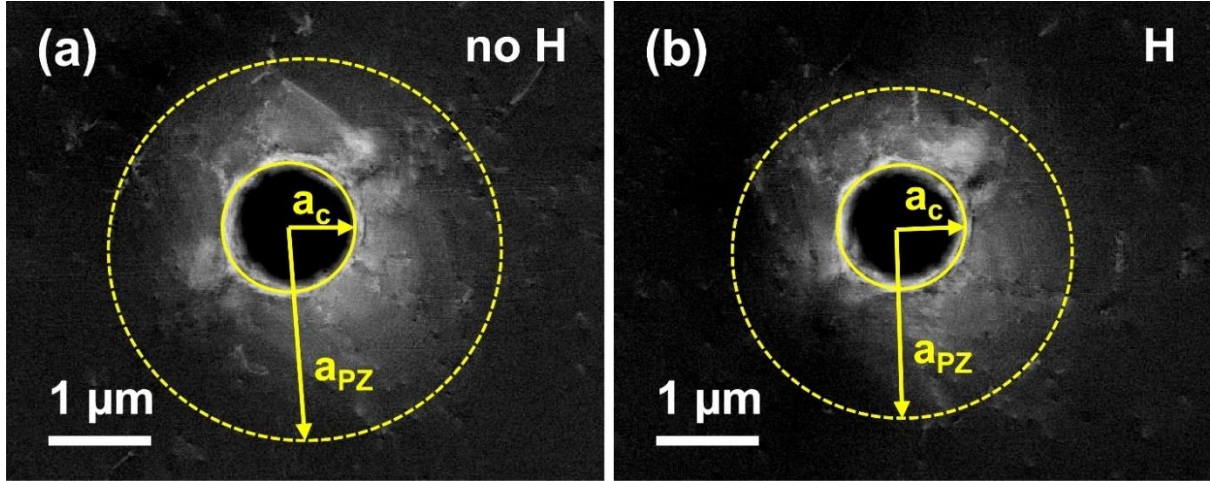
Fig. 4.10 Radius of contact area (a_c) and plastic zone (a_{PZ}) for the indents with a maximum load of 3mN by spherical indenter tip in Fe-21Cr near (110) normal orientation: (a) indented without hydrogen (b) indented during charging with a potential of -1.65 V_{Ref}.

The Burger's vector $b = 1/2[111]$ for the bcc lattice is calculated as 0.222 nm, considering a lattice constant $a_0 = 0.256$ nm (Details shown in the Supplement Material Fig. 4.8c and d). By combing Eq. (4.5)-(4.8), the hardness in the absence of hydrogen can be described as follows:

$$H_0 = C(\sigma_{\text{Taylor}} + \sigma_{\text{Fric}}) = C(M\alpha Gb \sqrt{\rho_{\text{SSD}} + \frac{3}{2} \frac{\tan^2\theta}{f^3 bh}} + \sigma_{\text{Fric}}) \qquad (4.9)$$

The measured and theoretical fitted curves without hydrogen are shown in Fig. 4.7d. The lattice friction stress is deduced as 710 MPa from Eq. (4.9), and it is close to the 678 MPa value obtained in a Fe-12 wt.%Cr alloy by considering the solid solution strengthening [156]. The difference might arise from the evaluation of the plastic zone in the ECCI image and differences in the composition. However, this does not affect the relative calculated stress contribution by hydrogen. In the current experiments, it is feasible to assume that hydrogen influences only the ρ_{GND} and σ_{Fric} as no other features were introduced affecting the ρ_{SSD} by the backside hydrogen charging method. Therefore, the Eq. (4.9) can be rewritten for the hydrogen charged sample as:

$$H_0 = C(\sigma_{Taylor} + \sigma_{Fric}) = C(M\alpha Gb\sqrt{\rho_{SSD} + \frac{3}{2}\frac{\tan^2\theta}{f_H{}^3 bh}} + \sigma_{Fric} + \sigma_H) \qquad (4.10)$$

where σ_H is the contribution of hydrogen to the overall stress. Using this equation, σ_H was calculated as 50 MPa, close to 45 MPa as calculated for Fe-22Mn by ECNI method [145]. The stress increment is attributed to the interaction of hydrogen with dislocations. Due to the high hydrogen diffusivity in bcc alloys [26] and the deep trapping site for hydrogen that constitutes the dislocation core [169, 170], it is expected that the local accumulation of hydrogen in the high-stress region beneath the indenter is sufficient to form a Cottrell atmosphere, which can drag the moving dislocations rather than accelerate the dislocation motion. This pinning/dragging impedes the movement or cross-slip of dislocations, leading to strain hardening [171, 172], which is consistent with the solute drag theory and supported by atomistic simulations in α-Fe [88, 173]. Particularly in bcc alloys, the formation and movement of kink pairs at screw dislocations are critical in determining the plastic behavior at a temperature below 340 K [174]. When kink motion is the rate-controlling step, the increase of lattice friction might be ascribed to the interaction of Carbon (C)-hydrogen (H) complexes with the kinks that retard their sideward motion along screw dislocations, as brought up by Oguri et al. [175]. Nonetheless, if carbon is not considered, the hydrogen solute atoms alone might segregate to the kinks and inhibit their motion according to simulations [62]. Besides, hydrogen facilitates vacancy generation, which retards the dislocation motion as well. Most *ex situ* experiments cannot eliminate the effect from trapped hydrogen. In our case, the reference data was taken after the pre-charging procedure filling the deep traps. Therefore, the observed hardening effect is mainly due to the diffusive hydrogen and hydrogen trapped by flat trapping sites such as dislocations and Cr-caused lattice distortion [26].

The increase in dislocation density with hydrogen, as observed in Fig. 4.7c, can also be calculated using Eq. (4.8). As the ρ_{SSD} is one order of magnitude smaller than ρ_{dis}, thus ρ_{GND} approximately equals to ρ_{dis}. The ratio of the dislocation density for the uncharged ($\rho_{dis,\,noH}$) and charged ($\rho_{dis,\,H}$) sample can be estimated by the following equation:

$$\frac{\rho_{dis,\,noH}}{\rho_{dis,\,H}} \approx \frac{\rho_{GND,\,noH}}{\rho_{GND,\,H}} = \frac{f_H{}^3}{f_{noH}{}^3} \qquad (4.11)$$

where $\rho_{GND,\,noH}$ and $\rho_{GND,\,H}$ are the density of GND for the uncharged and charged sample,

respectively. The calculated ratio of $f_H{}^3/f_{noH}{}^3$ is 1.32 ± 0.34 and coincides well with the ratio of dislocation density that is 1.24 calculated from Fig. 4.7c. A tremendous amount of dislocation entangled in the vicinity of the imprint, which might lead to the deviation of the value, especially for the hydrogen charged lamella with a higher amount of dislocations.

The increase in dislocation density with hydrogen can be attributed to reducing the free energy for the dislocation line energy according to the "defactant theory" developed by Kirchheim [62]. The "defactant theory" is based on a thermodynamic model [62] and the experimentally observed pop-in reduction phenomenon [118, 145, 146]. In the same alloy of Fe-21Cr, the reduction of pop-in load is also shown in by Duarte et al. [61]. The generation and multiplication of dislocations are facilitated in the presence of hydrogen. Consequently, a higher density evolves, leading to dislocation entanglement and material strengthening [88]. Besides, multiscale simulations in Ni suggest nano-hydrides formation around the dislocation lines, which can impede dislocation motion [5] – a scenario that is so far experimentally not confirmed. In summary, our results support the interpretation that hydrogen initially facilitates dislocation nucleation following the "defactant theory"; afterwards, Cottrell clouds form and increase the resistance force for dislocation motion according to the solute drag theory [88]. The synergy of both effects results in a drastic enhancement of the hardness observed in the present study, while the modulus remains unaffected.

4.3.3 Hydrogen-induced hardening effect with the increasing content of principal substitutional elements

Fig. 4.11 shows the diffusible hydrogen-induced hardening normalized by the hydrogen-free (pre-charged) measurement in Fe-4Al, Fe-16Cr and Fe-21Cr samples with (100) grain orientation. The data corresponds to ~3 mA/cm^2 based on Fig. 4.5b, above the turning point in the hardness behavior. The difference of electronegativity of Cr (0.54) or Al (0.59) to hydrogen is higher than that of Fe to hydrogen (0.37) according to the Pauling scale, which indicates a higher chemical affinity of Cr (or Al) to hydrogen [176]. The increased hydrogen-induced hardening effect can be discerned with the increasing content of Cr and Al in the ferritic alloys. A targeted study is necessary to study the individual effect of each principal substitutional element and therefore we will focus here on the comparison of the Cr containing alloys. Nevertheless, it is crucial to notice that the content of principal substitutional elements plays a critical role in this hardness differentiation in Fig. 6, as the influence of the initial dislocation density and alloy interfaces can be excluded since the experiments were conducted in single grains with low dislocation density as measured by ECCI.
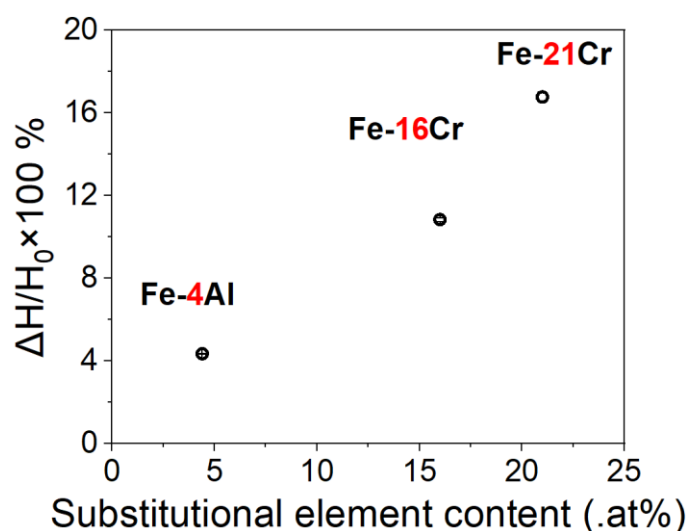
Fig. 4.11 Relative variation fraction of hardness normalized by the reference H_0 of the hydrogen-free Fe-4Al, Fe-16Cr and Fe-21Cr samples as a function of the principal substitutional element content at 3 mA/cm^2 based on Fig. 4.5b.

In the Fe-Cr alloys, a more pronounced hydrogen-induced hardening effect can be observed with higher Cr content. Substitutional Cr atoms cause lattice distortions creating a dilational misfit and therefore more space for hydrogen. According to ab-initio simulation works in α-Fe and Fe-9 wt.% Cr by Viviana et al. [177], substitutional Cr atoms could transverse the stable state of tetrahedral sites in pure Fe to a non-symmetrical state and create a new octahedral site that is more stable for hydrogen to sit in. This formation of a new octahedral site leads in Fe-9 wt.% Cr to a 200-time reduction in diffusion and a 10-time reduction in permeation coefficient. This also suggests an increase in hydrogen solubility [177]. Besides, hot extraction chemical analyses show that the hydrogen content in Fe-10.4 wt.% Cr is higher than in pure Fe after being immersed in 1 M H$_2$SO4 at 25 °C for 25 h [26].

Furthermore, a hydrogen trap with less than 30 kJ/mol binding energy is generally considered a reversible flat trapping site [26, 27]. The dilated sites near dislocations, large atoms of alloying elements and the stress field around precipitates are usually in this category of flat traps. In contrast, dislocation cores, grain boundaries, and interfaces with more than 50 kJ/mol binding energy are treated as deep traps [26]. The binding energy of hydrogen to Cr obtained by simulations in ferritic steels is 26-27 kJ/mol, which corresponds to flat hydrogen trapping sites [26, 170, 178]. Fe-Cr alloys would then absorb more hydrogen with a higher Cr content, leading to an increase in hardness. This was also observed in α-Fe compared to 13Cr and 16Cr binary alloys [18].

4.3.4 Anisotropy in hydrogen-induced hardening effect

Fig. 4.5c displays the anisotropy on the hydrogen-induced hardening effect for different grain orientations of (100), (110) and (111) for Fe-21Cr. When the applied current density is below the turning point of 2-3 mA/cm^2, the initial slope of the (100) grain has the highest value than (110) and (111) grains. This observation coincides well with the density functional theory (DFT) simulations performed in bulk bcc iron that shows hydrogen occupies the deep subsurface tetrahedral sites in (110) instead of the shallow subsurface tetrahedral sites in (100) during the diffusion process [179]. Therefore, a much lower barrier is predicted to exist in (100) than in (110) for hydrogen hopping through the adjacent tetrahedral sites following a curved path. On the contrary, the tendency of the slope for these 3 orientations is opposite above the transient current density region of 2-3 mA/cm^2 ($k(2)_{100} < k(2)_{110} < k(2)_{111}$), which might indicate a faster equilibrium in the (100) orientation. It needs to be noted that the applied current density in this study is limited (< 5 mA/cm^2). The anisotropic hardening effect between different grain orientations might not exist with higher applied current density, which requires further research.

4.3.5 Hydrogen concentration profile

The hydrogen diffusion behavior during hydrogen charging of the studied alloys can be described by the Fick's laws since the influence of deep traps can be excluded. The Fick's 1st law that applies to a steady state system where the concentration keeps constant is:

$$J = -D \frac{dC(x)}{dx} \tag{4.12}$$

where J represents the diffusion flux (amount of hydrogen passing through per unit area per unit time), D is the diffusion coefficient, and $C(x)$ is the concentration of hydrogen in the specific analyzed position x. However, the hydrogen concentration within the system is changed with time as hydrogen was produced continuously from the backside of the specimen. The one dimensional Fick's 2nd law here is applied to describe this condition:

$$\frac{\partial C(x,t)}{\partial t} = -\frac{\partial J}{\partial x} = D \frac{\partial^2 C(x,t)}{\partial x^2} \tag{4.13}$$

The frontside of the sample is purged with continuous Argon gas and the hydrogen concentration can be considered 0 all the time ($C_2 = 0$). For simplicity, the hydrogen concentration at the backside of the sample is considered to be a constant value of C_0 for a

given applied current density. The initial bulk hydrogen content is set to 0 (*f(x')=0*) since the hydrogen concentration is treated as 0 all over the sample before hydrogen charging. Therefore, the initial boundary conditions are given in the following formulas:

$$C_1=C_0, \ x=0, \ t\geq0 \tag{4.14}$$

$$C_2=0, \ x=L, \ t\geq0 \tag{4.15}$$

$$f(x')=0, \ 0<x<L, \ t=0 \tag{4.16}$$

where *L* is the thickness of the specimen, which is 2.4 mm. This condition inherently assumes a more rapid surface kinetic process than bulk diffusion. The trigonometrical solution for the Fick's equation, with this specific non-steady state with both surface hydrogen concentrations to be constant, is solved as follows [72]:

$$C(x,t)=C_1+(C_2-C_1)\frac{x}{L}+\frac{2}{\pi}\sum_{1}^{\infty}\frac{C_2\cos n\pi-C_1}{n}\sin\frac{n\pi x}{L}\exp\left(-\frac{Dn^2\pi^2t}{L^2}\right) \tag{4.17}$$

$$+\frac{2}{L}\sum_{1}^{\infty}\sin\frac{n\pi x}{L}\exp\left(-\frac{Dn^2\pi^2t}{L^2}\right)\int_{0}^{L}f(x')\sin\frac{n\pi x'}{L}dx'$$

In combination with Eq. (4.14)-(4.16), the equation can be rewritten as:

$$\frac{C(x,t)}{C_0}=1-\frac{x}{L}-\frac{2}{\pi}\sum_{1}^{\infty}\frac{1}{n}\sin\frac{n\pi x}{L}\exp\left(-\frac{Dn^2\pi^2t}{L^2}\right) \tag{4.18}$$

Differentiating Eq. (4.18) based on Eq. (4.13), the classic hydrogen flux permeation curve through the sample can be obtained as follows [180]:

$$\frac{J(x)}{J_\infty}=1+2\sum_{1}^{\infty}\cos\frac{n\pi x}{L}\exp\left(-\frac{Dn^2\pi^2t}{L^2}\right) \tag{4.19}$$

According to the aforementioned models, the hydrogen concentration distribution curves as a function of time across the specimen are schematically displayed in Fig. 4.12a. The model is applied to the Fe-21Cr alloy as an example (Fig. 4.3c). For Fe-21Cr, based on the Kelvin probe-based permeation experiments, the diffusion coefficient here in Fig. 4.12a and b we applied is 1.5×10^{-10} m^2/s [61]. In Fig. 4.12b, the permeated hydrogen flux on the frontside of the specimen is simulated by Eq. (4.19). When charging hydrogen continuously from the backside, hydrogen

gradually permeates through the specimen. After a certain duration, the hydrogen flux reaches the steady state that a continuous constant hydrogen flux $J(\infty)$ permeates through the sample. Infinite duration is required to reach the steady state. Therefore, we collect the hardness value above 95 % of the $J(\infty)$ (14353 s) as the variation afterward is negligible. The tendency of the hydrogen flux shows a sigmoidal shape, which coincides well with the hardness evolution at the first stage upon charging of the hydrogen, as exhibited in Fig. 4.3c, indicating that the hardness variation is attributed to the variation of hydrogen flux in the frontside of the specimen.
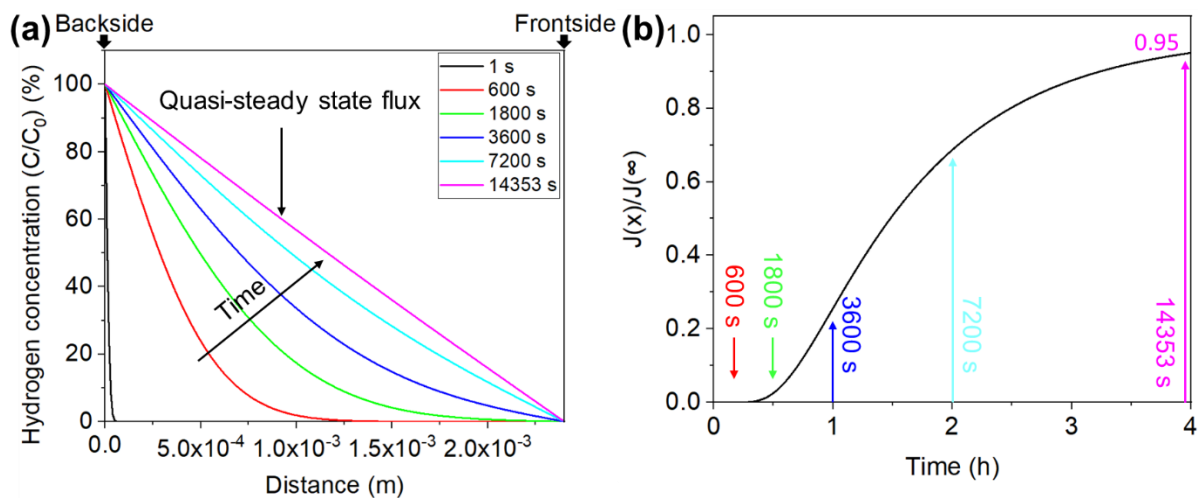
Fig. 4.12 (a) Modelling of the distribution curves of hydrogen concentration along the specimen depth for different hydrogen charging times in Fe-21Cr (Fig. 4.3c). Charging starts at the backside and continues until the system reaches a quasi-steady state (95 % of the steady state of hydrogen reaching the frontside). (b) Simulated evolution curve of hydrogen permeation flux for different backside charging times.

4.3.6 Invariance of Young's modulus with the introduction of hydrogen

A negligible change in the elastic modulus can be found in all the tested alloys during hydrogen charging (Fig. 4.5a). In fcc Ni [181] and hcp Ti-Mo alloy [182], which can accumulate a more massive amount of hydrogen, a reduction of the elastic modulus was observed, caused by a hydrogen-related lattice expansion. Besides, the elastic modulus reduction might be attributed in some cases to the artificial influence on the test setup or pile-up formation as found experimentally [118]. In our case, PCTFE avoids the electrolyte absorption into the charging cell, which guarantees the stability of the setup. In addition, Fischer et al. [183] presented a minor Young's modulus variation in single-crystal bcc Ta where ~61 wt ppm of hydrogen

reduces 0.08 % of $\Delta E/E$ at ambient temperature. Nonetheless, the hydrogen solubility in bcc is extremely low, with only 0.085 wt ppm diffusible hydrogen contained in Armco iron at ambient temperature [184]. Therefore, the concentration of hydrogen is far from reaching the amount necessary to influence the elastic modulus as claimed by Zhang et al. [185] that hydrogen content of ~8 wt ppm does not change Young's modulus in α-Fe at room temperature.

4.4 Summary and Conclusions

We have performed novel *in situ* backside hydrogen loading frontside nanoindentation tests on ferritic Fe-4Al, Fe-16Cr and Fe-21Cr alloys to investigate their mechanical response to electrochemically charged hydrogen. The results are summarized below:

- Time-dependent nanoindentation measurement as a function of the applied stepwise increased current density/potential to study HE is reliable with a backside charging approach and allow distinguishing between the effects of deeply trapped hydrogen and mobile hydrogen.

- The specific dynamic tendency in the mechanical behavior is shown for the initial transient charging stage and the hydrogen release. Once the charging process starts, the increase in hardness follows the sigmoidal curve corresponding to the diffusion behavior of hydrogen. The hydrogen release stage, after the charging is stopped, requires more than double the time than charging as it includes the release of hydrogen from deeper traps.

- A hardening effect appears in Fe-4Al, Fe-16Cr and Fe-21Cr alloys during hydrogen charging. At higher current density, the hardness variation concerning the reference hardness follows an initial linear increase. There exists a turning point for the increasing tendency with applied current density between the range of 2-3 mA/cm^2, above which the slope of the absolute hardness experiences a drastic decrease, indicating an establishment of a quasi-equilibrium state for introduced and releasing hydrogen flux.

- A more pronounced hardening effect is observed with a higher concentration of substitutional elements: 16.7 % enhancement in Fe-21Cr, 10.8 % in Fe-16Cr, and 4.3 % in Fe-4Al with a specific current density above the transient region of 2-3 mA/cm^2.

- Anisotropic hardness variation during hydrogen charging within different grain orientations of (100), (110), and (111) is noticed in Fe-21Cr alloy.

- A 24 % increase of dislocation density is observed by STEM for nanoindents in hydrogen charged Fe-21Cr compared to the uncharged reference.

- The hardening effect is associated with an increased dislocation density beneath the indenter due to hydrogen, and the hydrogen increased stress of ~ 50 MPa.

- The Young's modulus remains constant as the hydrogen solubility in all three bcc alloys is extremely low.

The measurements reveal that diffusible hydrogen impacts dislocation plasticity most. In contrast, trapped hydrogen does not manifest itself in a pronounced hardness change considering that deep traps did not release all hydrogen at ambient temperature in the air even after a long time in our studies. It can be speculated that adding more deep traps to materials only helps when exposed to a certain amount of hydrogen, as the diffusible hydrogen controls the enhanced hydrogen plasticity. As higher Cr content results in a higher hydrogen hardening effect, it is feasible to speculate that reducing the amount of Cr in alloys will mitigate the effect from hydrogen. Higher dislocation density plays a more profound role in the hydrogen hardening effect in comparison to the solute drag stress, meaning the increase of initial dislocation density due to the decrease of the free energy of homogeneous dislocation nucleation is assumed to play a more critical role in HE.

5. The effect of microstructural features on the hydrogen diffusion coefficient in ferritic FeCr alloys: a comparison between the Kelvin probe based potentiometric hydrogen electrode method and a nanohardness based method

5.1 Introduction

Hydrogen prefers to accumulate around the stress-concentrated regions and has a high diffusivity of 10^{-5} to 10^{-4} cm^2/s in ferritic iron alloys, even at ambient temperature [26, 30]. Due to its small atomic radius, hydrogen can easily be absorbed and penetrate through the material. Consequently, even with a low hydrogen solubility of less than 3 at. ppm for pure iron at room temperature, α-Fe is susceptible to HE [78]. Therefore, understanding the diffusion behavior of hydrogen and the interaction with different microstructural features in ferritic alloys are critical in unraveling the underlying mechanism that leads to HE and further producing HE resistant metals in preventing this sudden early failure.

Usually, when introduced into the metal, interstitial hydrogen atoms with the surrounding stress field can either be transported or attracted to available sinks in metallic materials. Defects forming the internal stress field, such as vacancies, dislocations, grain boundaries, inclusions interacting mutually with hydrogen-generated stress fields etc. or other microstructural features that introduces localized strain in the lattice, are acting as different types of hydrogen traps. The hydrogen permeation is decelerated for a sample with those imperfections compared to the defect-free ideal crystalline [186]. Different hydrogen trapping sites correspond with different hydrogen activation energies required for releasing hydrogen from the specific traps (E_a). In principle, the hydrogen trapping sites have been classified into two categories: flat trapping site (also called reversible hydrogen) and deep trapping site (known as irreversible hydrogen). Diffusive hydrogen jumps between the interstitial lattice site for which only ~4-8 kJ/mol is

needed in the case of pure iron [24]. The reversible trapping site generally owns an activation energy of less than 50 kJ/mol, differing it from the irreversible trapping site that requires an activation energy larger than 50 kJ/mol at ambient temperature, which impedes the hydrogen motion [24-28]. The reversible trapping site and the diffusive hydrogen play a more critical role in HE at ambient temperature as the deeply trapped hydrogen tends to lack diffusivity and contribute less to the hydrogen introduced failure process [187]. Upon specific service temperature, flat trapped hydrogen can detach from the reversible trap site that has lower activation energy after a certain duration, while external thermal energy would be required for deeply trapped hydrogen [73].

As a principle substitutional element, Cr has been added to steels to enhance the resistivity to corrosion and neutron irradiation expansion in industrial applications, which are exposed to a harsh environment under the risk of HE [188]. The substitutional Cr atom in ferritic steels is generally treated as the cause for the appearance of reversible hydrogen trapping sites. As calculated by simulations, the binding energy is -26-27 kJ/mol for Cr atoms with hydrogen in ferritic iron [170]. In terms of hydrogen diffusion behavior, Cr affects hydrogen diffusion in accordance with the chemical and elastic interaction between the Cr atom and hydrogen. Regarding the chemical interaction, Cr has a higher chemical (electronically) affinity to hydrogen based on Pauling scale [176]. While considering the elastic interaction, the Cr atom has a larger atomic radius than Fe, generating a distortion around the Cr atoms within the Fe matrix. A reduction of diffusion coefficient with higher Cr content due to the retardance of strain field around Cr atoms was commonly observed by the permeation tests. Hagi [189] found this effect in Fe-0.4~5.1 at.%Cr by the electrochemical permeation technique. The interstitial sites created around the substitutional atoms are suggested to act as hydrogen trapping sites, attributing to the strain field alteration after investigating the lattice constant by the X-ray diffraction technique [189]. The same reduction in hydrogen diffusion coefficient and enhancement in hydrogen solubility with increased Cr content in FeCr binary alloys was monitored at ambient temperature by the electrochemical double cell and hot extraction chemical analysis, respectively [26]. Even at a higher temperature range of 473-573K, the reduction in diffusion coefficient among Fe-4~14 wt.%Cr has also been reported using the gas evolution permeation technique [190]. Furthermore, as proposed by Ramunni based on the ab-initio simulation, the mismatch originating from Cr atoms produces a more stable octahedral interstitial site for hydrogen that reduces the diffusion coefficient by two orders of magnitude and enhances the hydrogen solubility in Fe-9 wt.%Cr compared to annealed α-Fe [177]. On the

other hand, Cr carbides are generally treated as the irreversible hydrogen trapping sites in ferritic steels [170, 191].

Different analytical methods have been used to characterize the trapping of hydrogen at different microstructural features, such as small-angle neutron scattering [192], transmission electron microscopy [103] and atom probe tomography [43]. Although these methods detect hydrogen/deuterium with microscale resolution at a specific location, there is a lack of quantitative information on diffusive hydrogen at a macroscopic level, which prevents the applicability of microstructural engineering from effectively mitigating HE effects. TDS, also known as TPD, is critical in investigating the thermodynamic and kinetic behavior of desorption/decomposition procedures in bulk materials. The amount of hydrogen desorbed from various hydrogen trapping sites at a defined heating ramp can be quantitatively identified by this technique as it is microstructural constituent sensitive [81].

However, the loss of diffusible hydrogen prior to the measurement is inevitable and the hydrogen diffusion rate throughout the specimen is unable to be determined. As compensation for the thermal destructive TDS measurements, the permeation technique is commonly applied since the hydrogen is continuously generated and penetrates through the specimens. The Devanathan-Stachurski double cell based on the principle theory of Fick's law is widely adapted in conventional hydrogen permeation studies, enabling a quantitative study of the hydrogen diffusion coefficient by measuring hydrogen oxidation current at the exit side electrochemical cell [107]. Nonetheless, the palladium layer deposited on the sample surface needs to be immersed in the solution, which leads to the instability of these few hundred-nanometer layers with harsh polarization conditions. Therefore, in this study, a non-destructive KP-based potentiometric technique was applied, enabling the measurement of the localized potentials with high hydrogen detection resolution and sensitivity instead of the averaged permeation rate in DS double cell [104, 105, 108-110].

The investigation of hydrogen introduced degradation of mechanical properties of materials is vital in studying the HE mechanism. The *in situ* hydrogen charging techniques are ideal for exploring the response of ferritic materials to hydrogen due to their high hydrogen diffusivity [60, 143]. Special interests have been triggered in the *in situ* frontside hydrogen charging and nanoindentation method brought up by Barnoush and Vehoff [60], which can introduce localized deformation into the material with a lateral resolution of nanometer-scale while electrochemically charging the specimens with hydrogen simultaneously. However, the

electrolyte-induced surface microstructure and stress condition alteration are unavoidable [118, 119], stimulating the further development of a novel backside hydrogen charging method [61, 143]. As the chemistry and surface topography remains unchanged on the measuring side of the specimen during hydrogen charging on the other side, the application field for this backside hydrogen charging method has been expanded, enabling us to perform mechanical and permeation investigation of bulk bcc FeCr alloys at the same time.

In this work, to study the contribution of various hydrogen traps (i.e. dislocations, grain boundaries, Cr content etc.) to the permeation behavior of hydrogen in the model ferritic FeCr alloys, designated metallurgical treatments have been employed to modify the microstructure. The microstructure analysis was achieved by EBSD and ECCI. An *in situ* KP-based potentiometric hydrogen electrode technique has been applied to measure the apparent and the mixed diffusion coefficient of materials to distinguish the effects from different atomic-scale hydrogen trapping sites. The feasibility of applying nanohardness based methods has been verified by comparing the mixed diffusion coefficient, including the influence of the highly mobile hydrogen that has a more detrimental effect on materials under stress (i.e. both diffusive and reversibly trapped hydrogen), with that calculated by the KP-based permeation method. The nanohardness data is collected by conducting the mechanical measurements with an *in situ* backside hydrogen charging setup. The hydrogen amount has been quantitatively measured using TDS.

5.2 Results

5.2.1 Characterization of microstructure

Grain size and the dislocation density for investigated ferritic alloys with different chemical compositions and metallurgical treatments are listed in Table 5.2. Based on the EBSD measurement, the grain size was calculated with the help of TSL OIM software (Fig. 5.1). The straight vertical lines in between segments of the EBSD image are coming from the stage movement during the combo scanning technique employed to obtain scans of a few millimeters. The bright dislocation lines for alloys with different states (before and after cold rolling, HPT treated combined with annealing) were observed upon the two-beam condition with the applied ECCI technique, as shown in Fig. 5.2 [166]. The dislocation density was calculated by dividing the number of dislocations by the inspection area. After cold rolling, the

dislocation density was enhanced drastically (Fig. 5.2c) compared with the material before cold rolling (Fig. 5.2a). An intermediate dislocation density was noticed in the material after HPT treatment, followed by annealing as displayed in Fig. 5.2b. The calculated grain sizes and dislocation densities for different alloys are shown in Table 3.2.
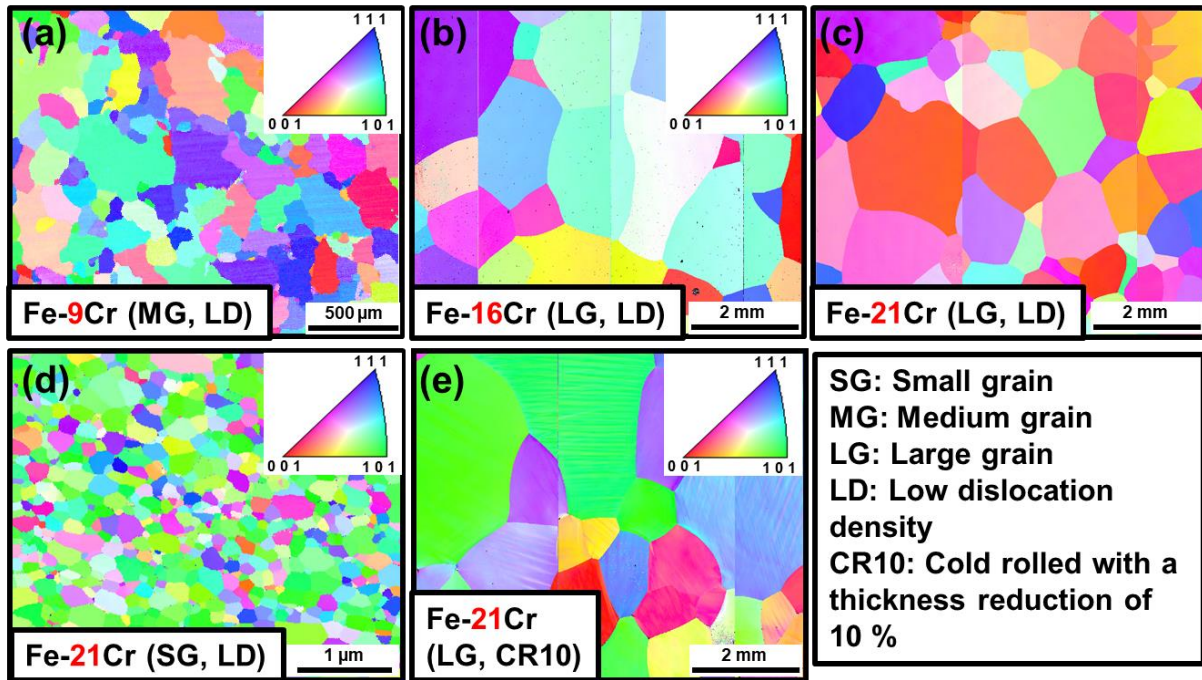
Fig. 5.1 EBSD images of various materials: (a) Fe-9Cr (MG, LD); (b) Fe-16Cr (LG, LD); (c) Fe-21Cr (LG, LD); (d) Fe-21Cr (SG, LD); (e) Fe-21Cr (LG, CR10). The symbols represent the grain size and dislocation density of the alloys (i.e. SG: Small grain, MG: Medium grain, LG: Large grain, LD: Low dislocation density, CR10: Cold rolled with a thickness reduction of 10 %)
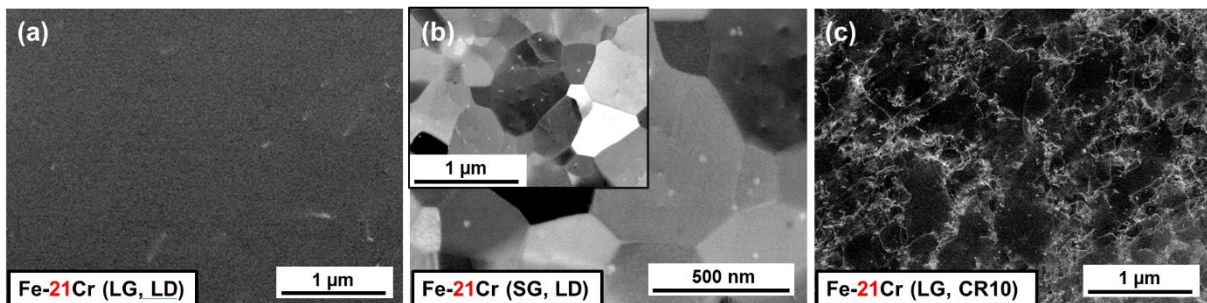
Fig. 5.2 Dislocation density measurement by ECCI in materials: (a) Fe-21Cr (LG, LD); (b) Fe-21Cr (SG, LD); (c) Fe-21Cr (LG, CR10). (SG: Small grain size, LG: Large grain size, LD: Low dislocation density, CR10: Cold rolled with a thickness reduction of 10 %)

5.2.2 Hydrogen concentration in different materials investigated by TDS*

TDS investigation was conducted to compare the quantitatively measured hydrogen amount in different types of materials (as annealed, cold-rolled specimens and HPT treated samples), as exhibited in Fig. 5.3. Fig. 5.3a shows the hydrogen desorption rate curves, the peaks of which indicate different types of hydrogen traps. There exist two peak regions of 50-250 °C and 350-450 °C. The peak of 50-250 °C variates more than the peak in the region of 350-450 °C. Since the TDS experiment onsets within 20 min at ambient temperature, some residual diffusive hydrogen remains in the materials, so the hydrogen desorption rate curves do not start at zero.
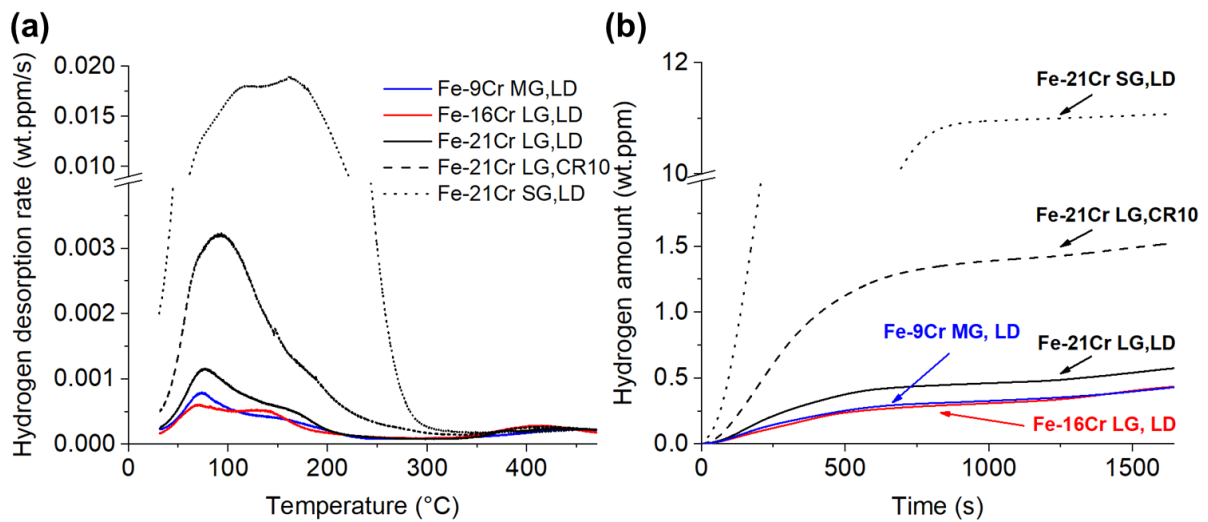
Fig. 5.3 (a) Hydrogen desorption curves and (b) Hydrogen amount curves for Fe-9Cr (MG, LD), Fe-16Cr (LG, LD), Fe-21Cr (LG, LD), Fe-21Cr (SG, LD) and Fe-21Cr (LG, CR10) after hydrogen charging for 4 h at ~2 mA/cm^2. TDS was conducted with a heating rate of 16 °C/min.

The hydrogen amount was determined by calculating the cumulative desorbed hydrogen from the TDS time spectra. By integrating the areas under the peaks, the absorbed hydrogen content in different materials can be obtained as displayed in Fig. 5.3b. The calculated total amount of absorbed hydrogen is listed in Table 5.1. We can see that Fe-21Cr alloys with their higher Cr content contain a relatively higher amount of hydrogen (8.45 at.ppm) compared to Fe-16Cr (6.42 at.ppm) and Fe-9Cr (6.32 at.ppm). This coincides well with the literature [26] that more hydrogen is absorbed in Fe-10.4 wt.%Cr than pure iron after the same hydrogen charging procedure as investigated by hot extraction chemical analysis. When the dislocation density increased from as-annealed of 2.4×10^{12} m^{-2} to cold-rolled of 1.4×10^{14} m^{-2}, a ~2.6 times enhancement of absorbed hydrogen in Fe-21Cr is observed as dislocations are suggested to be the hydrogen reversible trapping sites with TDS analysis [81]. Regarding the grain size,

_____

decreasing from a bigger grain size of 1133 ±85 µm to a smaller grain size of 297 ± 138 nm causes an increase of absorbed hydrogen content from 31.63 at.ppm to 609.51 at.ppm, indicating the critical role of grain boundaries in storing hydrogen.

Table 5.1 Summary of the total absorbed hydrogen amount in different samples. The values are obtained by integrating TDS desorption curves. TDS measurements were performed with a heating rate of 16 °C/min till 470 °C. (The CR10 denote alloys that were cold rolled from Fe-21Cr (LG, LD), with a thickness reduction of 10 %)

Sample / Desorbed hydrogen	Fe-9Cr MG, LD	Fe-16Cr LG, LD	Fe-21Cr LG, LD	Fe-21Cr LG, CR10	Fe-21Cr SG, LD
Weight percentage (wt.ppm)	0.431	0.436	0.575	1.525	11.082
Atomic percentage (at. ppm)	23.71	23.98	31.63	83.88	609.51

5.2.3 Analysis of hydrogen permeation curves (Apparent diffusion coefficient)*

In our case, the KP evaluates the surface chemical potential variation of hydrogen electrodes generated in the coated Pd layer without the influence of oxygen. Fig. 5.4a displays the typical evolution of KP measured potential in the Pd coated side starting from the onset of the hydrogen charging in Fe-21Cr (LG, CR10) until the Pd reaches the binary phase state. The binary phase /reference potential (E_{bp}), which represents the state when dissolved α-Pd-H coexists with the β-H-Pd, is set to 0 V for calibration [109].

With the enhancement of hydrogen content in Pd, the Kelvin probe measured potential drops drastically until reaching the lowest point, which stays static once the hydrogen content in Pd exceeds ~2.4 at.%. The monitored KP potential (E) can be converted to hydrogen concentration in Pd ($c(H_{Pd})$) based on the Nernst equation [105]:

$$E = E_{SHE}^{*'} + m \cdot \ln (c(H_{Pd}))$$
(5.1)

where $E_{SHE}^{*'}$ represents the standard hydrogen electrode potential, the applied m as measured by Evers et al. [104, 109] is -130 mV/decade for this specific nanocrystalline Pd coating with a thickness of 100 nm (deviation should be noted for Pd layer with different microstructure

70

features).
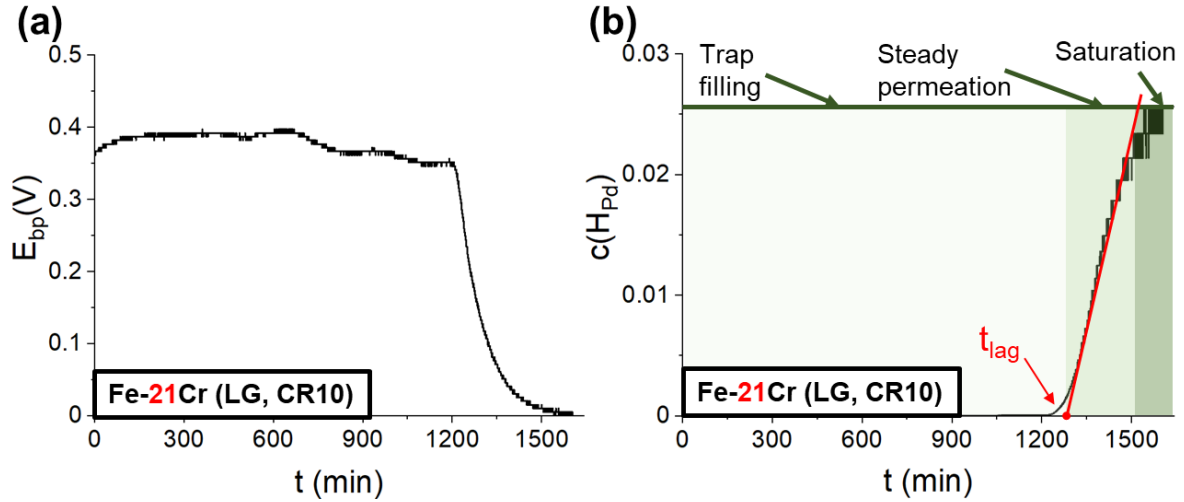
Fig. 5.4 (a) The evolution of Kelvin probe potential measured on the 100 nm Pd coated side during hydrogen charging in Fe-21Cr (LG, CR10) with a polarization voltage of -1.52 V_{Ref}. (b) Permeation curve transferred based on the Nernst equation for calculation of apparent hydrogen diffusion coefficient (Eq. (5.1)).

Fig. 5.4b exhibits the typical permeation curve that shows the corresponding evolution of hydrogen concentration in Pd calculated from Fig. 5.4a. The curve follows the 3 stages of initial trap filling, steady hydrogen permeation and saturation (also known as binary phase state). The retention of hydrogen penetrating through the specimen is considered as the 'time-lag' [26], which implies the behavior of hydrogen traps within the materials. By measuring the time where the asymptotic linear portion of the rising permeation curve intersects with x-axis (see Fig. 5.4b), the lag time (t_{lag}) is extracted and further utilized to calculate the hydrogen apparent diffusion coefficient (D_{app}) and mixed diffusion coefficient (D_{mix}) according to the following formula:

$$D = \frac{L^2}{6 * t_{lag}} \qquad (5.2)$$
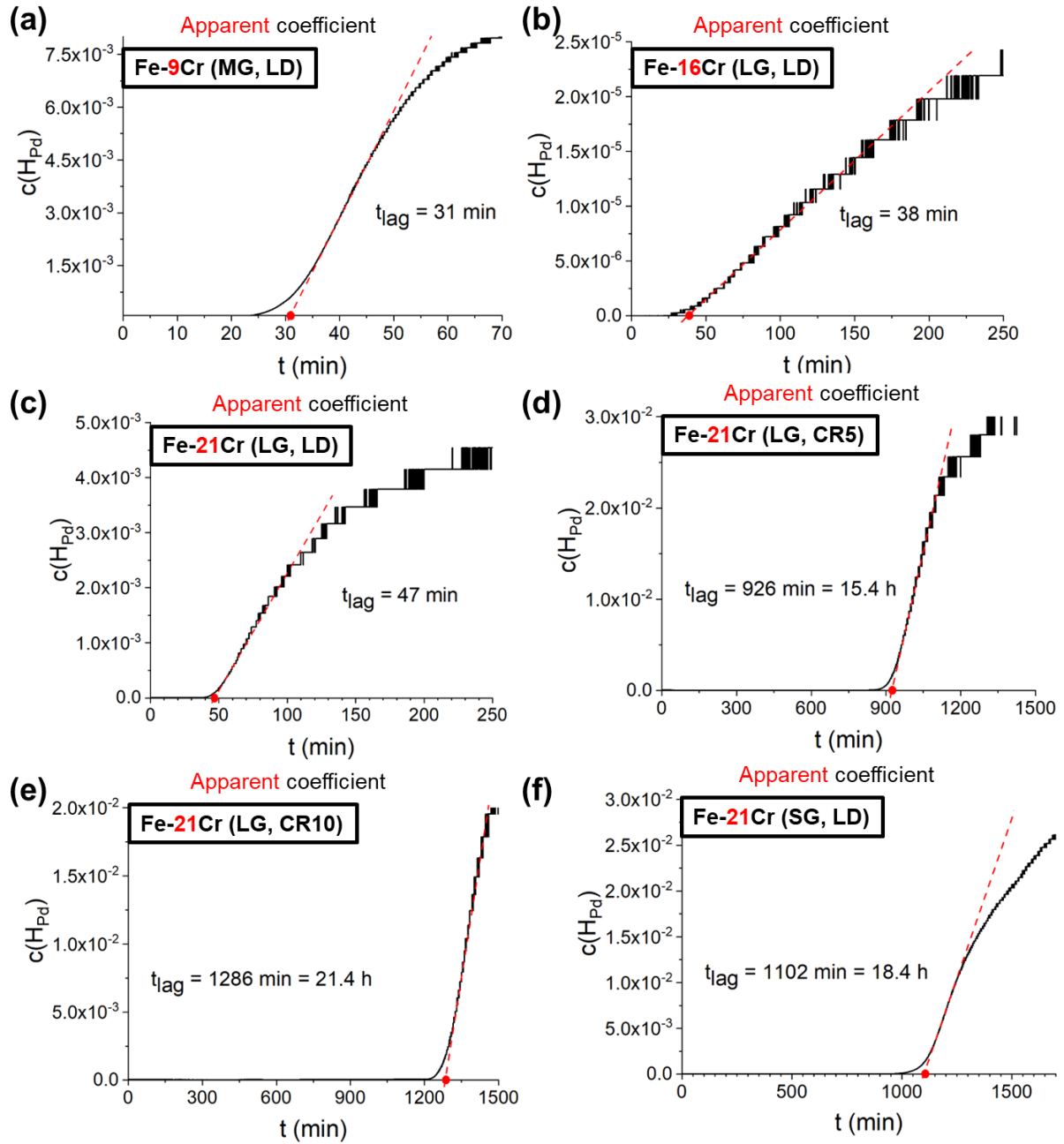
Fig. 5.5 Permeation curves for apparent diffusion coefficient calculation based on the KP measured hydrogen electrode potential in the coated 100 nm Pd layer for different materials: (a) Fe-9Cr (MG, LD); (b) Fe-16Cr (LG, LD); (c) Fe-21Cr (LG, LD); (d) Fe-21Cr (LG, CR5); (e) Fe-21Cr (LG, CR10) and (f) Fe-21Cr (SG, LD). The dotted red line is the slope for the steady-state rate for hydrogen permeation. The intersection of the dotted red line with the x-axis indicates the lag time (t_{lag}).

Fig. 5.5 shows the permeation curves for Fe-Cr alloys with different material conditions of Fe-9Cr, Fe-16Cr and Fe-21Cr (with various dislocation densities and grain sizes) without hydrogen pre-charge for the calculation of the apparent diffusion coefficient. With the

introduction of the continuous hydrogen flux, after filling the obstacles of deep hydrogen trapping sites and reversible hydrogen trapping sites, the diffusive hydrogen finally reaches the Pd-coated side through the interstitial lattice diffusion across the specimen. As opposed to the materials in Fig. 5.5d-f that are charged to saturation state, specimens in Fig. 5.5a-c are charged in accordance with the first step of Fig. 3.3b, which is charged until the system reaches about half its saturation status. As depicted in Fig. 5.5a-c, Fe-9Cr possesses the shortest lag time of 31 min, whereas Fe-21Cr occupies the longest lag time of 47 min and Fe-16Cr has the intermediate lag time of 38 min under the same hydrogen charging condition. The lag time is proportional to the number of hydrogen traps in materials, indicating Fe-21Cr has the highest amount of hydrogen trapping sites. A comparison of the permeation behavior between Fe-21Cr with different dislocation densities and grain sizes is shown in Fig. 5.5c-f. In samples with large grain sizes in the millimeter range, the lag times are prolonged if the dislocation density is large, following the tendency of $t_{lag}(CR10) > t_{lag}(CR5) > t_{lag}(LD)$. Besides, as illustrated in Fig. 5.5c and f, a longer lag time appears for Fe-21Cr alloy with a smaller grain size as well.

In contrast to Fig. 5.5, the lag time in Fig. 5.6 was collected after hydrogen pre-charging followed by releasing of both the reversible trapped hydrogen and diffusive hydrogen for Fe-9Cr, Fe-16Cr and Fe-21Cr (Fig. 3.3b illustrates the procedure). As shown in Fig. 5.6 again, an enhancement in the lag time with increasing Cr content is observed. This coincides well with the previous TDS results revealing that alloys with higher Cr content contain more hydrogen, suggesting Cr is acting as a reversible hydrogen trapping site in ferritic Fe-Cr alloys.
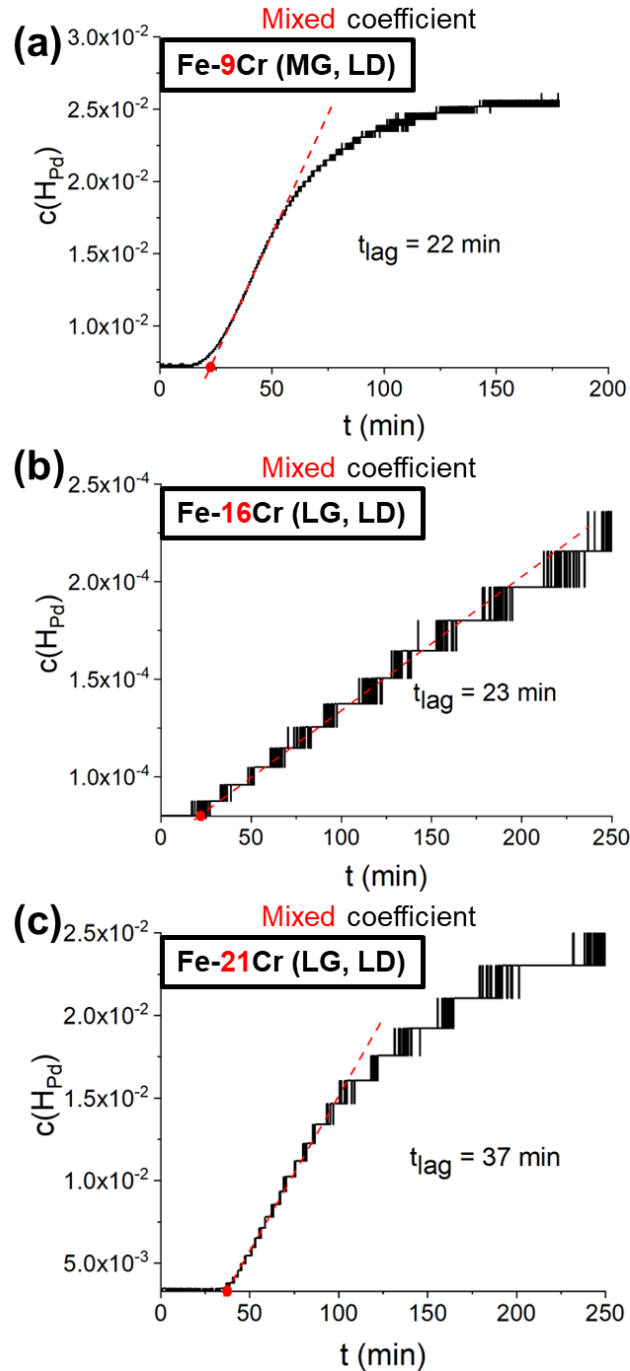
Fig. 5.6 Permeation curves for mixed diffusion coefficient calculation based on the KP measured hydrogen electrode potential for: (a) Fe-9Cr (MG, LD), (b) Fe-16Cr (LG, LD) and (c) Fe-21Cr (LG, LD).

The mixed diffusion coefficient can be calculated based on this lag time, considering the delay originated from the reversible traps and hydrogen diffusion through interstitial sites. Table 5.2 summarizes D_{app} for Fe-9Cr, Fe-16Cr and Fe-21Cr with varying grain sizes and dislocation densities. Note that the difference in dislocation density between the cold-rolled Fe-21Cr

samples of varying thicknesses is small when considering the scale bar. Given such a high dislocation density of 10^{14} m^{-2}, it is hard to differentiate the subtle dissimilarities using ECCI images. Nonetheless, it remains an efficient technique for investigating materials with different magnitudes of dislocation densities.

Table 5.2 Overview of grain size, dislocation densities and hydrogen diffusion coefficients D_{app} calculated based on t_{lag} for Fe-9Cr, Fe-16Cr and Fe-21Cr.

Alloy	Grain size	Dislocation density (m^{-2})	Hydrogen diffusion coefficient (cm^2/s)
Fe-9Cr	149±33 µm	(2.3±1.8)×10^{12}	D_{app}= (4.40±0.11)×10^{-6}
Fe-16Cr	1133±85 µm	(2.6±1.9)×10^{12}	D_{app}= (3.62±0.07)×10^{-6}
Fe-21Cr	1049±51 µm	(2.4±1.9)×10^{12}	D_{app}= (2.86±0.03)×10^{-6}
Fe-21Cr	959±267 µm	(1.3±0.1)×10^{14}	D_{app}= (1.68±0.01)×10^{-7}
		(1.4±0.1)×10^{14}	D_{app}= (1.29±0.01)×10^{-7}
	297±138 nm	(3.7±0.6)×10^{13}	D_{app}= (1.92±0.12)×10^{-8}

5.2.4 Mechanical properties obtained before and during the *in situ* hydrogen charging

Fig. 5.7 displays the evolution of Young's modulus (blue) and hardness (red) in Fe-16Cr (LG, LD) and Fe-21Cr (LG, LD) alloys before and during the cathodic hydrogen charging by utilizing the *in situ* backside hydrogen loading frontside nanoindentation setup. Hydrogen charging is achieved by the potentiostatic method and the corresponding current density at a designated potential is collected and displayed in green curves. The hydrogen charging procedure is consistent with the second stage of the permeation experiment, as shown in Fig. 3.3b. After pre-charge and release of the lightly trapped and diffusive hydrogen, the mechanical reference data are gathered. The initial reference hardness of Fe-21Cr is larger than the Fe-16Cr due to the substitutional solid solution strengthening caused by the strain field formed by the mismatch between Cr and Fe atoms [152-154]. At the onset of a constant hydrogen charging, the hardness increases and follows a sigmoidal shape until reaching a plateau where the quasi-equilibrium state of hydrogen flux is attained. The Young's modulus remains unaltered before and during the hydrogen charging as the setup is stable and the hydrogen

solubility in these two materials is ~0.1 wt.ppm, which is low to cause any changes in Young's modulus as suggested by Zhang et al. [185]. Fe-21Cr exhibits a more pronounced hardness enhancement of 0.24 GPa during hydrogen charging compared to Fe-16Cr of 0.18 GPa with the same applied potential of -1.25 V_{Ref} (Fig. 5.7). Besides, the previous TDS analysis demonstrates that Fe-21Cr absorbs more hydrogen (0.153 wt.ppm) than Fe-16Cr (0.116 wt.ppm). This hydrogen-introduced hardening effect occurs in α-Fe and 13Cr binary alloy as well [18].
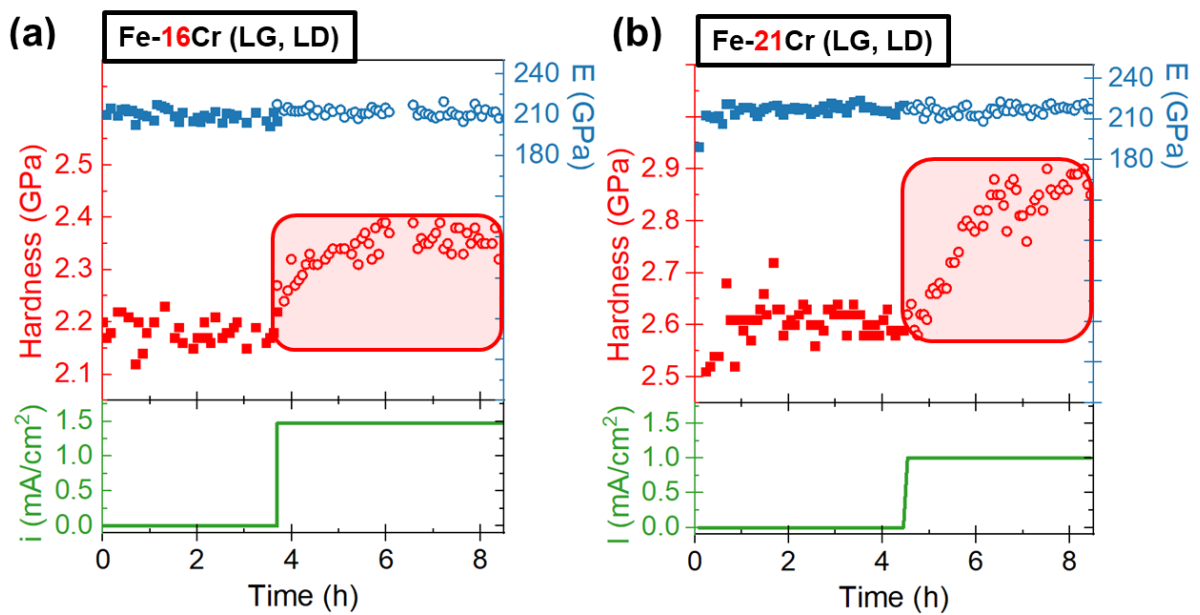
Fig. 5.7 Young's modulus (blue) and hardness (red) evolution with the current density (green) by applying the potential of -1.25 V_{Ref} in (a) Fe-16Cr (LG, LD) and (b) Fe-21Cr (LG, LD) after hydrogen pre-charge and releasing of lightly trapped hydrogen and diffusive hydrogen.

5.3 Discussion

5.3.1 Comparison between nanohardness based and KP based hydrogen permeation behavior (Mixed diffusion coefficient)

During the collection of the nanohardness evolution by employing the *in situ* backside hydrogen loading frontside nanoindentation setup, a continuous Argon flow is purged onto the sample surface to prevent the release of hydrogen and water formation. The hydrogen concentration on the frontside surface could be considered 0 (C_2) throughout the experiments. In addition, the backside of the specimen is under continuous electrochemical hydrogen

charging, the hydrogen concentration upon which is treated as a constant value of C_0 ($C_1=C_0$). The initial hydrogen content is 0 throughout the bulk material ($f(x')=0$). Based on Fick's law, the whole system can be interpreted by the non-steady state diffusion process with constant surface concentrations in a plane sheet model [72]. In summary, the boundary conditions during hydrogen charging for the system are elucidated by the following equations:

$$C_1=C_0, \ x=0, \ t\geq0 \tag{5.3}$$

$$C_2=0, \ x=L, \ t\geq0 \tag{5.4}$$

$$f(x)=0, \ 0<x<L, \ t=0 \tag{5.5}$$

where L is the sample thickness, the solution for the accumulation of hydrogen diffusion flux (J) at the side with negligible hydrogen concentration ($x=L$) obtained by the Laplace transform or the separation of the variable is given as [180]:

$$\frac{J(x)}{J_\infty}=1+2\sum_1^\infty \cos\frac{n\pi x}{L}\exp\left(-\frac{Dn^2\pi^2t}{L^2}\right) \tag{5.6}$$

where J_∞ represents the condition when the exit hydrogen flux reaches the steady state.
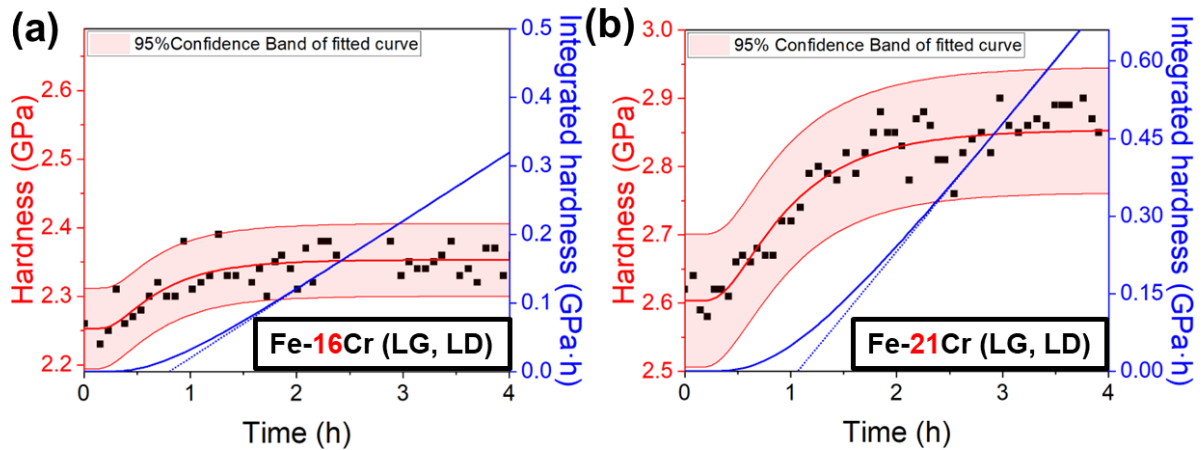
Fig. 5.8 The hardness evolution after hydrogen pre-charging at the commencing of hydrogen charging (black square dots) is simulated based on the non-steady state model of Eq. (5.6) (solid red line) and the integration of the hardness (solid blue line), and the linear fit of the integrated hardness (dotted blue line) for (a) Fe-16Cr (LG, LD) and (b) Fe-21Cr (LG, LD). The light red region indicates the 95 % confidence band for the simulated hardness curve.

The linear increase of the nanohardness with the applied current density in both Fe-16Cr and

77

Fe-21Cr below 5 mA/cm^2 was experimentally observed previously with the same *in situ* backside hydrogen charging setup [133]. Besides, the positive proportional relation between the applied cathodic current density and the hydrogen activity has been demonstrated by Dafft et al. [66] below ~5 mA/cm^2 at ambient temperature. Therefore, using the nanohardness based method to investigate the permeation behavior within a certain range of applied current density (< 5 mA/cm2) in these specific materials is feasible. Fig. 5.8 depicts the original hardness evolution curves (black square dots) for Fe-16Cr (LG, LD) and Fe-21Cr (LG, LD) after hydrogen pre-charge, and the simulated curves (solid red line) derived from Eq. (5.6). Due to the hydrogen concentration gradient across the specimen, the hydrogen flux continuously permeates through the specimen, leading to the enhancement of hardness in the exit side until reaching the steady state. The linear fitting curves (dotted blue line) of the integrated hardness curves (solid blue line) intersect with the x-axis, obtaining the t_{lag} for further hydrogen diffusion coefficient calculation. Since the permeation behavior of these two alloys is independent of the input hydrogen concentration based on this model, it is possible to compare the diffusion coefficients for these two alloys charged with different current densities [193]. Only the J_∞ value alters with various input hydrogen concentrations. A summation of n=16 has been applied in simulating the hardness evolution, which is sufficiently accurate with n>6 according to the ASTM G148-97(2018) standard [111].

Table 5.3 Hydrogen mixed diffusion coefficient calculated from the KP based potentiometric hydrogen electrode method and nanohardness based method in ferritic Fe-16Cr (LG, LD) and Fe-21Cr (LG, LD) alloys.

D_{mix}	Fe-16Cr (LG, LD)	Fe-21Cr LG, LD
KP-based diffusion coefficient (cm^2/s)	$(5.98\pm0.11)\times10^{-6}$	$(3.64\pm0.03)\times10^{-6}$
Nanohardness-based diffusion coefficient (cm^2/s)	$(3.12\pm0.04)\times10^{-6}$	$(1.79\pm0.01)\times10^{-6}$

The mixed diffusion coefficients attained for Fe-16Cr (LG, LD) and Fe-21Cr (LG, LD) acquired from the nanohardness method are listed in Table 5.3. According to both methods, the D_{mix} in Fe-21Cr is smaller than that of Fe-16Cr and the values are within the same order of

magnitude, which verifies the feasibility of applying the nanohardness method in studying hydrogen diffusion in ferritic FeCr alloys. However, it is noticeable that the value of D_{mix} performed by KP-based method is slightly larger than the nanohardness-based method, which is assumed to be mainly attributed to the surrounding atmosphere of the specimens. As displayed in Fig. 3.3a, the Pd coated side measured by KP is sealed in a chamber with nitrogen flow and controlled humidity of 0 rh %, while inside the nanoindentation chamber, the sample is purged by the Argon flux through a pipe without the control of humidity. Consequently, the hydrogen is postulated to permeate through the sample faster within the sealed nitrogen atmosphere, leading to a larger D_{mix}. As a result, for more accurate quantification of D_{mix}, a higher vacuum level is required in the nanoindentation chamber. In addition, the KP-sensed surface is deposited with the Pd foil, which has a lower hydrogen chemical potential [104, 109]. The Pd film takes up the hydrogen from the sample, which may cause the depletion of hydrogen to occur in the vicinity of the utmost surface of the specimen and a larger D_{mix}. Apart from the factors mentioned above, higher scattering in the nanohardness data, variation in the tip's diameter and electrolyte state, etc., may all contribute to the difference between the D_{mix} of the two methods.

The nanohardness based permeation method makes it possible to obtain both the mechanical and diffusion data simultaneously in the bulk materials. It should be noted that we are not proposing a new method of measuring the diffusion coefficient. Instead, this method gives a new prospect in applying the novel *in situ* backside hydrogen loading frontside nanoindentation technique that can dig out more information from one series of experiments. Nevertheless, suppose the material hardness is not linearly related to the applied current density, for example, when the phase transition or hydride formation occurs during hydrogen supplement or when the applied current density exceeds the range of linear relation. In that case, this nanohardness based method is no longer appropriate.

5.3.2 Different hydrogen trapping sites

The hydrogen desorption rate curves shown in Fig. 5.3a are mainly composed of two peak regions of 50-200 °C and 350-450 °C. As investigated by previous work, the small amount of C and O remaining in the alloys (Table 3.1) contributes to the formation of carbides (~40 x 200 nm^2) along the grain boundary and Cr oxides (~4 µm) embedded in the matrix [133]. Desorbed hydrogen peaks in the region of 350-450 °C alter minorly as the amount of the carbides and oxides is low (the peak of which is ~0.0003 wt.ppm/s) in all the materials, compared with the

peak of 50-200 °C. Therefore, the peak between 350-450 °C is postulated to arise due to the carbides and Cr oxides that are assumed to be deep hydrogen trapping sites as illustrated in [170] with the binding energies of -65 kJ/mol and -51-70 kJ/mol, respectively. The experimental evidence for Cr carbides acting as the hydrogen trapping sites in ferritic steels was proposed by Depover et al. [191] by conducting TDS measurements.

As shown in Fig. 5.5, hydrogen diffusion coefficients have an intimate correlation with the hydrogen traps in the samples, including intrinsic traps in the analyzed material and the Pd coating, as well as the interface traps between the interface of alloys and the Pd coating. As we keep the Pd coating deposition parameters and the mechanical surface preparation the same for all the alloys, the influence of traps between interfaces and the traps within the Pd coating is minor, as verified in [105]. Therefore, the intrinsic traps in the materials play an essential role in altering the hydrogen diffusion coefficient.
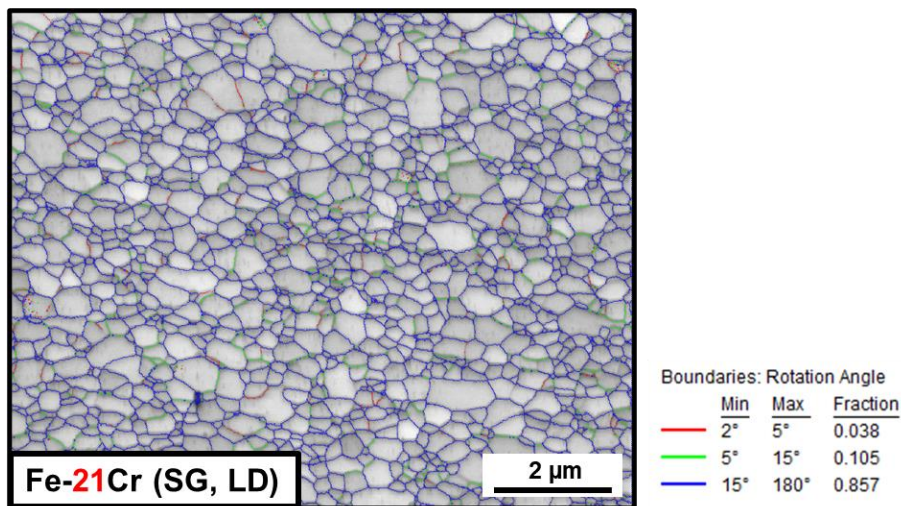
Fig. 5.9 Grain boundary mapping of Fe-21Cr (SG, LD) investigated by the EBSD.

In the cold-rolled Fe-21Cr (LG, CR10), the amount of hydrogen absorbed increased drastically compared with Fe-21Cr (LG, LD), and the apparent diffusion coefficient decreased by one order of magnitude. The majority of the hydrogen is desorbed at 50-100 °C instead of 100-200 °C in Fe-21Cr (LG, CR10) with a higher dislocation density (Fig. 5.3), suggesting dislocation is responsible for the hydrogen released at 50-100 °C. As supported by a similar experiment, the single crystal α-iron was taken to TDS measurement after cathodically hydrogen charging with a current density of 2 mA/cm^2, the peak at 122 °C in the hydrogen evolution rate curve is attributed to the hydrogen released from dislocations with a heating rate of 1°C/min [86]. A broadening and shift to higher temperatures of the hydrogen desorption peak are observed by

TDS measurements with increasing heating rates [194, 195]. Furthermore, observation of dislocations trapping deuterium, an isotope of hydrogen, was achieved by cryogenic atom probe tomography [43]. After the cold rolling treatment, the dislocation density increased in Fe-21Cr from 2.4×10^{12} m^{-2} to 1.4×10^{14} m^{-2} while the grain size stayed within 10 % alteration, as illustrated in Table 5.2. As a result, it is reasonable to treat dislocations as reversible hydrogen trapping sites since deeper hydrogen traps do not have an impact on the permeation test.

Compared with Fe-21Cr (LG, CR10), the HPT-treated Fe-21Cr (SG, LD) has a smaller grain size in the nanometer range and a lower dislocation density. As can be seen in Fig. 5.9, 86 % high angle grain boundaries with larger than 15° rotation angle are involved in the Fe-21Cr (SG, LD) based on the EBSD analysis. Its ~7 times smaller diffusion coefficient can be attributed to the grain boundary trapping effect as the lower dislocation density enhances the diffusion coefficient based on our previous discussion (Table 5.2). Besides, the absorbed hydrogen amount is ~7 times higher in Fe-21Cr (SG, LD) than in Fe-21Cr (LG, CR10). It is noticeable that with reduced grain size, the 100-200 °C peak enhancement is more than the 50-100 °C peak in Fe-21Cr (SG, LD) compared with the Fe-21Cr (LG, LD). It is reasonable to assume that grain boundaries are responsible for the 100-200 °C peak. This result is consistent with the desorbed hydrogen at a heating rate of 1 °C/min in polycrystalline iron, where the hydrogen peak at 142 °C is suggested to stem from grain boundary traps [86]. As the interference from the deep hydrogen traps has been avoided in the permeation experiment, the grain boundaries are proposed in our study to be the reversible trapping site that slow down the motion of hydrogen in these FeCr alloys. This coincides with kinetic Monte Carlo studies of Du et al. [89, 90] in bcc Fe.
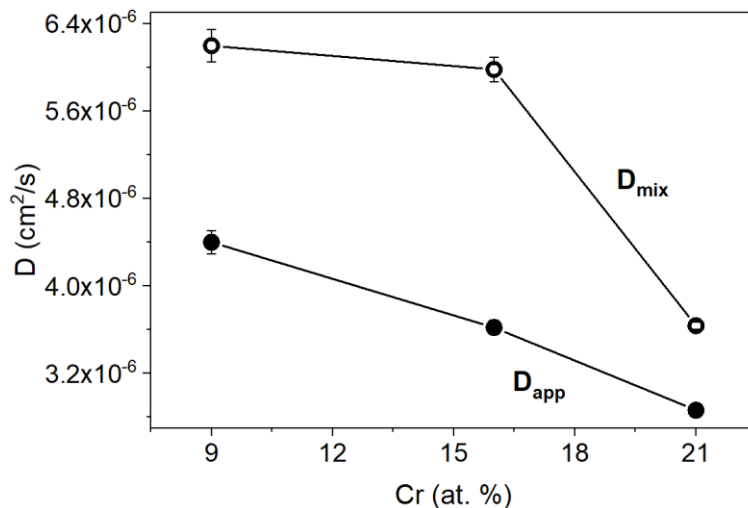
Fig. 5.10 Comparison between mixed and apparent hydrogen diffusion coefficient in Fe-9Cr (MG, LD), Fe-16Cr (LG, LD) and Fe-21Cr (LG, LD) investigated by the KP-based potentiometric hydrogen permeation method.

Fig. 5.10 shows the mixed and apparent hydrogen diffusion coefficient in Fe-9Cr (MG, LD), Fe-16Cr (LG, LD) and Fe-21Cr (LG, LD) measured by the KP-based potentiometric hydrogen permeation method. Considering the deep hydrogen traps, the D_{app} decreases with increased Cr content, following almost a linear relationship in ferritic Fe-9Cr, Fe-16Cr and Fe-21Cr alloys. The reduction of the hydrogen diffusion coefficient of 200 times in Fe-9 wt.%Cr compared with alpha iron was also found by Ramunni et al. [177] based on the numerical calculation. Furthermore, the TDS measurements (Fig. 4a and Table 2) showed that more hydrogen is absorbed in the alloys with higher Cr content, which is consistent with the hot extraction chemical experiment and ab-initio calculations [26, 177]. The only difference between Fe-16Cr and Fe-21Cr is their Cr content since the experiments were performed in the materials subjected to the long-term annealing treatment, excluding the effect of dislocation density, grain size and vacancies. Hence it is reasonable to assume that the principle substitutional element Cr is responsible for Fe-Cr alloys that enhance the intake of hydrogen and reduce hydrogen diffusivity. The crystalline misfit generated by the dimensional difference between Cr and Fe atoms causes a lattice distortion, an enlarged volume for hydrogen. In addition, ab-initio simulation in alpha iron and Fe-9 wt.% Cr suggests that a more stable octahedral interstitial site might be created from the stable tetrahedral sites in pure Fe with the introduction of substitutional Cr atoms [177]. This octahedral site can reserve more hydrogen. The X-ray diffraction technique verifies the normalized lattice dilatation with the presence of Cr in the binary FeCr alloys [189]. In addition, a higher chemical affinity of hydrogen to Cr exists than for Fe, considering the Pauling scale. The binding energy for Cr atoms with hydrogen in ferritic iron is -26-27 kJ/mol, according to the literature [170, 176]. Therefore, Cr atoms that induce the volume change of the interstitial site and create a new type of octahedral interstitial site are assumed to act as reversible hydrogen trapping sites in alpha iron.

As shown in Fig. 5.10, D_{mix} is larger than the D_{app} in the same material, primarily because the deep traps that impede the motion of hydrogen are filled in advance. Without the influence from hydrogen deep traps of oxide and carbides, the increase of D_{mix} is not as pronounced as D_{app}, comparing Fe-16Cr and Fe-9Cr. As discussed above, the dislocations and grain boundaries are reversible trapping sites for the hydrogen. Therefore, the Fe-9Cr with a higher amount of dislocation and grain boundaries than Fe-16Cr shows a greater extent of hydrogen

motion hindrance, reducing the D_{mix} as expected.

In summary, interstitial hydrogen sites introduced by dislocations, grain boundaries and Cr atoms are proposed in this study to be the three kinds of reversible hydrogen trapping sites that influence the first peak region of 50-200 °C in these ferritic FeCr alloys with the specific heating rate of 16 °C/min. This assumption coincides well with the study of Shi et al. [194], which also identified the peak at ~150 °C in α-Fe as the hydrogen absorbed by dislocation as reversible hydrogen traps with the same technique of TDS measurements with a heating rate of 5 °C/min. With a heating rate of ~25 °C/min in bcc model alloy Fe-5 wt.% Ni, the observed dominating 2 peaks for materials after cold rolling and hydrogen charging for 2 h lie at 100-200 °C and 200-300 °C, which is identified as dislocations (desorption energy 29 ± 5 kJ/mol) and vacancies (desorption energy 38 ± 5 kJ/mol), respectively [81]. In the low carbon ferritic steel, which has been cathodically charged with hydrogen, Chen et al. [43] believed that the 100-200 °C peak is due to the hydrogen trapped by dislocations/grain boundaries by TDS measurement as well.

5.4 Conclusion

We have performed an efficient nanohardness based permeation experiment using the *in situ* backside hydrogen loading frontside nanoindentation setup, which enables us to measure the mechanical properties and the diffusion coefficient of the bulk FeCr alloys simultaneously. The viability of the technique has been verified by comparing the mixed diffusion coefficient collected from the specific model bcc metals, which shows a linear relation between hardness and applied current density, with that measured by the KP-based potentiometric hydrogen electrode method. By employing the TDS tests and the KP-based permeation measurements on the model ferritic alloys Fe-9Cr, Fe-16Cr and Fe-21Cr with designated microstructure, the dislocation density, grain boundaries and Cr atoms are systematically investigated and postulated to be the reversible hydrogen trapping sites in these metals. These hydrogen-defects interaction rules can be further applied to other iron-based ferritic steels as they share similar characteristics of defects structure, giving us an insightful perspective in designing the HE-resistant materials by employing/avoiding the formation of various atomic-scale hydrogen traps. The approach of applying the *in situ* backside hydrogen loading frontside nanoindentation technique of studying HE in Fe-Cr alloys can be further allocated to other

iron-based ferritic materials. With further modifications, like sealing the whole system or modifying the specimens' dimensions, its usage range can be extended to other alloy systems with different microstructures of FCC or HCP and materials with coatings.

6. Hydrogen-induced strain hardening effect in ferritic Fe-21Cr alloy (100) orientation with different dislocation densities by *in situ* micropillar compression technique

This section is based on Manuscript 3:

J. Rao, B. Sun, A. Vogel, N. Peter, G. Dehm, M. J. Duarte, *Hydrogen-induced strain hardening effect in ferritic Fe-21Cr alloy (100) orientation with different dislocation density by in situ micropillar compression technique.*

6.1 Introduction

In this section, I used a novel *in situ* backside hydrogen charging technique combined with the micropillar compression test. This approach is ideal for exploring BCC alloys as the sample surface remains pristine throughout the experiment, enabling a post-mortem microstructure characterization with high resolution without further surface preparation. The FeCr alloys have been studied in the same *in situ* backside hydrogen charging nanoindentation apparatus, unveiling a hardening effect and a reduction in the pop-in load during hydrogen charging [61, 133]. However, the micropillar compression test is necessary to simplify the stress state for further deformation analysis with the presence of hydrogen, making it feasible to unveil the HE mechanism in FeCr alloys.

6.2 Results

EBSD images for Fe-21Cr-LD and Fe-21Cr-HD are displayed in Fig. 6.1a and b, respectively. Both metals owe the BCC structure with the grain size of the micrometer range as analyzed via the TSL OIM software. The ECCI technique can visualize the dislocation under two-beam condition as shown in Fig. 6.1c and d. A one order of magnitude higher dislocation density of 8.7×10^{13} /m^2 appears in the specimen Fe-21Cr-HD after cold rolling, compared to the as-annealed specimen Fe-21Cr-LD with a dislocation density of 1.3×10^{12} /m^2. The Fe and Cr distribution was homogeneous within the FeCr alloy, as found by SEM-EDS (see Fig. 6.2).
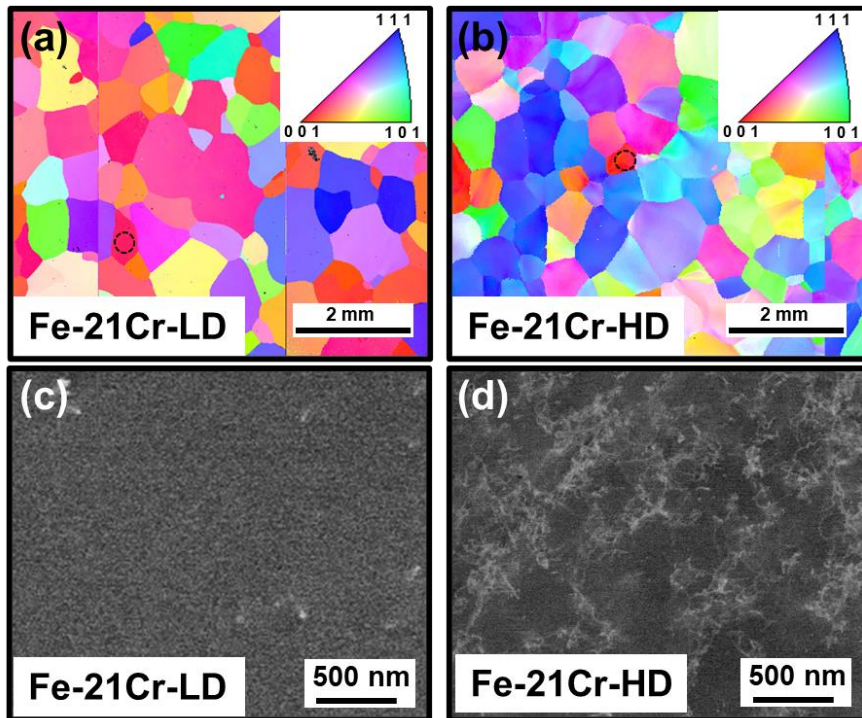
Fig. 6.1 EBSD images for (a) Fe-21Cr-LD and (b) Fe-21Cr-HD. Dislocation observation conducted by ECCI for (c) Fe-21Cr-LD and (d) Fe-21Cr-HD. (i.e. LD: Low dislocation density, HD: High dislocation density)
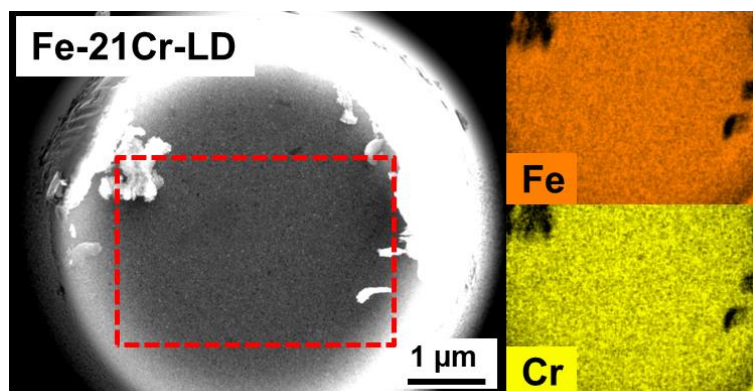
Fig. 6.2 EDS mapping on the surface of Fe-21Cr.

Quantification of the absorbed hydrogen amount in Fe-21Cr-LD and Fe-21Cr-HD is realized by the TDS measurement* after the same externally cathodic hydrogen charging for 4 h with a steady current density of ~2 mA/cm^2, ensuring introducing sufficient hydrogen (Fig. 6.3). Fig. 6.3a displays the hydrogen desorption rate curves, indicating the variation between the two materials mainly lies in the hydrogen desorption peak of 50-250 °C. Dislocations acting as hydrogen trapping sites in alpha iron are considered responsible for the released hydrogen

86

* The TDS measurements were performed by Binhan Sun

in this temperature region [86]. A certain amount of diffusive hydrogen remains in the samples prior to conducting TDS measurements. This residual hydrogen can contribute to the hydrogen desorption rate curves. Therefore, the curves do not start from the value of zero in Fig. 6.3a. Fig. 6.3b is obtained by integrating the curves displayed in Fig. 6.3a to calculate the hydrogen concentration in the samples. Fe-21Cr-HD contains 22.60 at.ppm (0.41 wt.ppm) of hydrogen. In comparison, Fe-21Cr-LD has 6.58 at.ppm (0.12 wt.ppm) of hydrogen, approximately 3 times less than the hydrogen content in Fe-21Cr-HD.

Before performing the micropillar compression tests, it is vital to confirm the existence of hydrogen in the micropillar during the electrochemically hydrogen charging procedure. Before milling the 5 µm pillar by PFIB (Fig. 6.4a)*, Fe-21Cr-LD was deposited with a 100 nm Pd layer by physical vapor deposition for further SKPFM investigation (Fig. 6.4b-e)**. Continuous hydrogen charging with a current density of ~2 mA/cm^2 for 4 h has been applied to the materials in the backside hydrogen charging apparatus, ensuring hydrogen filling inside the entire sample. As labeled in Fig. 6.3, the counting of time starts after taking out the sample from the hydrogen charging setup. The potential mappings over the pillar surface are shown in Fig. 6.4b and c. Darker color indicates lower potential, corresponding to a higher amount of hydrogen concentration. The mapping of 55 min displays darker zones than after 428 min.
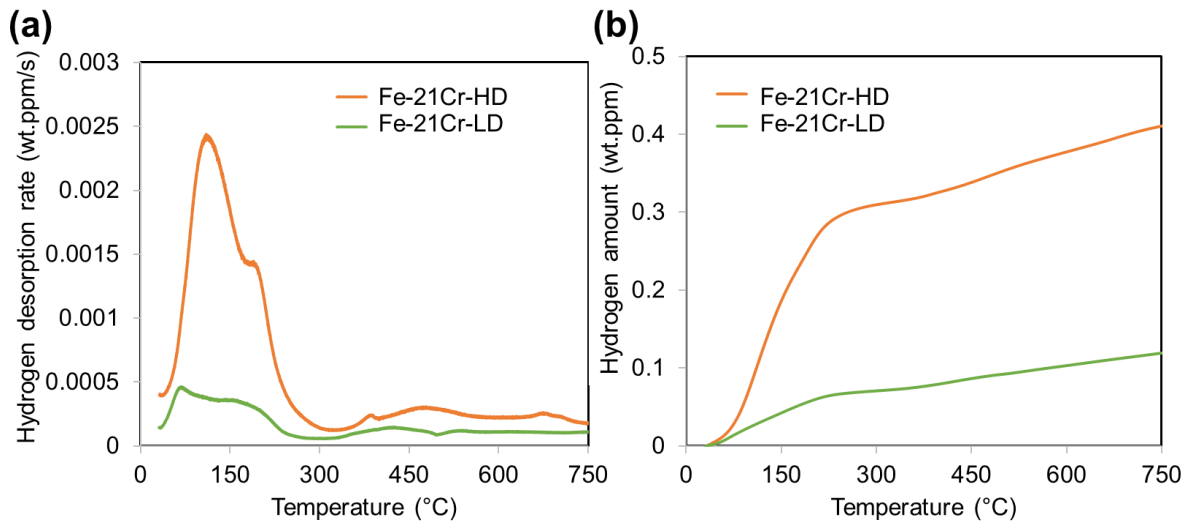
Fig. 6.3 (a) TDS investigated hydrogen desorption rate versus temperature curves and (b) Integrated desorbed hydrogen amount for both Fe-21Cr-LD and Fe-21Cr-HD. A 16 °C/min heating rate has been applied until the samples reach the temperature of 750 °C.

Fig. 6.4d presents the potential evolution curves along the line profile, as highlighted by the

---

* The PFIB pillar was milled by Nicolas Peter
** The SKPFM was performed by Alexandra Vogel

white arrow in Fig. 6.4b and c. The potential decreases with prolonged hydrogen releasing duration as hydrogen diffuses out from specimens continuously. The reduction of potential is first drastically and then slowing down over time, as demonstrated in Fig. 6.4e by extracting the value from the middle 2-3 µm of the line profile (i.e. middle of the pillar) of the potential evolution curves. The potential variation for hydrogen release coincides well with our previous hardness variation at the final hydrogen release stage in the same material of Fe-21Cr [133]. Based on the SKPFM results, hydrogen existence in the micropillars is confirmed. In addition, as the micropillar compression tests are carried out simultaneously during hydrogen charging, even higher hydrogen content is expected in the micropillars under this condition.
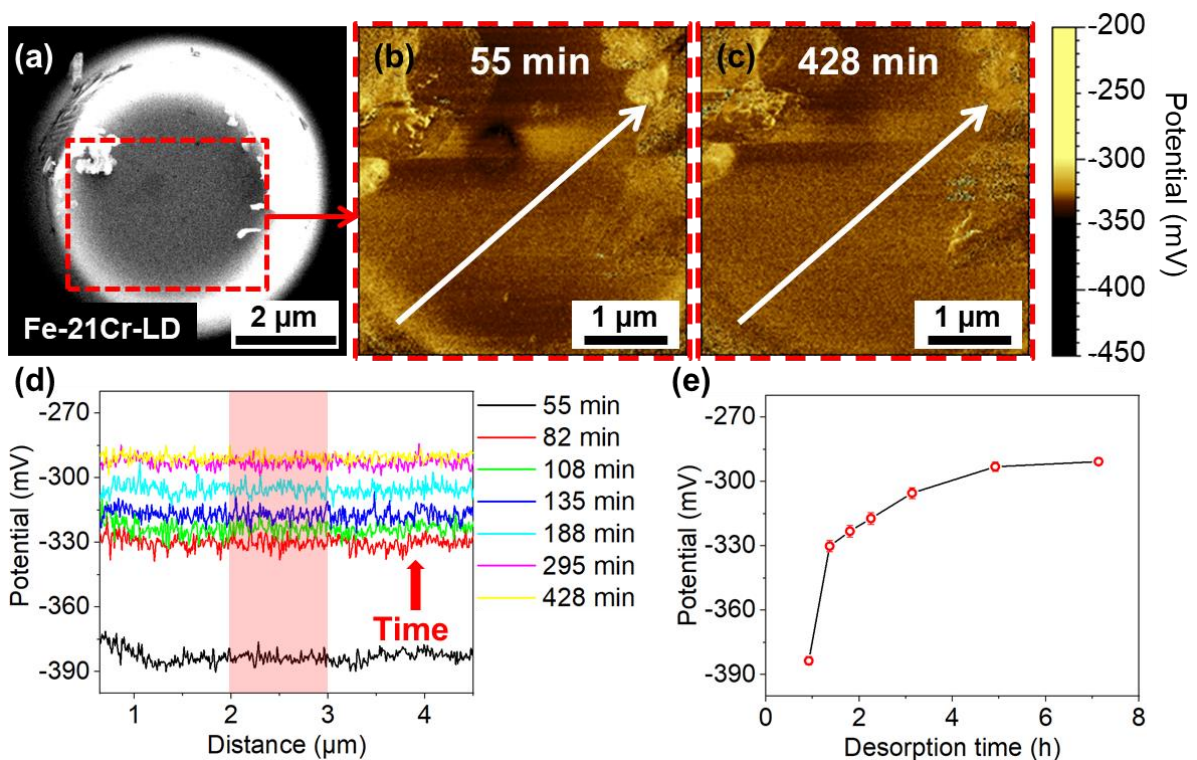
Fig. 6.4 (a) The SEM image of the 5 µm pillar fabricated in Fe-21Cr-LD. The SKPFM potential mapping of the pillar surface cut from Fe-21Cr-LD after taking out the sample from the hydrogen charging setup at (b) 55 min and (c) 428 min, respectively. (d) The evolution of the potential along the white arrows, as highlighted in (b) and (c). (e) The variation of the potential over time in the center of the pillar (highlighted with light red in Fig. 6.4d between the distance of 2-3 µm) after taking out from the hydrogen charging setup.

The representative engineering stress-strain curves in Fig. 6.5 are evaluated based on the micropillar load-displacement curves. Before hydrogen charging, the engineering stress is higher for Fe-21Cr-HD with higher dislocation density (rhombus symbol) than Fe-21Cr-LD

with lower dislocation density (round symbol), as the pre-existing dislocations tangled with each other, enhancing the resistance force for initiating plastic deformation. Regarding the hydrogen effect, compared with the reference condition before hydrogen charging, a more pronounced hardening effect can be observed in micropillars during hydrogen charging in Fe-21Cr.

Based on compression tests exhibited in Fig. 6.5, Fig. 6.6a and b show the averaged flow stress with error bars at plastic strain between 0.005-0.02 before and during hydrogen charging for Fe-21Cr-LD and Fe-21Cr-HD, respectively. During hydrogen charging, the flow stress enhances 57 ± 3 MPa for Fe-21Cr-LD, and the increase in flow stress of 82 ± 17 MPa is also observed in Fe-21Cr-HD compared with the reference condition.
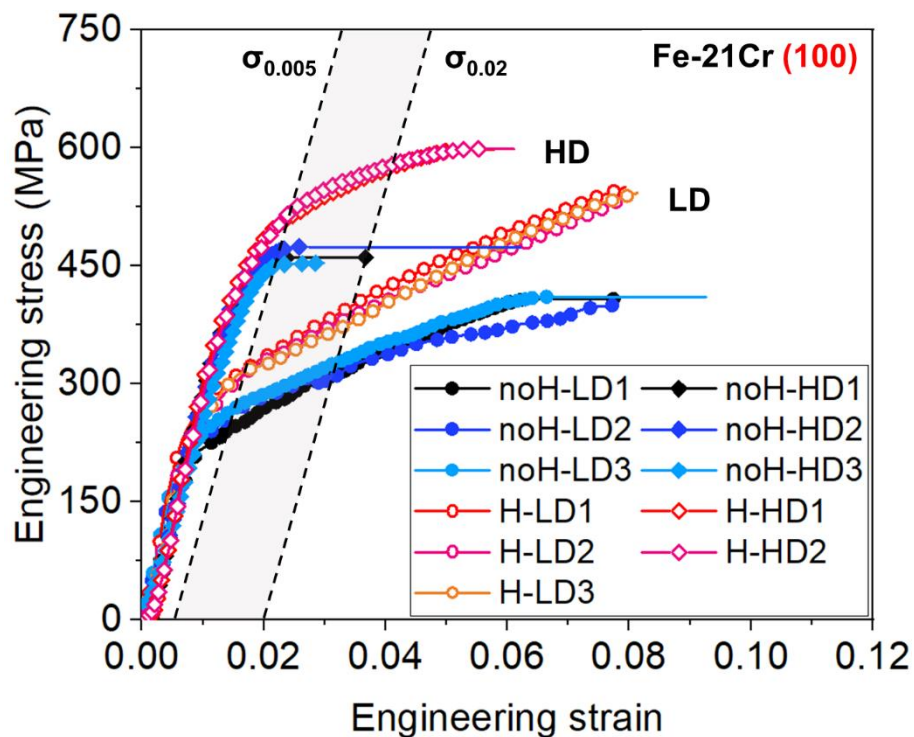
Fig. 6.5 Representative stress-strain curves for Fe-21Cr-LD and Fe-21Cr-HD tested in (100) grain orientation without and with the hydrogen charging (3.6 mA/cm^2). The dashed lines indicate the flow stress at the strain of 0.005 and 0.02, respectively.

The hydrogen effect on the apparent strain hardening rate is exhibited in Fig. 6.6c-d in Fe-21Cr with low and high dislocation density. With low dislocation density, the apparent strain hardening rates are similar. A hydrogen-induced apparent strain hardening rate enhancement can be noticed in Fe-21Cr-HD, the difference between the hydrogen charged and reference pillars is gradually increased after the strain exceeds ~0.017 (Fig. 6.6d). The enhancement of

apparent strain hardening rate in Fe-21Cr-HD is 6.2 ± 1.4 GPa, suggesting a pronounced hardening occurring in materials with high dislocation density.
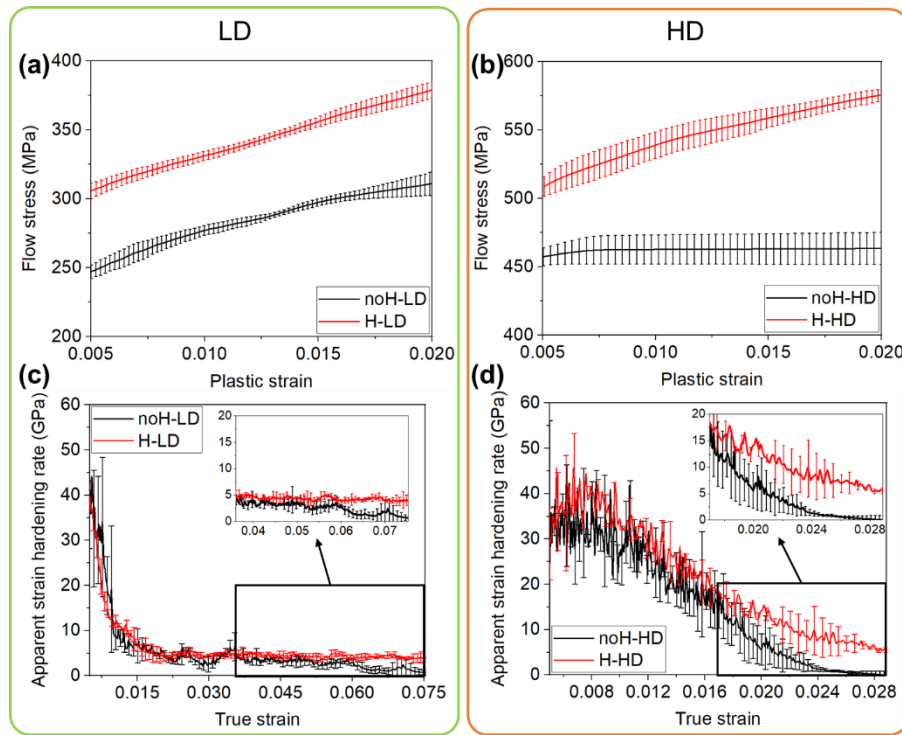
Fig. 6.6 Hydrogen effect on the averaged flow stress with error bar at the plastic strain between 0.005-0.02 and the apparent strain hardening rate for pillars in the materials of: (a) and (c) Fe-21Cr-LD; (b) and (d) Fe-21Cr-HD. The solid black and red lines indicate the conditions before and during hydrogen charging, respectively.

Table 6.1 Euler angles ($\varphi 1$, Φ, $\varphi 2$) of the investigated grains in Fe-21Cr-LD and Fe-21Cr-HD

Sample	$\varphi 1$ (deg)	Φ (deg)	$\varphi 2$ (deg)
Fe-21Cr-LD	147	3	187
Fe-21Cr-HD	122	89	178

Fig. 6.7 shows the morphology of the deformed micropillars by the post-mortem captured SEM images. A slip band highlighted by a solid red line compensates for the major plastic strain in the pillar without hydrogen (Fig. 6.7a) instead of several slip lines (highlighted by the dotted blue lines) for the pillars exposed to hydrogen charging (Fig. 6.7c). In addition, the deformed pillars charged with hydrogen appear to be barrel-shaped. In contrast, Fe-21Cr-HD reveals strong slip steps for hydrogen-free and hydrogen-charged pillars (Fig. 6.7b and d). In addition,

the micropillar exposed to hydrogen (Fig. 6.7d) exhibits a larger density of slip lines and slip traces of 1.2 µm^{-1} compared to Fe-21Cr-HD in hydrogen-free condition of 0.8 µm^{-1}.

Note that the grain orientation deviation of Fe-21Cr-LD to (100) orientation is 19°, while Fe-21Cr-HD has a 13° deviation from the (100) orientation. The Euler angles are listed in Table 6.1.
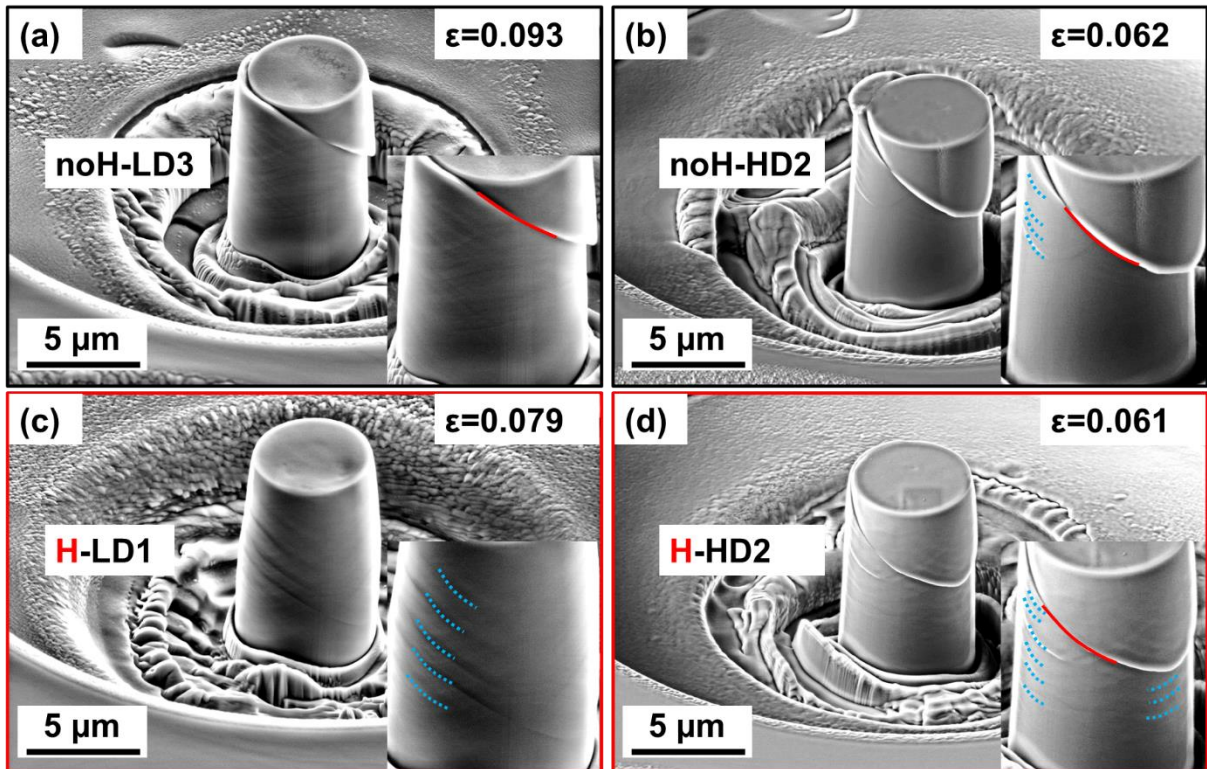
Fig. 6.7 Representative post-mortem SEM micrographs of deformed micropillars for Fe-21Cr-LD (a) before and (c) during hydrogen charging and for Fe-21Cr-HD (a) before and (c) during hydrogen charging. The solid red lines indicate the shear bands while the dotted blue lines indicate the slip steps.

6.3 Discussion

Due to the dislocation forest hardening, the sample with pre-exist higher dislocation density has a higher flow stress at plastic strain between 0.005-0.02 in the reference condition before hydrogen charging (Fig. 6.6). Higher stress required for further plastic deformation can be compensated either by the nucleation of new dislocation sources or by overcoming the resistance force of tangled dislocations [196]. In the meantime, a lack of strain hardening region

can also be discerned in samples with high dislocation density as the critical shear stress for activating the shear band is readily reached as displayed in Fig. 6.7a.

During hydrogen charging, an enhanced apparent strain hardening rate can be observed in the material with high dislocation density (Fig. 6.6c-d). In addition, the increase in apparent strain hardening rate is more drastic after the first strain burst in the mechanical stress-strain curve than the reference state. After the burst, continuous engineering stress enhancement can be observed in Fig. 6.5 during hydrogen charging to compensate the strain instead of one sudden serration in the case without the presence of hydrogen. This burst, corresponds to the pronounced shearing of the slip band, is also visible in the SEM images (solid red line in Fig. 6.7a). However, during hydrogen charging, dense shallower slip lines can be observed (dotted blue lines in Fig. 6.7c) with barrel shape, indicating the intersection of slip planes. This phenomenon coincides with the pillar compression tests conducted by Xufei et al. [197] in tungsten, where multiple slip lines are noticed in pillars exposed to deuterium exposure, compared to one primary slip step found in the reference pillar without hydrogen, suggesting that deuterium facilitates the dislocation nucleation.

Apparently, this hydrogen-induced hardening effect suggests the influence of hydrogen in the dislocation activity within the micropillars, which has also been reported in FeCr alloy by nanoindentation [61, 133]. During hydrogen charging, more slip lines marked with dotted blue lines can be revealed in the deformed micropillars compared to the reference hydrogen-free pillars, indicating the activation of more parallel slip planes inside the micropillars. The dense slip lines on the non-parallel slip planes can be elucidated based on the "Defactant" concept that the presence of hydrogen decreases the line energy of dislocations, causing a more readily dislocation nucleation and multiplication on different slip systems [15-17]. Therefore, those excessive dislocations are assumed to have a higher chance of tangling with each other and forming junctions as they cannot cross slip and act as obstacles for further dislocation motion, leading to the strain hardening known as conventional forest hardening. (Fig. 6.6). As also observed by the previous investigation on the single crystal BCC vanadium hydrogen-charged micropillars, the dense small steps accompanied by strengthened flow stress can be attributed to the facilitated dislocation nucleation and activation of multiple slip systems that promote the interactions between dislocations with the presence of hydrogen [198].

The dislocation that forms an internal stress field in the lattice is generally considered a type of hydrogen trapping site, which impedes the motion of hydrogen [24-28]. The indirect

evidence of deuterium trapped in the dislocations has been discerned by the cryogenic APT [43]. Besides, a higher amount of hydrogen was detected by TDS in alpha iron [86]. According to our TDS measurement in Fig. 6.3b, around 3 times larger amount of hydrogen was absorbed by the Fe-21Cr-HD with higher dislocation density than Fe-21Cr-LD. The hydrogen amount varies mainly between the absorption temperature range of 50-250 °C (Fig. 6.3a), where dislocations are proposed to be responsible [86]. During hydrogen charging, the enhancement of apparent strain hardening rate in Fe-21Cr-HD is 6.2 ± 1.4 GPa, also around 3 times higher than the Fe-21Cr-LD of 1.8 ± 0.9 GPa as shown in the insets of Fig. 6.6c and d. We assume that hydrogen forms the Cottrell clouds within the material during deformation, which retard the motion of dislocation by increasing the resistance force according to the solute drag theory [88]. In addition, enhanced friction stress has been calculated in the Fe-21Cr and high-Mn steel by *in situ* nanoindentation tests [133, 145]. Therefore, a higher amount of hydrogen has more chances to interact with the higher number of dislocations, leading to a more pronounced hardening effect, as observed in Fe-21Cr-HD. However, further characterization in the cross-section of the micropillar is necessary to disclose the interior microstructure evolution that can correlate and further verify the mechanism we postulated.

6.4 Conclusion

The micropillar compression tests have been conducted in Fe-21Cr with different dislocation densities within grains with the same orientation of (100) before and during hydrogen charging by utilizing a novel *in situ* backside electrochemical hydrogen charging apparatus, assembling within the nanoindentation machine. The SKPFM experiment has confirmed the existence of a sufficient amount of hydrogen in the micropillar. Hydrogen charging in micropillars led to the appearance of denser slip lines, accompanied by a discernible hardening effect. This hardening effect is postulated to be a synergistic outcome of multiple mechanisms, including hydrogen-facilitated dislocation nucleation and interaction, the retardance of dislocation motion by hydrogen-formed Cottrell clouds, and the increased lattice friction induced by hydrogen. These combined mechanisms contribute to the observed strengthening response in the micropillars during hydrogen charging.

The Fe-21Cr alloy with higher dislocation density absorbs more hydrogen, as verified by TDS investigation under the same charging condition. Due to the hydrogen-dislocation interaction,

a higher apparent strain hardening rate was observed in the alloy with a higher dislocation density than the one with a lower dislocation density.

7. Hardening relationship with hydrogen and dislocation structure evolution in FeCr alloys by *in situ* nanoindentation scratch across the Σ3 grain boundary

This section is based on Manuscript 4:

J. Rao, K. Angenendt, G. Dehm, M. J. Duarte, *Hardening relationship with hydrogen and dislocation structure evolution in FeCr alloys by in situ nanoindentation scratch across the Σ3 grain boundary.*

7.1 Introduction

Grain boundaries have a crucial impact on the mechanical properties of materials exposed to hydrogen. According to the hydrogen-enhanced decohesion mechanism introduced by Pfeil [6], hydrogen facilitates the crack initiation in the interfaces through reducing the strength of interatomic bonding. Therefore, a comprehensive understanding of hydrogen ingress, diffusion and trapping in the grain boundary region is indispensable in avoiding the early abrupt failure of the materials by hydrogen embrittlement.

Depending on the character and configuration of the microstructure, controversy exists on the performance of different grain boundaries exposed to hydrogen. By mapping the hydrogen distribution with time-of-flight secondary ion mass spectroscopy in polycrystalline Ni, Oudriss [199] proposed that high-angle random grain boundaries (Σ>29) accelerate hydrogen diffusivity by short-circuit diffusion due to the geometrically necessary dislocations in these interfaces, which increase the excess volume of this disordered structure. On the contrary, ordered grain boundaries (Σ3, Σ9 and Σ27) accommodated by defects such as dislocations or vacancies, perform as the hydrogen trapping sites and retard the motion of hydrogen [93, 199]. Besides, the segregation and trapping of hydrogen in the grain boundary area has been indirectly verified by discerning deuterium using cryogenic atom probe tomography in BCC martensitic steel [43]. According to the first-principles simulation in alpha-iron, the close-packed Σ3 (211) grain boundary has unique interstitial sites, which contain higher coordination at the interface between grain boundary and matrix [89]. As a result, this Σ3 (211) grain boundary is proposed to absorb a higher concentration of hydrogen and act as the barrier for hydrogen diffusion, reducing the strain required for fracture. Therefore, to investigate grain

boundary response to hydrogen in alpha iron, we select the Σ3 (211) grain boundary, which might trap a higher amount of hydrogen with a more prominent effect that might be easier to detect based on the studies mentioned above.

The high hydrogen diffusivity in BCC alloys poses challenges in conducting experimental studies, resulting in a lack of comprehensive investigations into the behavior of Σ3 grain boundaries in BCC metals when exposed to hydrogen. As a result, further research efforts are needed to address this gap and gain deeper insights into the behavior of Σ3 grain boundaries under hydrogen exposure in BCC metals. In this study, we investigate the Σ3 grain boundary in a model BCC FeCr alloy with the *in situ* backside hydrogen charging nanoindentation technique. During continuous hydrogen charging, external plastic deformation was induced to the material by scratching, with scratch directions perpendicular to the grain boundary. Coupling high resolution TKD with confocal microscopy and SEM, the character of grain boundary and deformed microstructure is studied with and without hydrogen effects.

7.2 Results

Fig. 7.1a displays the EBSD map of Fe-21Cr, which has a BCC structure with a millimeter large grain size. A ∑3 grain boundary was selected for further investigation as it is reported as a deep trapping site for hydrogen. Therefore, a more pronounced hydrogen effect that can be noticed is expected to occur. Combined with the TKD* analysis based on Fig. 7.6a, the grain boundary is confirmed to be a ∑3 60° (211) grain boundary. In Fig. 7.1b, the grain boundary area is magnified, and scratches are made in opposite directions perpendicularly across the grain boundary. Two single pass scratches were conducted with different hydrogen charging conditions.

Fig. 7.2 exhibits the mechanical depth evolution for scratches under the conditions of hydrogen free reference ("noH pre"), during hydrogen charging with a current density of 1.67 ± 0.09 mA/cm^2 ("H"), and after hydrogen release for 7 hours ("noH post"). The lighter-colored curves (Fig. 7.2a-f) represent the scratch tests carried out at a low load of 20 µN to acquire the surface profile of the material. These profiles serve as the baselines, essential for comparing and analyzing the surface changes in the materials caused by wear while excluding the effects of the surface microstructural features. The indenter is round so that the intersection of the tangents to the curves is considered to be the grain boundary. The darker-colored curves,

* The TKD measurements were performed by Katja Angenendt

corresponding to scratch tests conducted at a higher load of 20 mN, are also displayed in Fig. 7.2a-f. Experimental and simulation studies performed in [200] and [201] confirm that the applied force increases when approaches the grain boundary area. This enhancement in force is attributed to the blocking effect imposed on dislocation extension by the presence of the grain boundary. Once crossing the grain boundary region, the force starts to drop. Therefore, the first upward peak of the depth profile after the downward spike of the darker-colored curve is identified as the grain boundary. It is important to note that this pattern resembles the behavior observed when the tip approaches the chromium oxide as highlighted in Fig. 7.2d by the red arrow, where a distinct upward spike is observed in the curve as well. EDS analysis confirms the existence of chromium oxide in the grain interior, as shown in Fig. S1 of [133], using the same binary alloy Fe-21Cr. The scratch distance is used to distinguish between the microstructure features of the oxide and grain boundary.
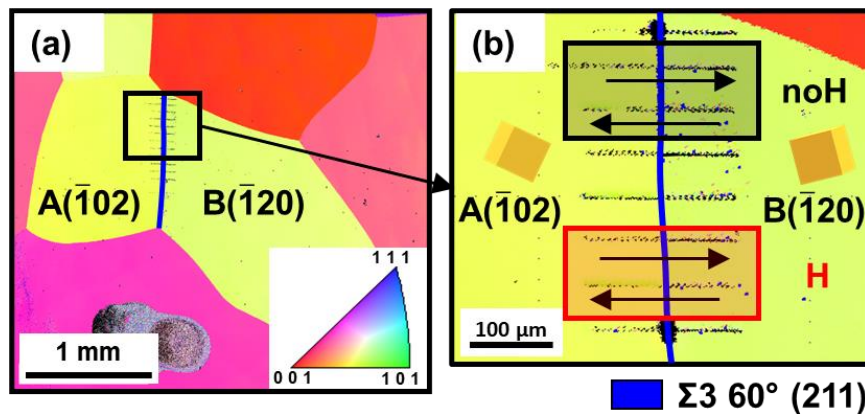
Fig. 7.1 (a) EBSD images for Fe-21Cr with $\Sigma3$ 60° (211) grain boundary. (b) shows the scratches made perpendicular to the grain boundary under hydrogen-free ("noH") and hydrogen-charged ("H") conditions.

In the scratch direction from grain A to B (Fig. 7.2a, c and e), the grain boundary movement is hindered to 7.8±0.2 µm during hydrogen charging, compared to 8.2±0.2 µm under the pre- and post-hydrogen charging conditions. The same hydrogen-induced hindrance of grain boundary movement can be seen in Fig. 7.2b, d and f. During hydrogen charging, the grain boundary migration is 1.0±0.1 µm when scratches are conducted in the direction from grain B to A, which is shorter than before hydrogen charging of 1.3±0.3 µm um and after the hydrogen release of 1.3±0.3 µm. Taking the error bar into account, a solid statement of grain boundary migration cannot be made. Hence, characterization techniques with higher resolution to detect the movement of grain boundary are needed.
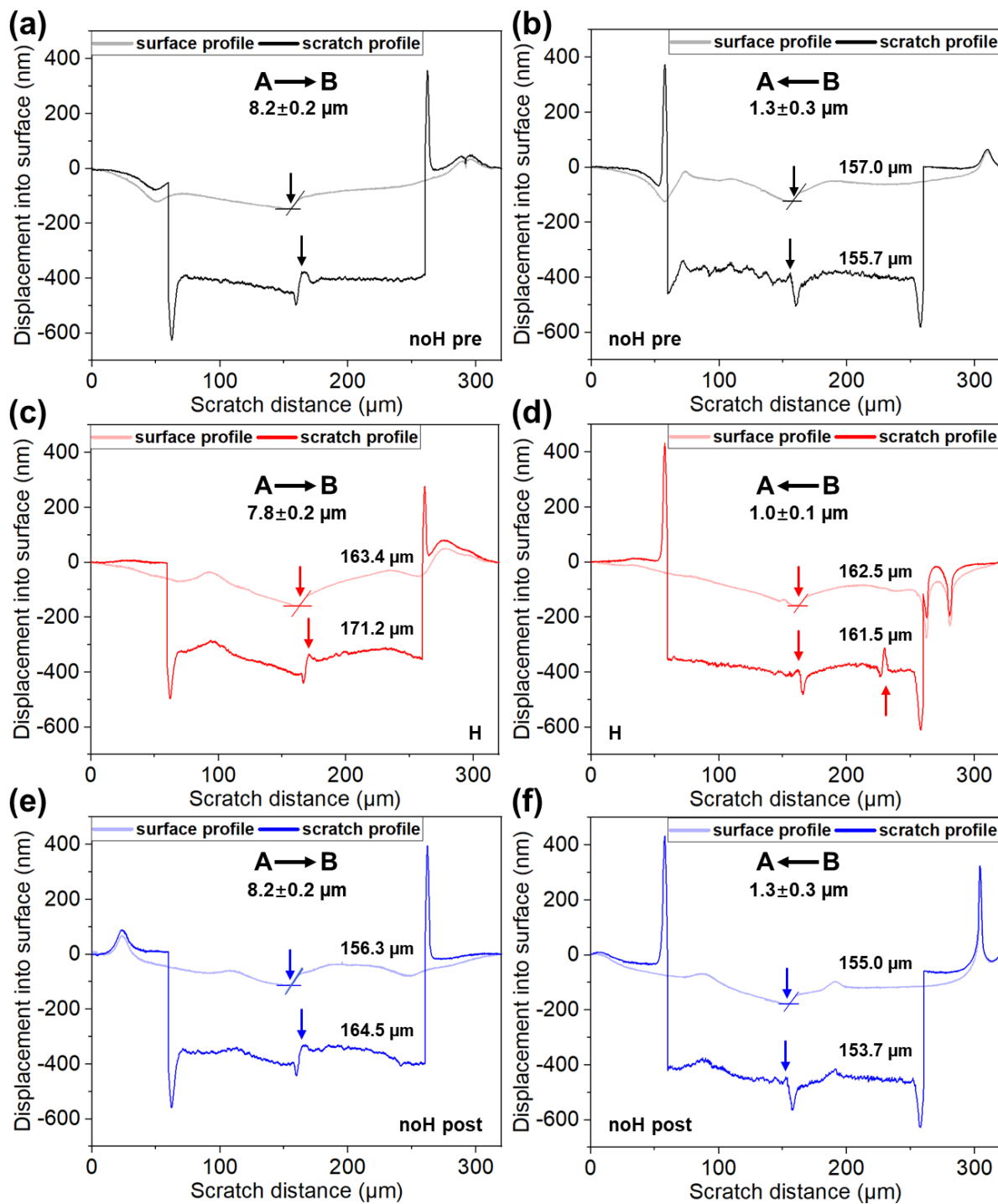
Fig. 7.2 Representative depth curves for the 20 mN wear tracks performed by a 5 µm indenter in the scratch direction from grain A to B of (a) before, (c) during, and (e) after hydrogen charging. With direction from grain B to A, the depth curves of (b) before, (d) during, and (f) after hydrogen charging. (noH pre: scratch conducted before hydrogen charging, H: scratch conducted during hydrogen charging, noH post: scratch conducted after hydrogen release for 7 hours.)
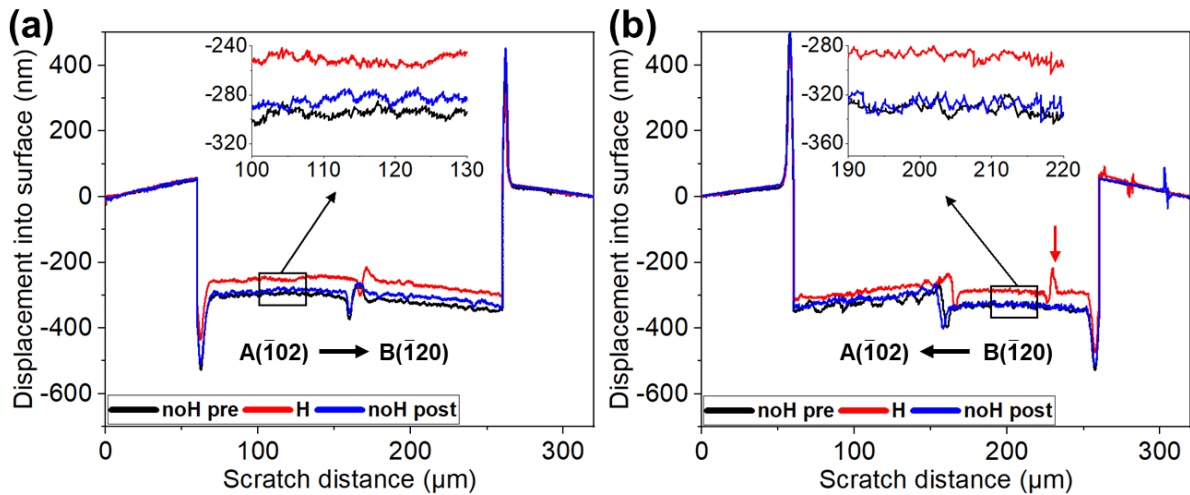
Fig. 7.3 Subtracting the profiling baseline, the relative depth curves of scratches made under three different conditions before, during and after hydrogen charging in the opposite directions of (a) grain A to B; (b) grain B to A.

Subtracting the profiling baseline, the relative depth curves of scratches made under three different conditions before, during and after hydrogen charging are shown in Fig. 7.3g and h with opposite scratch directions. A lower scratch depth can be observed in grain A and grain B during hydrogen charging, compared with the hydrogen free reference condition. Since in all 3 cases (hydrogen-free, hydrogen-loaded and hydrogen-discharged), the same load was applied, a hardening effect is revealed by hydrogen exposure. After 7 hours of hydrogen release, the hydrogen-induced hardening effect reduced drastically, comparable to the initial condition before hydrogen charging, as exhibited in the insets of Fig. 7.3. Therefore, the hydrogen impact on the material is investigated hereafter based on the conditions before and during hydrogen charging. The shift in the middle part of the red curve (i.e. the grain boundary region) is due to the sample location shift according to the profiling curves in Fig. 7.2c and d.

To evaluate the surface topography, post-mortem confocal microscopy analysis is conducted as shown in Fig. 7.4 for scratches with direction from grain A to B and the reverse direction before and during hydrogen charging. Profiles across the scratch grooves at 50 µm from the grain boundary in grains A and B are collected (Fig. 7.4e-h). Shallower grooves with less material loss and a reduction in the height of the pileups are exhibited for scratches during hydrogen charging than for the hydrogen-free sample, indicating that strengthening occurs under hydrogen.
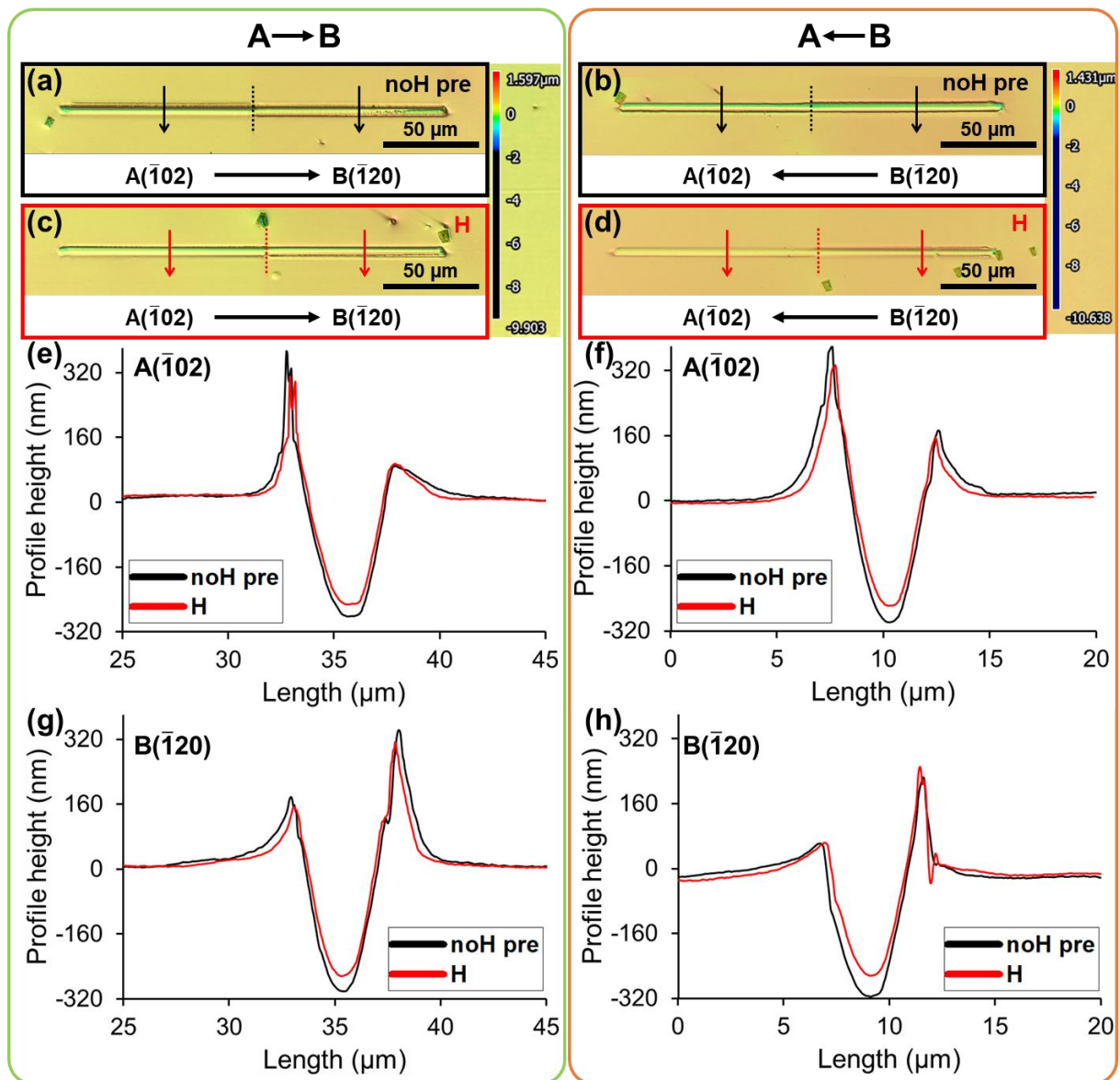
Fig. 7.4 The representative surface topography measured by confocal microscopy for (a) before hydrogen charging in scratch direction from grain A to B, (b) before hydrogen charging in scratch direction from grain B to A, (c) during hydrogen charging in scratch direction from grain A to B and (d) during hydrogen charging in scratch direction from grain B to A. Comparison of depth profiles before and during hydrogen charging across the wear tracks at a depth of 100 µm away from the grain boundary in (e) grain A in scratch direction from grain A to B, (f) grain A in scratch direction from grain B to A, (g) grain B in scratch direction from grain A to B and (h) grain B in scratch direction from grain B to A. The colored scale bar in (a-d) demonstrates the height variation.
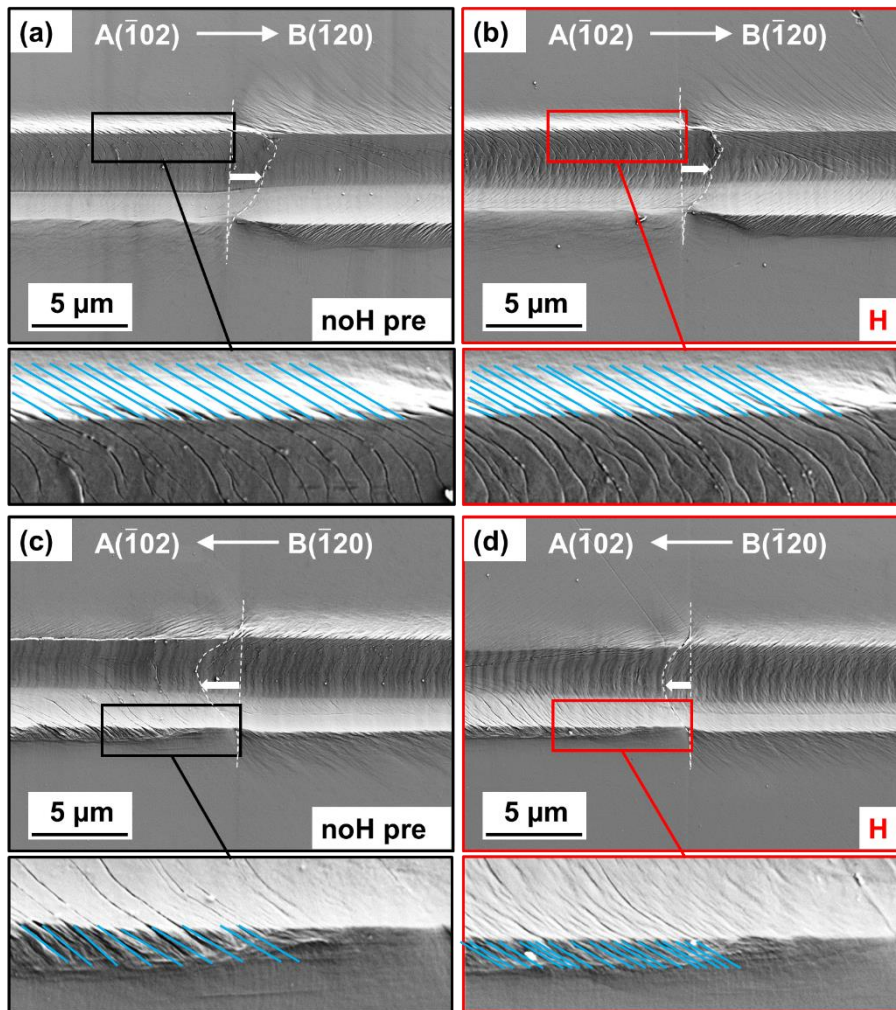
Fig. 7.5 SEM images for wear tracks (a) before hydrogen charging in scratch direction from grain A to B, (b) during hydrogen charging in scratch direction from grain A to B, (c) before hydrogen charging in scratch direction from grain B to A and (d) during hydrogen charging in scratch direction from grain B to A. (Slip traces are highlighted with blue lines in the enlarged images. Migrated grain boundary contour is highlighted by the white dotted lines.)

An enhancement in the density of slip traces is observed in grain A with opposite scratch directions by SEM characterization during hydrogen charging as shown in Fig. 7.5. Under hydrogen, the density of slip traces along the side of the wear tracks with scratch direction from grain A to B increased to 3.7 μm^{-1} from 2.9 μm^{-1} for the hydrogen-free reference. Wear tracks with scratch directions from grain B to A demonstrate the same increase in density of slip traces from 2 μm^{-1} for the hydrogen-free reference to 3.8 μm^{-1} for the hydrogen-charged condition.
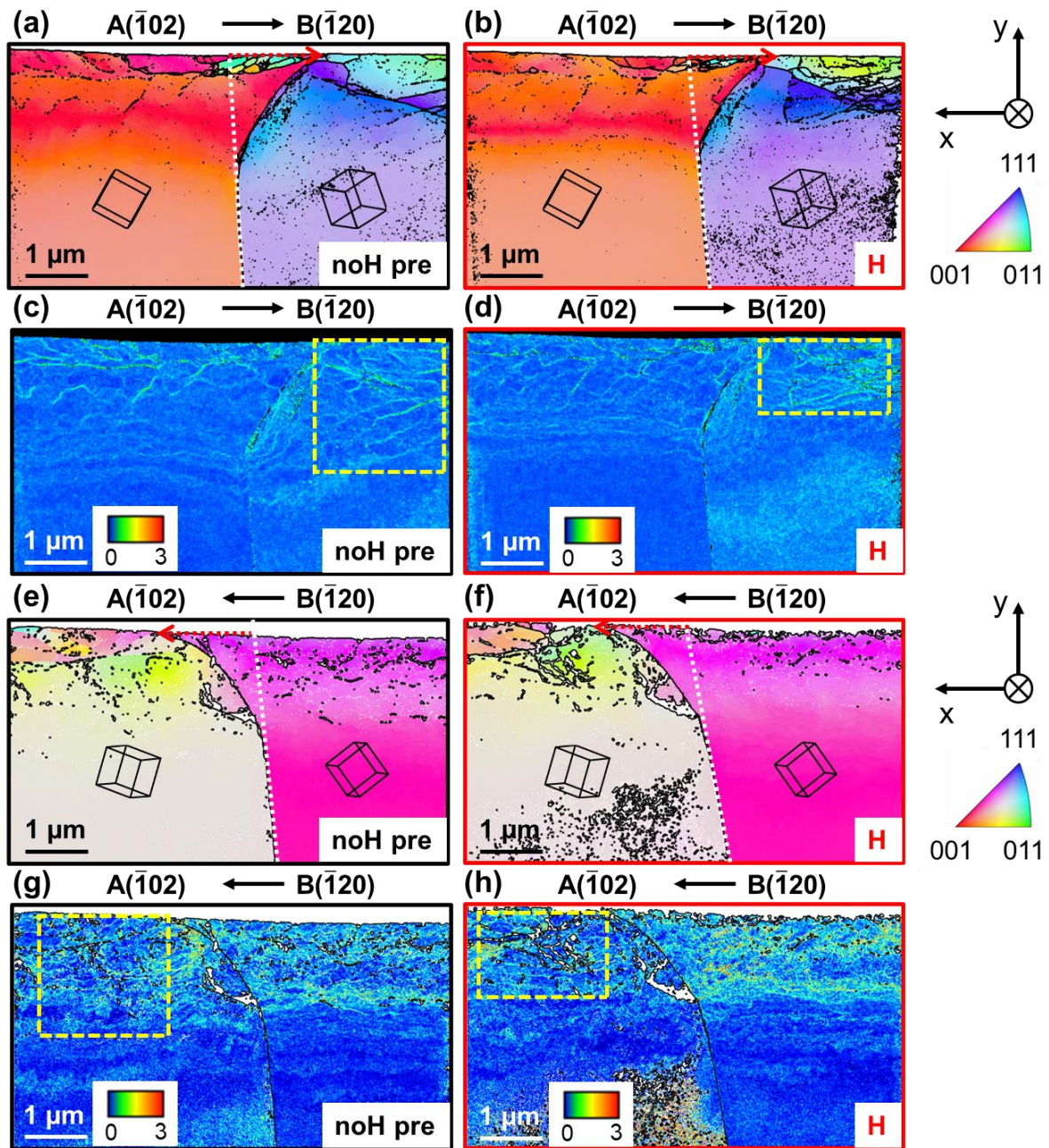
Fig. 7.6 TKD analysis in the cross section area of grain boundary, showing IPF images in scratch direction from grain A to B (a) before and (b) during hydrogen charging, KAM images in scratch direction from grain A to B (c) before and (d) during hydrogen charging, IPF images in scratch direction from grain B to A (e) before and (f) during hydrogen charging, KAM images in scratch direction from grain B to A (g) before and (h) during hydrogen charging.

Moreover, a smaller grain boundary migration of 1.53±0.03 µm from the original position (marked with white dotted lines) can be observed after scratching with direction from grain A to B for the hydrogen charged condition (Fig. 7.5b), compared with 1.74±0.04 µm measured

in Fig. 7.5a for the reference condition. The same phenomenon occurs when performing scratch along the reverse direction from grain B to A. During hydrogen charging, grain boundary shifts less of 1.44 ± 0.02 µm compared to the case without inducing hydrogen with a shift distance of 2.09 ± 0.02 µm. Based on the reduced distance of grain boundary in both scratch directions under the influence of hydrogen, we assume that hydrogen inhibits the movement of grain boundary.

Higher resolution microstructural characterization of the area underneath the scratch deformed grain boundary for both A to B and reverse directions with and without hydrogen charging was achieved by TKD analysis of the FIB-fabricated lamella as show in Fig. 7.6. A shrinkage of plastic region can be observed during hydrogen charging in the grain interior of grain A and B as highlighted by the yellow dotted square in Fig. 7.6c-d and Fig. 7.6g-h, respectively. As proposed in [145] and [133] by simulating the elastoplastic part of load displacement curve, hydrogen-induced enhanced friction force between dislocations is assumed to be the cause of the reduction in the plastic zone.

Fig. 7.6a-b show the bending distance of grain boundaries varies in the scratch direction from grain A to B, and the grain boundary with the presence of hydrogen have shifted by 1.49 ± 0.01 µm, which is smaller than the reference pre-charge condition of 1.55 ± 0.01 µm. Accordingly, the quasi-triangular deformation area adjacent to the grain boundary has also decreased from 1.07 ± 0.01 µm² under the pre-charge condition to 0.85 ± 0.01 µm² under the hydrogen-charged condition. The same phenomenon occurs for the wear tracks carried out in the direction from grain B to A (Fig. 7.6e-f). The bending distance of grain boundary decreases from 1.50 ± 0.01 µm to 1.44 ± 0.01 µm when the hydrogen is introduced. The quasi-triangular deformation region shrinks from 0.82 ± 0.01 µm² to 0.74 ± 0.01 µm² with the hydrogen charging.

7.3 Discussion

The mechanical depth evolution curves based on the scratch tests (Fig. 7.2 and Fig. 7.3) and the depth profiles extracted from the confocal microscopy images (Fig. 7.4) indicate that grains A and B undergo a strengthening effect during hydrogen charging in the grain interior, compared to the hydrogen-free reference condition. This is consistent with earlier observation on the same material by nanoindentation (see Chapter 4) and pillar compression (see Chapter 6) studies [133]. This hydrogen-induced strengthening effect is assumed to be attributed to the altered dislocation activities by hydrogen. According to the surface topography

characterization (Fig. 7.5), the density of the slip traces close to the wear tracks is enhanced during hydrogen charging compared to the hydrogen-free reference samples. This agrees with the plastic deformation traces assessed by KAM images shown in Fig. 7.6c-d. Based on the "defactant" concept that hydrogen decreases the energy required for dislocation nucleation, we assumed that more dislocations are generated and tangled with each other during hydrogen charging, enhancing the strength required for further dislocation motion [15-17]. In addition, hydrogen can be trapped by the strain field of dislocations as indirectly verified by cryogenic APT and numerical analysis [43, 84, 85, 88]. The trapped hydrogen is suggested to form the Cottrell atmosphere that hinders the propagation of dislocation as also illustrated by the solute drag theory [88]. Therefore, the plastic zone is reduced as observed in the cross-section underneath the wear tracks in the individual grains (Fig. 7.6c-d). This is also noticed in Fe-22Mn-0.6C TWIP steel and FeCr alloy by ECCI method [133, 145]. In addition, in BCC alloys, the enhancement in lattice friction also plays an essential role in the hydrogen-induced hardening effect.

In the case of the scratch direction from grain A to B, the grain boundary movement is hindered by ~0.4±0.3 µm for the hydrogen-charged condition as determined from the mechanical data, while the SEM image shows ~0.2±0.1 µm and the TKD mapping shows ~0.06±0.01 µm the decreased distance with the influence of hydrogen. In the opposite direction from grain B to A, during hydrogen charging, the hindrance of grain boundary movement is ~0.3±0.3 µm, compared to the pre-charged condition extracted from the mechanical data, which is comparable to the ~0.06±0.01 µm difference as calculated from the TKD images and the ~0.6±0.1 µm variation that from the SEM images. Although scratch profile analysis can provide valuable information about the surface characteristics of materials and assist in the initial identification of grain boundaries. It should be noted that grain boundary determination from scratch profiles may not be as accurate as TKD analysis, especially with the appearance of recrystallized grains as can be seen in Fig. 7.6a-b. The value of grain boundary movement is nearly zero considering the error bar. Therefore, the investigation using SEM and TKD are applied with their higher resolution in detecting the grain boundary movement. The SEM images show more of the flow of material pushed over the grain boundary. This is in good agreement with Fig. 7.4, where the height of pileups is smaller during hydrogen charging based on the post-mortem confocal microscopy analysis. Nevertheless, with all of the observed evidence above, we believe that the inhibition of grain boundary motion is closely related to hydrogen.

Hydrogen is the inhibitor for the defect movements such as dislocation in metals and alloys. Based on molecular dynamic simulation conducted in α-Fe by Song and Curtin [88], Cottrell atmosphere forms with sufficient induced hydrogen, resisting the migration of dislocation motion and reducing the hydrogen mobility by solute drag. Xie et al. [59] also found the locking effect in dislocation through an environmental TEM. They attributed the hindrance of dislocation motion to the formation of abundant hydrogenated vacancy cluster in aluminium according to the atomistic simulation [59]. The blocking effect of grain boundary with the presence of hydrogen is verified by Lu et al. [196], who perceive by TKD that the grain boundary suppresses the transmission of dislocations in a Ni-based alloy, resulting in the piling up of dislocations in the vicinity of the grain boundary. Hydrogen-facilitated vacancy generation around grain boundaries is supposed to be the reason behind the retardance according to the simulation work [199]. Considering the above reasons, we suppose that the shift reduction in grain boundary and the shrinkage in the grain boundary deformation area are due to hydrogen, which facilitates vacancy formation around the grain boundaries and reduce the mobility of grain boundary.

7.4 Conclusion

In the present study, scratch tests have been performed across the Σ3 grain boundary at the perpendicular direction in a FeCr alloy, combined with an *in situ* backside hydrogen charging nanoindentation apparatus. The post-mortem microstructure characterization was realized by the confocal microscopy and high-resolution TKD method, enabling investigation of the interior and boundary area of the grains.

In the interior of the grains, a strengthening effect based on the mechanical depth evolution curve of scratches was observed during hydrogen charging. A shrinkage in the plastic region and an increase in the density of slip traces was discerned after microstructure characterization. The hydrogen-induced hardening effect is proposed to be attributed to the facilitated dislocation multiplication according to the "defactant" concept, the pinning effect to dislocations that are the trapping sites for hydrogen and the enhanced lattice friction.

In the grain boundary region, the reduction in the shift distance of the grain boundary and the shrinkage of the deformation area in the vicinity of the grain boundary during hydrogen charging compared to the reference condition is postulated to stem from the locking effect of hydrogen. It is speculated that hydrogen retards the mobility of the grain boundary as the

ordered $\Sigma 3$ grain boundary is assumed to trap a high concentration of hydrogen.

Further higher resolution characterization is required to investigate the microstructural evolution around the grain boundary area, especially hydrogen content at grain boundary compared to grain interior. To make a more comprehensive conclusion on the observed grain boundary motion with and without hydrogen, more tests need to be performed to guarantee the reproducibility of the results.

8. Summary and outlook

The ferritic stainless steels have a wide range of applications in industry and daily life. Among them, FeCr alloys occupy an indispensable position in fusion reactors and automotive exhaust systems with high radiation and corrosion resistance. Therefore, this study mainly investigates the binary FeCr model alloys produced in-house with Cr content varying from 9 at.%-21 at.%, ideal for comparing with the simulation works. As overexploitation of fossil fuels has emitted abundant greenhouse gases into the atmosphere, drastically impairing the environment, efforts have been put into implementing hydrogen as a type of clean energy in our society. However, a severe issue, "hydrogen embrittlement", demonstrates a sudden brittle failure of materials with few ppm of hydrogen, commonly occurring during hydrogen production, transportation and consumption. Although many mechanisms have been brought up (such as the HIE, HEDE, HELP, AIDE, HESIVE and the "Defactant" concept), none of which can systematically unveil the underlying principles and controversy still exists. Due to their high hydrogen diffusivity and low hydrogen solubility, ferritic alloys are not well-suited for testing using conventional external hydrogen charging apparatus. This is primarily because a significant amount of hydrogen tends to be lost before subsequent tests can be conducted. Instead, we applied a novel and reliable *in situ* backside hydrogen charging approach, ideal for studying such material as hydrogen can be electrochemically charged into the specimen and the mechanical tests can be conducted in a G200 nanoindentation machine simultaneously. Besides, hydrogen is electrochemically charged into the specimens from the backside, enabling thorough and high-resolution post-mortem characterizations of the microstructure.

Impact of diffusible hydrogen on the nanohardness and dislocation structure of FeCr alloys

We first performed the nanoindentation tests with Berkovich diamond tip in three different ferritic alloys of Fe-4Al, Fe-16Cr and Fe-21Cr to investigate their mechanical response and microstructural evolution with the presence of mobile hydrogen. The influence of deeply trapped hydrogen is excluded by pre-charging the samples for three hours. Analyzing the mechanical evolution curves with different applied polarized potentials correlated to an increased hydrogen supply, a hardening effect exhibits a specific dynamic tendency for the initial transient charging and the hydrogen release stages are discerned. The increase in hardness follows the sigmoidal curve corresponding to the diffusion behavior of hydrogen permeating through the specimen that can be well-fitted to the model based on the non-steady

state. With the effect of deeply trapped hydrogen, the hydrogen release process requires a longer duration of ~4.2 h, about double the time needed for the initial hydrogen charging stage (~2.6 h). The mechanical data for the three alloys are then summarized versus the various current densities, including different grain orientations. When the applied current density is lower than 2-3 mA/cm^2, the hardness variation with respect to the reference hardness follows an initial linear increment with increased current density (i.e. hydrogen content). Once the utilized current density is above the critical range, the slope of the measured hardness variation experiences a drastic decrease, indicating the establishment of a quasi-equilibrium state for the introduced and released hydrogen flux. Furthermore, it is noteworthy that a stronger hardening effect induced by hydrogen is observed in alloys with higher concentrations of substitutional elements within the same grain orientation of (100). Specifically, Fe-21Cr exhibits a 16.7% enhancement in hardness, Fe-16Cr shows a 10.8% enhancement, and Fe-4Al demonstrates a 4.3% enhancement when subjected to a specific current density of 3 mA/cm^2 above the transient region of applied current density. In Fe-21Cr, we also investigated the hydrogen response to different grain orientations. An anisotropic hardness variation during hydrogen charging within different grain orientations of (100), (110), and (111) is noticed. At a current density of 4-5 mA/cm^2, nanohardness increment in (100) grain is 4.7 %, in (110) grain is 14.2 % and in (111) grain is 15.5 %, respectively. However, the Young's modulus remains constant with a maximum deviation of 1.7 % as the hydrogen solubility in all three BCC alloys is extremely low.

After indentation in the hydrogen-free and hydrogen-charged Fe-21Cr samples, the dislocation structure of the cross-section region underneath the imprints was studied by scanning the FIB-fabricated foil with BF-STEM, displaying a 24 % increase in the dislocation density for indents performed during hydrogen charging compared to the uncharged reference. Enhancement in dislocation density is attributed to the hydrogen-facilitated dislocation nucleation, which is supported by the "defactant" concept and the pop-in load reduction as shown in the Appendix I [15-17, 61]. In addition, hydrogen can be trapped by the strain field of dislocations, which forms a Cottrell atmosphere and impedes the dislocation motion according to the "solute drag theory", enhancing the strength required for further dislocation propagation [88]. The elastoplastic range of the CSM hardness curve obtained from nanoindentation was analyzed using the modified Tabor's model [157]. An increase in the lattice friction of 50 MPa caused by the hydrogen can be noticed. The simulation results indicate an increase in lattice friction of 50 MPa, attributed to the presence of hydrogen. In summary, our results support the

interpretation that hydrogen initially facilitates dislocation nucleation following the "defactant" concept; afterwards, Cottrell clouds form and increase the resistance force for dislocation propagation according to the solute drag theory [88]. Furthermore, the higher density of dislocations generated due to the presence of hydrogen leads to increased interactions between dislocations. This impedes the motion of additional dislocations and consequently enhances the strength and hardness of the material.

The measurements reveal that diffusible hydrogen impacts dislocation plasticity most. In contrast, trapped hydrogen does not manifest itself in a pronounced hardness change, considering that deep traps did not release all hydrogen at ambient temperature in the air even after a long time in our studies. It can be speculated that adding more deep traps to materials only helps when exposed to a certain amount of hydrogen, as the diffusible hydrogen controls the enhanced hydrogen plasticity. As higher Cr content results in a higher hydrogen hardening effect, it is feasible to speculate that reducing the amount of Cr in alloys will mitigate the effect of hydrogen. Higher dislocation density plays a more profound role in the hydrogen hardening effect compared to the solute drag stress, meaning the increase of initial dislocation density due to the decrease of the free energy of homogeneous dislocation nucleation is assumed to play a more critical role in HE.

The effect of microstructural features on the hydrogen diffusion coefficient in ferritic FeCr alloys

During cathodic hydrogen charging, a more pronounced hydrogen-induced hardening effect was observed in FeCr alloys with a higher substitutional element content, which is proposed to be attributed to the Cr, serving as the reversible hydrogen trapping site. In addition to Cr content, the hydrogen interactions with other microstructural features of the grain boundary and dislocation density is also systematically investigated. The nanohardness-based diffusion coefficients obtained from the *in situ* backside hydrogen loading frontside nanoindentation setup are $(3.12\pm0.04)\times10^{-6}$ cm^2/s for Fe-16Cr (LG, LD), higher than $(1.79\pm0.01)\times10^{-6}$ cm^2/s for Fe-21Cr (LG, LD), which are comparable to diffusion coefficient acquired from the KP-based potentiometric hydrogen electrode method of $(5.98\pm0.11)\times10^{-6}$ cm^2/s for Fe-16Cr (LG, LD) and $(3.64\pm0.03)\times10^{-6}$ cm^2/s for Fe-21Cr (LG, LD), verifying the viability of this apparatus in measuring the mechanical properties and diffusion coefficient simultaneously. The mixed hydrogen diffusion coefficient without the effect of deep traps and the apparent diffusion coefficient with the influence of deep traps are evaluated in Fe-9Cr, Fe-16Cr and Fe-21Cr. In

combination with the TDS measurements, the dislocation density, grain boundaries and Cr atoms introduced interstitials are proposed to be the reversible hydrogen traps, responsible for the first peak region of 50-200 °C in these ferritic FeCr alloys with the specific heating rate of 16 °C/min by analyzing the TDS desorption curves.

The nanohardness based permeation method makes it possible to obtain both the mechanical and diffusion data simultaneously in the bulk materials. It should be noted that we are not proposing a new method of measuring the diffusion coefficient. Instead, this method gives a new prospect in applying the novel *in situ* backside hydrogen loading frontside nanoindentation technique that can dig out more information from one series of experiments. Nevertheless, suppose the material hardness is not linearly related to the applied current density, for example, when a phase transition or hydride formation occurs during hydrogen charging or when the applied current density exceeds the range of linear relation. In that case, this nanohardness based method is no longer appropriate.

Nevertheless, these discerned hydrogen defect interaction rules can be further applied to other iron-based ferritic steels as they share similar characteristics of defects structure, giving us an insightful perspective in designing the HE-resistant materials by employing/avoiding the formation of various atomic-scale hydrogen traps. The approach of applying the *in situ* backside hydrogen loading frontside nanoindentation technique of studying HE in Fe-Cr alloys can be further allocated to other iron-based ferritic materials. With further modifications, like sealing the whole system or modifying the specimens' dimensions, its usage range can be extended to other alloy systems with different microstructures of FCC or HCP and materials with coatings.

Hydrogen-induced strain hardening effect in ferritic Fe-21Cr alloy (100) orientation with different dislocation density by *in situ* micropillar compression technique

Compared to nanoindentation, the micropillar compression test owes the overwhelming advantage that a simpler uniaxial stress state can be produced, making it more appropriate and effective for unravelling the HE mechanism in FeCr alloys. In the present study, a relatively large 5 µm pillars with a height-to-diameter aspect ratio of 2 for reserving more hydrogen were fabricated by PFIB milling in Fe-21Cr (100) with two different dislocation densities detected by ECCI. The pillar compression tests were performed using the *in situ* backside hydrogen setup inside the nanoindentation machine with the strain rate of 7.5×10^{-3} s^{-1}. Hydrogen content was quantified by the TDS measurements. Fe-21Cr-HD with higher dislocation density uptakes

about three times more hydrogen of 22.60 at.ppm (0.41 wt.ppm) than Fe-21Cr-LD of 6.58 at.ppm (0.12 wt.ppm), indicating dislocation is a type of reversible hydrogen trapping site. The existence of sufficient hydrogen in pillars during cathodic charging was confirmed by the SKPFM potential mapping on the pillar surface. A hardening effect accompanying the appearance of denser slip lines was discerned during hydrogen charging in micropillars, which is postulated to be attributed to a synergistic function of hydrogen-facilitated dislocation nucleation and interaction, the retardance of hydrogen formed Cottrell clouds on dislocation motion, and the increased lattice friction by inducing hydrogen. Due to the hydrogen-dislocation interaction, a 3 times higher apparent strain hardening rate was observed in the alloy with a higher dislocation density than the one with a lower dislocation density. This coincides with the amount of hydrogen absorbed in the materials.

As the feasibility of *in situ* pillar compression tests has been verified, in addition to dislocation, the influence of other microstructural features, such as grain boundary, phase boundary, precipitate and vacancy, can also be investigated utilizing this method, drastically enhancing the reliability of the observed microstructural evolution compared with the *in situ* nanoindentation tests. The role of dislocation in response to hydrogen in materials indicates that less dislocation should be introduced to prevent the effect of hydrogen.

Dislocation structure evolution in FeCr alloys by *in situ* nanoindentation scratch across the Σ3 grain boundary

The grain boundary is critical in determining the mechanical properties of polycrystal materials. Here, we conducted the nanoscratch experiments with a passing velocity of 1 µm/s using a 5 µm spherical tip along the reversible directions perpendicular to the Σ3 grain boundary that is supposed to trap relatively more hydrogen during hydrogen charging. Combining with the confocal microscopy analysis of the lateral profile, a hydrogen-induced hardening effect consistent with previous studies was observed based on the mechanical data. The post-mortem characterization of the wear tracks affected by hydrogen exhibits a higher dislocation density in comparison to the reference condition as noticed in the vicinity of the grain boundary by SEM. Besides, KAM analysis of the thin foil extracted from the cross-section underneath the grain boundary through the TKD technique reveals a more extensive deformation region confined within a smaller plasticity region. In the grain boundary region, the reduction in the shift distance of the grain boundary and the shrinkage of the deformation region near the grain boundary during hydrogen charging compared to the reference condition

is assumed to be due to the locking effect of hydrogen. The ordered Σ3 grain boundary is postulated to trap a high concentration of hydrogen. The trapped hydrogen retards the mobility of the grain boundary.

More experiments are necessary to thoroughly investigate the microstructural evolution encompassing the grain boundary region. These studies are crucial to establish a more conclusive understanding of the observed grain boundary migration during hydrogen charging.

9. Appendix I: Pop-in load variation during hydrogen charging

Fig. 9.1 shows that with a higher applied cathodic potential, corresponding to a higher hydrogen activity [66], the pop-in loads on average of 50 normal percentiles decrease from the reference 0.135 mN without hydrogen charging to 0.119 mN for -1.3 V_{Ref}, 0.099 mN for -1.4 V_{Ref}, and 0.086 mN for -1.6 V_{Ref}, respectively.

Fig. 9.1 Cumulative curves for pop-in load variation before and during hydrogen charging with different applied potentials in Fe-21Cr (110)c as displayed in Table 4.1.

List of figures

List of tables

Reference

[1] B. Sun, D. Wang, X. Lu, et al., Current Challenges and Opportunities Toward Understanding Hydrogen Embrittlement Mechanisms in Advanced High-Strength Steels: A Review. Acta Metallurgica Sinica, 2021: p. 1-14.

[2] A. Barnoush and H. Vehoff, Recent developments in the study of hydrogen embrittlement: Hydrogen effect on dislocation nucleation. Acta Materialia, 2010. **58**(16): p. 5274-5285.

[3] W. H. Johnson, On some remarkable changes produced in iron and steel by the action of hydrogen and acids. 1875, Nature Publishing Group.

[4] J. Von Pezold, L. Lymperakis, and J. Neugebeauer, Hydrogen-enhanced local plasticity at dilute bulk H concentrations: The role of H–H interactions and the formation of local hydrides. Acta Materialia, 2011. **59**(8): p. 2969-2980.

[5] G. Leyson, B. Grabowski, and J. Neugebauer, Multiscale description of dislocation induced nano-hydrides. Acta Materialia, 2015. **89**: p. 50-59.

[6] L. B. Pfeil and P. Character, The effect of occluded hydrogen on the tensile strength of iron. Proceedings of the Royal Society of London Series A, 1926. **112**(760): p. 182-195.

[7] R. Oriani and P. Josephic, Equilibrium aspects of hydrogen-induced cracking of steels. Acta Metallurgica, 1974. **22**(9): p. 1065-1074.

[8] A. R. Troiano, R. Gibala, and R. Hehemann, Hydrogen embrittlement and stress corrosion cracking: a Troiano Festschrift. 1984: ASM International.

[9] C. D. Beachem, A new model for hydrogen-assisted cracking (hydrogen "embrittlement"). Metallurgical Materials Transactions B, 1972. **3**(2): p. 441-455.

[10] S. Lynch, Discussion of some recent literature on hydrogen-embrittlement mechanisms: addressing common misunderstandings. Corrosion Reviews, 2019. **37**(5): p. 377-395.

[11] S. Lynch, Environmentally assisted cracking: overview of evidence for an adsorption-induced localised-slip process. Acta Metallurgica, 1988. **36**(10): p. 2639-2661.

[12] S. Lynch, Metallographic contributions to understanding mechanisms of environmentally

assisted cracking. Metallography, 1989. **23**(2): p. 147-171.

[13] S. Lynch, Comments on "A unified model of environment-assisted cracking". Scripta Materialia, 2009. **61**(3): p. 331-334.

[14] S. Lynch, Hydrogen embrittlement (HE) phenomena and mechanisms. Corrosion Reviews, 2012. **30**(3-4): p. 105-123.

[15] R. Kirchheim, Reducing grain boundary, dislocation line and vacancy formation energies by solute segregation: I. Theoretical background. Acta Materialia, 2007. **55**(15): p. 5129-5138.

[16] R. Kirchheim, Reducing grain boundary, dislocation line and vacancy formation energies by solute segregation: II. Experimental evidence and consequences. Acta Materialia, 2007. **55**(15): p. 5139-5148.

[17] R. Kirchheim, Revisiting hydrogen embrittlement models and hydrogen-induced homogeneous nucleation of dislocations. Scripta Materialia, 2010. **62**(2): p. 67-70.

[18] M. Nagumo, Fundamentals of hydrogen embrittlement. 2016: Springer.

[19] J. Song and W. Curtin, A nanoscale mechanism of hydrogen embrittlement in metals. Acta Materialia, 2011. **59**(4): p. 1557-1569.

[20] P. Novak, R. Yuan, B. Somerday, et al., A statistical, physical-based, micro-mechanical model of hydrogen-induced intergranular fracture in steel. Journal of the Mechanics Physics of Solids, 2010. **58**(2): p. 206-226.

[21] A. Barnoush, Hydrogen embrittlement, revisited by in situ electrochemical nanoindentation. 2007.

[22] A. Pundt and R. Kirchheim, HYDROGEN IN METALS: Microstructural Aspects. Annual Review of Materials Research, 2006. **36**(1): p. 555-608.

[23] M. Koyama, M. Rohwerder, C. C. Tasan, et al., Recent progress in microstructural hydrogen mapping in steels: quantification, kinetic analysis, and multi-scale characterisation. Materials Science Technology, 2017. **33**(13): p. 1481-1496.

[24] X. Li, J. Zhang, S. Shen, et al., Effect of tempering temperature and inclusions on hydrogen-assisted fracture behaviors of a low alloy steel. 2017. **682**: p. 359-369.

[25] S. K. Dwivedi and M. Vishwakarma, Effect of hydrogen in advanced high strength steel materials. International Journal of Hydrogen Energy, 2019. **44**(51): p. 28007-28030.

[26] E. R. Hans Jürgen Grabke, Absorption and diffusion of hydrogen in steels. Materiali in tehnologije, 2000. **34**(6): p. 331.

[27] I. Maroef, D. Olson, M. Eberhart, et al., Hydrogen trapping in ferritic steel weld metal. International Materials Reviews, 2002. **47**(4): p. 191-223.

[28] T. Depover and K. Verbeken, The effect of TiC on the hydrogen induced ductility loss and trapping behavior of Fe-C-Ti alloys. Corrosion Science, 2016. **112**: p. 308-326.

[29] S. Wang, N. Hashimoto, and S. Ohnuki, Effects of hydrogen on activation volume and density of mobile dislocations in iron-based alloy. Materials Science and Engineering: A, 2013. **562**: p. 101-108.

[30] H. Hagi, Y. Hayashi, and N. Ohtani, Diffusion coefficient of hydrogen in pure iron between 230 and 300 K. Transactions of the Japan institute of metals, 1979. **20**(7): p. 349-357.

[31] G. Gottstein, Physical foundations of materials science. 2013: Springer Science & Business Media.

[32] D. Araújo, E. Vilar, and J. P. Carrasco, A critical review of mathematical models used to determine the density of hydrogen trapping sites in steels and alloys. International Journal of Hydrogen Energy, 2014. **39**(23): p. 12194-12200.

[33] P. Bruzzoni, R. Carranza, J. C. Lacoste, et al., Hydrogen diffusion in α-iron studied using an electrochemical permeation transfer function. Electrochimica Acta, 1999. **44**(16): p. 2693-2704.

[34] I. S. S. Forum, The Ferritic Solution - Properties, Advantages and Applications: The Essential Guide to Ferritic Stainless Steels. 2007: Brussels.

[35] A. J. Samin, D. A. Andersson, E. F. Holby, et al., First-principles localized cluster expansion study of the kinetics of hydrogen diffusion in homogeneous and heterogeneous Fe-Cr alloys. Physical Review B, 2019. **99**(1): p. 014110.

[36] D. Terentyev, F. Bergner, and Y. Osetsky, Cr segregation on dislocation loops enhances

hardening in ferritic Fe–Cr alloys. Acta Materialia, 2013. **61**(5): p. 1444-1453.

[37] C. D. Hardie and S. G. Roberts, Nanoindentation of model Fe–Cr alloys with self-ion irradiation. Journal of Nuclear Materials, 2013. **433**(1-3): p. 174-179.

[38] P. Grammatikopoulos and K. Nordlund, Molecular dynamics simulation of Cr-precipitate demixing in FeCr alloys. Radiation Effects Defects in Solids, 2014. **169**(7): p. 646-654.

[39] S. M. Dubiel and J. Cieślak, Sigma-phase in Fe-Cr and Fe-V alloy systems and its physical properties. Critical reviews in solid state materials sciences, 2011. **36**(4): p. 191-208.

[40] O. Kubaschewski, Iron—Binary phase diagrams. 2013: Springer Science & Business Media.

[41] A. Cerezo, J. Hyde, M. Miller, et al., Atomistic modelling of diffusional phase transformations. Philosophical Transactions of the Royal Society of London, Series A, 1992. **341**(1661): p. 313-326.

[42] H. Okamoto and T. Massalski, Binary alloy phase diagrams. Vol. 1. 1990: ASM International, Materials Park, OH, USA.

[43] Y.-S. Chen, H. Lu, J. Liang, et al., Observation of hydrogen trapping at dislocations, grain boundaries, and precipitates. Science, 2020. **367**(6474): p. 171-175.

[44] Y.-S. Chen, D. Haley, S. S. Gerstl, et al., Direct observation of individual hydrogen atoms at trapping sites in a ferritic steel. Science, 2017. **355**(6330): p. 1196-1199.

[45] D. R. Lide, CRC handbook of chemistry and physics. Vol. 85. 2004: CRC press.

[46] M. Bououdina, D. Grant, and G. Walker, Review on hydrogen absorbing materials—structure, microstructure, and thermodynamic properties. International Journal of Hydrogen Energy, 2006. **31**(2): p. 177-182.

[47] D. Shih, I. Robertson, and H. Birnbaum, Hydrogen embrittlement of α titanium: in situ TEM studies. Acta Metallurgica, 1988. **36**(1): p. 111-124.

[48] D. Teter, I. Robertson, and H. Birnbaum, The effects of hydrogen on the deformation and fracture of β-titanium. Acta Materialia, 2001. **49**(20): p. 4313-4323.

[49] V. Olden, C. Thaulow, and R. Johnsen, Modelling of hydrogen diffusion and hydrogen induced cracking in supermartensitic and duplex stainless steels. Materials & Design, 2008. **29**(10): p. 1934-1948.

[50] B. Sun, D. Palanisamy, D. Ponge, et al., Revealing fracture mechanisms of medium manganese steels with and without delta-ferrite. Acta Materialia, 2019. **164**: p. 683-696.

[51] P. Sofronis and H. K. Birnbaum, Mechanics of the hydrogen/dislocation/impurity interactions: I. Increasing shear modulus. Journal of the Mechanics Physics of Solids, 1995. **43**(1): p. 49-90.

[52] I. M. Robertson, P. Sofronis, A. Nagao, et al., Hydrogen embrittlement understood. Metallurgical Materials Transactions A, 2015. **46**(6): p. 2323-2341.

[53] M. Itakura, H. Kaburaki, M. Yamaguchi, et al., The effect of hydrogen atoms on the screw dislocation mobility in bcc iron: A first-principles study. Acta Materialia, 2013. **61**(18): p. 6857-6867.

[54] H. Matsui, H. Kimura, and S. Moriya, The effect of hydrogen on the mechanical properties of high purity iron I. Softening and hardening of high purity iron by hydrogen charging during tensile deformation. Materials Science and Engineering, 1979. **40**(2): p. 207-216.

[55] G. Bond, I. Robertson, and H. Birnbaum, Effects of hydrogen on deformation and fracture processes in high-ourity aluminium. Acta Metallurgica, 1988. **36**(8): p. 2193-2197.

[56] M. Nagumo, K. Ohta, and H. Saitoh, Deformation induced defects in iron revealed by thermal desorption spectroscopy of tritium. Scripta Materialia, 1999. **40**(3): p. 313-319.

[57] K. Takai, H. Shoda, H. Suzuki, et al., Lattice defects dominating hydrogen-related failure of metals. Acta Materialia, 2008. **56**(18): p. 5158-5167.

[58] K. Sakaki, T. Kawase, M. Hirato, et al., The effect of hydrogen on vacancy generation in iron by plastic deformation. Scripta Materialia, 2006. **55**(11): p. 1031-1034.

[59] D. Xie, S. Li, M. Li, et al., Hydrogenated vacancies lock dislocations in aluminium. Nature communications, 2016. **7**(1): p. 1-7.

[60] A. Barnoush and H. Vehoff, Electrochemical nanoindentation: A new approach to probe

hydrogen/deformation interaction. Scripta Materialia, 2006. **55**(2): p. 195-198.

[61] M. Duarte, X. Fang, J. Rao, et al., In situ nanoindentation during electrochemical hydrogen charging: a comparison between front-side and a novel back-side charging approach. Journal of materials science, 2021: p. 1-13.

[62] R. Kirchheim, Solid solution softening and hardening by mobile solute atoms with special focus on hydrogen. Scripta Materialia, 2012. **67**(9): p. 767-770.

[63] R. B. Gupta, Hydrogen fuel: production, transport, and storage. 2008: CRC press.

[64] S. M. Myers, M. I. Baskes, H. K. Birnbaum, et al., Hydrogen interactions with defects in crystalline solids. Reviews of Modern Physics, 1992. **64**(2): p. 559-617.

[65] A. Sieverts, Die Löslichkeit von Wasserstoff in Kupfer, Eisen und Nickel. Zeitschrift fur Physikalische Chemie, 1911. **77**(1): p. 591-613.

[66] E. Dafft, K. Bohnenkamp, and H. Engell, Investigations of the hydrogen evolution kinetics and hydrogen absorption by iron electrodes during cathodic polarization. Corrosion Science, 1979. **19**(9): p. 591-612.

[67] L. Marchetti, E. Herms, P. Laghoutaris, et al., Hydrogen embrittlement susceptibility of tempered 9% Cr–1% Mo steel. International Journal of Hydrogen Energy, 2011. **36**(24): p. 15880-15887.

[68] F. Bao, E. Kemppainen, I. Dorbandt, et al., Understanding the Hydrogen Evolution Reaction Kinetics of Electrodeposited Nickel-Molybdenum in Acidic, Near-Neutral, and Alkaline Conditions. ChemElectroChem, 2021. **8**(1): p. 195-208.

[69] D. Wan, Y. Deng, J. I. H. Meling, et al., Hydrogen-enhanced fatigue crack growth in a single-edge notched tensile specimen under in-situ hydrogen charging inside an environmental scanning electron microscope. Acta Materialia, 2019. **170**: p. 87-99.

[70] Y. Deng, T. Hajilou, D. Wan, et al., In-situ micro-cantilever bending test in environmental scanning electron microscope: Real time observation of hydrogen enhanced cracking. Scripta Materialia, 2017. **127**: p. 19-23.

[71] V. Raja and T. Shoji, Stress corrosion cracking: theory and practice. 2011: Elsevier.

[72] J. Crank, The mathematics of diffusion. 1979: Oxford university press.

[73] A. Turnbull, Hydrogen diffusion and trapping in metals, in Gaseous HE of materials in energy technologies. 2012, Woodhead. p. 89-128.

[74] M. S. de Santa Maria and A. Turnbull, The effect of H2S concentration and pH on the cracking resistance of AISI 410 stainless steel in 5% brine. Corrosion Science, 1989. **29**(1): p. 69-88.

[75] E. Yagi, The state of hydrogen in Nb-based Nb-Mo alloys analyzed by the channelling method. ISIJ international, 2003. **43**(4): p. 505-513.

[76] J. P. Hirth, Effects of hydrogen on the properties of iron and steel. Metallurgical Transactions A, 1980. **11**(6): p. 861-890.

[77] T. Perng and C. Altstetter, Comparison of hydrogen gas embrittlement of austenitic and ferritic stainless steels. Metallurgical Transactions A, 1987. **18**(1): p. 123-134.

[78] A. San-Martin and F. Manchester, The Fe-H (iron-hydrogen) system. Bulletin of Alloy Phase Diagrams, 1990. **11**(2): p. 173-184.

[79] Y. Tateyama and T. Ohno, Stability and clusterization of hydrogen-vacancy complexes in $\alpha-$ Fe: an ab initio study. Physical Review B, 2003. **67**(17): p. 174105.

[80] M. J. ZEHETBAUER, G. Steiner, E. Schafler, et al. Deformation induced vacancies with severe plastic deformation: Measurements and modelling. in Materials Science Forum. 2006. Trans Tech Publ.

[81] W. Krieger, S. V. Merzlikin, A. Bashir, et al., Spatially resolved localization and characterization of trapped hydrogen in zero to three dimensional defects inside ferritic steel. Acta Materialia, 2018. **144**: p. 235-244.

[82] G. Lu and E. Kaxiras, Hydrogen embrittlement of aluminum: the crucial role of vacancies. Physical Review Letters, 2005. **94**(15): p. 155501.

[83] R. Kirchheim, Solid Solutions of Hydrogen in Complex Materials. Solid State Physics, 2004. **59**: p. 203-291.

[84] R. Kirchheim, Interaction of hydrogen with dislocations in palladium—I. Activity and

diffusivity and their phenomenological interpretation. Acta Metallurgica, 1981. **29**(5): p. 835-843.

[85] R. Kirchheim, Interaction of hydrogen with dislocations in palladium—II. Interpretation of activity results by a fermi-dirac distribution. Acta Metallurgica, 1981. **29**(5): p. 845-853.

[86] K. Ono and M. Meshii, Hydrogen detrapping from grain boundaries and dislocations in high purity iron. Acta metallurgica et materialia, 1992. **40**(6): p. 1357-1364.

[87] W. Xie, X. Liu, W. Chen, et al., Hydrogen hardening effect in heavily deformed single crystal α-Fe. Computational Materials Science, 2011.

[88] J. Song and W. A. Curtin, Mechanisms of hydrogen-enhanced localized plasticity: An atomistic study using α-Fe as a model system. Acta Materialia, 2014. **68**: p. 61-69.

[89] Y. A. Du, L. Ismer, J. Rogal, et al., First-principles study on the interaction of H interstitials with grain boundaries in α-and γ-Fe. Physical Review B, 2011. **84**(14): p. 144121.

[90] Y. A. Du, J. Rogal, and R. Drautz, Diffusion of hydrogen within idealized grains of bcc Fe: A kinetic Monte Carlo study. Physical Review B, 2012. **86**(17): p. 174110.

[91] T. Ohmisawa, S. Uchiyama, and M. Nagumo, Detection of hydrogen trap distribution in steel using a microprint technique. Journal of alloys compounds, 2003. **356**: p. 290-294.

[92] E. J. McEniry, T. Hickel, and J. Neugebauer, Hydrogen behaviour at twist {110} grain boundaries in α-Fe. Philosophical Transactions of the Royal Society A: Mathematical, Physical Engineering Sciences, 2017. **375**(2098): p. 20160402.

[93] A. Oudriss, S. Le Guernic, Z. Wang, et al., Meso-scale anisotropic hydrogen segregation near grain-boundaries in polycrystalline nickel characterized by EBSD/SIMS. Materials Letters, 2016. **165**: p. 217-222.

[94] E. Legrand, J. Bouhattate, X. Feaugas, et al., Numerical analysis of the influence of scale effects and microstructure on hydrogen diffusion in polycrystalline aggregates. Computational Materials Science, 2013. **71**: p. 1-9.

[95] M. Hallil, A. Metsue, A. Oudriss, et al., Some Advances on Antagonist Effects of Grain Boundaries between the Trapping Process and the Fast Diffusion Path Investigated on Nickel

Bicrystals. Research Square, 2021.

[96] A. Pedersen and H. Jonsson, Simulations of hydrogen diffusion at grain boundaries in aluminum. Acta Materialia, 2009. **57**(14): p. 4036-4045.

[97] S. K. Sharma, D. S. Verma, L. U. Khan, et al., Handbook of materials characterization. 2018: Springer.

[98] N. M. Pirozzi, J. P. Hoogenboom, and B. N. Giepmans, ColorEM: analytical electron microscopy for element-guided identification and imaging of the building blocks of life. Histochemistry cell biology, 2018. **150**(5): p. 509-520.

[99] R. Armstrong, B. L. Adams, and M. A. Arnold, ASM Handbook Volume 10 Materials Characterization. 2018, ASM International.

[100] M. Koyama, D. Yamasaki, T. Nagashima, et al., In situ observations of silver-decoration evolution under hydrogen permeation: Effects of grain boundary misorientation on hydrogen flux in pure iron. Scripta Materialia, 2017. **129**: p. 48-51.

[101] J. Ovejero-García, Hydrogen microprint technique in the study of hydrogen in steels. Journal of materials science, 1985. **20**(7): p. 2623-2629.

[102] C. Jones, V. Tuli, Z. Shah, et al., Evidence of hydrogen trapping at second phase particles in zirconium alloys. Scientific reports, 2021. **11**(1): p. 1-12.

[103] R. Ishikawa, E. Okunishi, H. Sawada, et al., Direct imaging of hydrogen-atom columns in a crystal by annular bright-field electron microscopy. Nature materials, 2011. **10**(4): p. 278-281.

[104] S. Evers, C. Senoz, and M. Rohwerder, Hydrogen detection in metals: a review and introduction of a Kelvin probe approach. Science and Technology of Advanced Materials, 2013. **14**(1): p. 014201.

[105] C.-H. Wu, W. Krieger, and M. Rohwerder, On the robustness of the Kelvin probe based potentiometric hydrogen electrode method and its application in characterizing effective hydrogen activity in metal: 5 wt. % Ni cold-rolled ferritic steel as an example. Science and Technology of Advanced Materials, 2019. **20**(1): p. 1073-1089.

[106] E. J. Song, D.-W. Suh, and H. K. D. H. Bhadeshia, Theory for hydrogen desorption in ferritic steel. Computational Materials Science, 2013. **79**: p. 36-44.

[107] M. Devanathan and Z. Stachurski, The adsorption and diffusion of electrolytic hydrogen in palladium. Proceedings of the Royal Society of London. Series A., 1962. **270**(1340): p. 90-102.

[108] S. Evers, C. Senöz, and M. Rohwerder, Spatially resolved high sensitive measurement of hydrogen permeation by scanning Kelvin probe microscopy. Electrochimica Acta, 2013. **110**: p. 534-538.

[109] S. Evers and M. Rohwerder, The hydrogen electrode in the "dry": A Kelvin probe approach to measuring hydrogen in metals. Electrochemistry Communications, 2012. **24**: p. 85-88.

[110] C. Senöz, S. Evers, M. Stratmann, et al., Scanning Kelvin Probe as a highly sensitive tool for detecting hydrogen permeation with high local resolution. Electrochemistry Communications, 2011. **13**(12): p. 1542-1545.

[111] A. G148-97, Standard practice for evaluation of hydrogen uptake, permeation, and transport in metals by an electrochemical technique. ASTM International, 2011. **1**: p. 1-10.

[112] M. Koyama, A. Bashir, M. Rohwerder, et al., Spatially and kinetically resolved mapping of hydrogen in a twinning-induced plasticity steel by use of scanning Kelvin probe force microscopy. Journal of the Electrochemical Society, 2015. **162**(12): p. C638.

[113] B. Sun, W. Krieger, M. Rohwerder, et al., Dependence of hydrogen embrittlement mechanisms on microstructure-driven hydrogen distribution in medium Mn steels. Acta Materialia, 2020. **183**: p. 313-328.

[114] D. Wan, Y. Deng, and A. Barnoush, Hydrogen embrittlement effect observed by in-situ hydrogen plasma charging on a ferritic alloy. Scripta Materialia, 2018. **151**: p. 24-27.

[115] A. Barnoush and H. Vehoff, In situ electrochemical nanoindentation: A technique for local examination of hydrogen embrittlement. Corrosion Science, 2008. **50**(1): p. 259-267.

[116] A. Barnoush, N. Kheradmand, and T. Hajilou, Correlation between the hydrogen chemical potential and pop-in load during in situ electrochemical nanoindentation. Scripta

Materialia, 2015. **108**: p. 76-79.

[117] T. Hajilou, M. S. B. Hope, A. H. Zavieh, et al., In situ small-scale hydrogen embrittlement testing made easy: An electrolyte for preserving surface integrity at nano-scale during hydrogen charging. International Journal of Hydrogen Energy, 2018. **43**(27): p. 12516-12529.

[118] A. S. Ebner, S. Brinckmann, E. Plesiutschnig, et al., A Modified Electrochemical Nanoindentation Setup for Probing Hydrogen-Material Interaction Demonstrated on a Nickel-Based Alloy. Jom: The Journal of The Minerals, 2020.

[119] D. Wang, X. Lu, D. Wan, et al., In-situ observation of martensitic transformation in an interstitial metastable high-entropy alloy during cathodic hydrogen charging. Scripta Materialia, 2019. **173**: p. 56-60.

[120] A. Barnoush and H. Vehoff, Hydrogen embrittlement of aluminum in aqueous environments examined by in situ electrochemical nanoindentation. Scripta Materialia, 2008. **58**(9): p. 747-750.

[121] A. Ahmadian, D. Scheiber, X. Zhou, et al., Aluminum depletion induced by co-segregation of carbon and boron in a bcc-iron grain boundary. Nature communications, 2021. **12**(1): p. 1-11.

[122] M. Smialowski, Hydrogen in steel: effect of hydrogen on iron and steel during production, fabrication, and use. 2014: Elsevier.

[123] A. Atrens, Q. Liu, C. Tapia-Bastidas, et al., Influence of Hydrogen on Steel Components for Clean Energy. Corrosion and Materials Degradation, 2018. **1**(1): p. 3-26.

[124] Q. Liu and A. Atrens, A critical review of the influence of hydrogen on the mechanical properties of medium-strength steels. Corrosion Reviews, 2013. **31**(3-6): p. 85-103.

[125] W. C. Oliver and G. M. Pharr, An improved technique for determining hardness and elastic modulus using load and displacement sensing indentation experiments. Journal of Materials Research, 1992. **7**(6): p. 1564-1583.

[126] W. C. Oliver and G. M. Pharr, Measurement of hardness and elastic modulus by instrumented indentation: Advances in understanding and refinements to methodology. Journal

of Materials Research, 2004. **19**(1): p. 3-20.

[127] A. C. Fischer-Cripps and D. W. Nicholson, Nanoindentation. Mechanical engineering series. Applied Mechanics Reviews, 2004. **57**(2): p. 37.

[128] K. Durst and V. Maier, Dynamic nanoindentation testing for studying thermally activated processes from single to nanocrystalline metals. Current Opinion in Solid State and Materials Science, 2015. **19**(6): p. 340-353.

[129] V. Maier-Kiener and K. Durst, Advanced nanoindentation testing for studying strain-rate sensitivity and activation volume. Jom: The Journal of The Minerals, 2017. **69**(11): p. 2246-2255.

[130] B. Lucas and W. Oliver, Indentation power-law creep of high-purity indium. Metallurgical Materials Transactions A, 1999. **30**(3): p. 601-610.

[131] V. Gaspard, G. Kermouche, D. Delafosse, et al., Hydrogen effect on dislocation nucleation in a ferritic alloy Fe–15Cr as observed per nanoindentation. Materials Science and Engineering: A, 2014. **604**: p. 86-91.

[132] A. Montagne, V. Audurier, and C. Tromas, Influence of pre-existing dislocations on the pop-in phenomenon during nanoindentation in MgO. Acta Materialia, 2013. **61**(13): p. 4778-4786.

[133] J. Rao, S. Lee, G. Dehm, et al., Hardening effect of diffusible hydrogen on BCC Fe-based model alloys by in situ backside hydrogen charging. Materials & Design, 2023: p. 112143.

[134] C.-H. Wu, The Principle and Applications of Scanning Kelvin Probe Based Hydrogen Detection Technique on Pd-coated and Oxide Covered Surface. 2019, Fakultät für Maschinenbau, Ruhr-Universität-Bochum Bochum, Germany.

[135] J. Manoj Prabhakar, A. de Vooys, and M. Rohwerder, In situ microscopic investigation of ion migration on the surface of chromium coated steels. npj Materials Degradation, 2022. **6**(1): p. 1-13.

[136] T. Malis, S. Cheng, and R. Egerton, EELS log-ratio technique for specimen-thickness measurement in the TEM. Journal of electron microscopy technique, 1988. **8**(2): p. 193-200.

[137] J. Schindelin, I. Arganda-Carreras, E. Frise, et al., Fiji: an open-source platform for biological-image analysis. Nature methods, 2012. **9**(7): p. 676-682.

[138] G. C. Sneddon, P. W. Trimby, and J. M. Cairney, Transmission Kikuchi diffraction in a scanning electron microscope: A review. Materials Science Engineering: R, 2016. **110**: p. 1-12.

[139] N. Fairley, V. Fernandez, M. Richard-Plouet, et al., Systematic and collaborative approach to problem solving using X-ray photoelectron spectroscopy. Applied Surface Science Advances, 2021. **5**: p. 100112.

[140] R. Andreas, S. Oded, H. Hannu, et al., In-situ ToF-SIMS analyses of deuterium re-distribution in austenitic steel AISI 304L under mechanical load. Scientific Reports (Nature Publisher Group), 2020. **10**(1).

[141] Y. Zhao, D.-H. Lee, M.-Y. Seok, et al., Resistance of CoCrFeMnNi high-entropy alloy to gaseous hydrogen embrittlement. Scripta Materialia, 2017. **135**: p. 54-58.

[142] Y. Zhao, J.-M. Park, D.-H. Lee, et al., Influences of hydrogen charging method on the hydrogen distribution and nanomechanical properties of face-centered cubic high-entropy alloy: A comparative study. Scripta Materialia, 2019. **168**: p. 76-80.

[143] A. Massone, A. Manhard, W. Jacob, et al., An SEM compatible plasma cell for in situ studies of hydrogen-material interaction. Review of Scientific Instruments, 2020. **91**(4): p. 043705.

[144] N. Kheradmand, R. Johnsen, J. S. Olsen, et al., Effect of hydrogen on the hardness of different phases in super duplex stainless steel. International Journal of Hydrogen Energy, 2016. **41**(1): p. 704-712.

[145] D. Wang, X. Lu, Y. Deng, et al., Effect of hydrogen on nanomechanical properties in Fe-22Mn-0.6C TWIP steel revealed by in-situ electrochemical nanoindentation. Acta Materialia, 2019. **166**: p. 618-629.

[146] A. Barnoush, M. Asgari, and R. Johnsen, Resolving the hydrogen effect on dislocation nucleation and mobility by electrochemical nanoindentation. Scripta Materialia, 2012. **66**(6): p. 414-417.

[147] M. Zamanzade, H. Vehoff, and A. Barnoush, Cr effect on hydrogen embrittlement of Fe3Al-based iron aluminide intermetallics: Surface or bulk effect. Acta Materialia, 2014. **69**: p. 210-223.

[148] G. Stenerud, R. Johnsen, J. S. Olsen, et al., Effect of hydrogen on dislocation nucleation in alloy 718. International Journal of Hydrogen Energy, 2017. **42**(24): p. 15933-15942.

[149] S. Asano, Y. Nishino, and R. Otuska, Lattice Hardening and Anomalous Softening of Iron and Steel Caused by Electrolytic Hydrogen Charging. Journal of the Japan Institute of Metals, 1979. **43**(3): p. 241-248.

[150] M. C. Biesinger, B. P. Payne, A. P. Grosvenor, et al., Resolving surface chemical states in XPS analysis of first row transition metals, oxides and hydroxides: Cr, Mn, Fe, Co and Ni. Applied Surface Science, 2011. **257**(7): p. 2717-2730.

[151] Y. Liao, Practical electron microscopy and database. 2006, Global Sino.

[152] K.-E. Thelning, Steel and its heat treatment. 2013: Butterworth-heinemann.

[153] M. Maalekian, The effects of alloying elements on steels (I). 2007.

[154] C. Heintze, F. Bergner, and M. Hernández-Mayoral, Ion-irradiation-induced damage in Fe–Cr alloys characterized by nanoindentation. Journal of Nuclear Materials, 2011. **417**(1-3): p. 980-983.

[155] D. Caillard, A TEM in situ study of alloying effects in iron. II—Solid solution hardening caused by high concentrations of Si and Cr. Acta Materialia, 2013. **61**(8): p. 2808-2827.

[156] M. Matijasevic and A. Almazouzi, Effect of Cr on the mechanical properties and microstructure of Fe–Cr model alloys after n-irradiation. Journal of Nuclear Materials, 2008. **377**(1): p. 147-154.

[157] K. Durst, B. Backes, O. Franke, et al., Indentation size effect in metallic materials: Modeling strength from pop-in to macroscopic hardness using geometrically necessary dislocations. Acta Materialia, 2006. **54**(9): p. 2547-2555.

[158] K. L. Johnson, Contact Mechanics, ninth printing. 2003, Cambridge University Press.

[159] M. M. Biener, J. Biener, A. M. Hodge, et al., Dislocation nucleation in bcc Ta single

crystals studied by nanoindentation. Physical Review B, 2007. **76**(16): p. 165422.

[160] W. D. Nix and H. Gao, Indentation size effects in crystalline materials: a law for strain gradient plasticity. Journal of the Mechanics and Physics of Solids, 1998. **46**(3): p. 411-425.

[161] W. S. Choi, B. C. De Cooman, S. Sandlöbes, et al., Size and orientation effects in partial dislocation-mediated deformation of twinning-induced plasticity steel micro-pillars. Acta Materialia, 2015. **98**: p. 391-404.

[162] J. Rosenberg and H. Piehler, Calculation of the Taylor factor and lattice rotations for bcc metals deforming by pencil glide. Metallurgical Transactions B, 1971. **2**(1): p. 257-259.

[163] G. I. Taylor, The mechanism of plastic deformation of crystals. Part I.—Theoretical. Proceedings of the Royal Society of London. Series A, 1934. **145**(855): p. 362-387.

[164] X. Qiu, Y. Huang, W. Nix, et al., Effect of intrinsic lattice resistance in strain gradient plasticity. Acta Materialia, 2001. **49**(19): p. 3949-3958.

[165] G. Ghosh and G. Olson, The isotropic shear modulus of multicomponent Fe-base solid solutions. Acta Materialia, 2002. **50**(10): p. 2655-2675.

[166] S. Zaefferer and N.-N. Elhami, Theory and application of electron channelling contrast imaging under controlled diffraction conditions. Acta Materialia, 2014. **75**: p. 20-50.

[167] C. Woodcock, D. Bahr, and N. J. Moody, Plastic zone development around nanoindentations. MRS Online Proceedings Library, 2000. **649**: p. Q7. 14.

[168] K. Durst, B. Backes, and M. Göken, Indentation size effect in metallic materials: Correcting for the size of the plastic zone. Scripta Materialia, 2005. **52**(11): p. 1093-1097.

[169] H. Hagi and Y. Hayashi, Effects of interstitial impurities on dislocation trapping of hydrogen in iron. Transactions of the Japan institute of metals, 1987. **28**(5): p. 375-382.

[170] B. H. K. D. Hansraj, Prevention of hydrogen embrittlement in steels. ISIJ international, 2016. **56**(1): p. 24-36.

[171] D. P. Abraham and C. J. Altstetter, The effect of hydrogen on the yield and flow stress of an austenitic stainless steel. Metallurgical and Materials transactions A, 1995. **26**(11): p. 2849-2858.

[172] R. Oriani and P. Josephic, Effects of hydrogen on the plastic properties of medium-Carbon steels. Metallurgical Transactions A, 1980. **11**(11): p. 1809-1820.

[173] P. M. Anderson, J. P. Hirth, and J. Lothe, Theory of dislocations. 2017: Cambridge University Press.

[174] P. El Ters and M. A. Shehadeh, Modeling the temperature and high strain rate sensitivity in BCC iron: Atomistically informed multiscale dislocation dynamics simulations. International Journal of Plasticity, 2019. **112**: p. 257-277.

[175] K. Oguri, S. Takaki, and H. Kimura, Hydrogen-induced softening and hardening in high purity Fe-C alloys. Materials Science and Engineering, 1982. **53**(2): p. 223-232.

[176] L. Pauling, The Nature of the Chemical Bond. Vol. 260. 1960: Cornell university press Ithaca, NY.

[177] V. P. Ramunni, C. Hurtado-Noreña, and P. Bruzzoni, Ab-initio approach to study hydrogen diffusion in 9Cr steels. Physica B: Condensed Matter, 2012. **407**(16): p. 3301-3304.

[178] A. Shirley and C. Hall, Trapping of hydrogen by substitutional and interstitial impurities in α-iron. Scripta Metallurgica, 1983. **17**(8): p. 1003-1008.

[179] D. Jiang and E. A. Carter, Diffusion of interstitial hydrogen into and through bcc Fe from first principles. Physical Review B, 2004. **70**(6): p. 064102.

[180] N. Barakat, Hydrogen permeation through low alloy steels. 2009, Heriot-Watt University.

[181] S. K. Lawrence, B. P. Somerday, M. D. Ingraham, et al., Probing the effect of hydrogen on elastic properties and plastic deformation in nickel using nanoindentation and ultrasonic methods. Jom: The Journal of The Minerals, 2018. **70**(7): p. 1068-1073.

[182] N. Paton, O. Buck, and J. Williams, Effect of hydrogen on the strength modulus and lattice parameter of a Ti--Mo alloy. Scripta Metallurgica, 1975. **9**(6): p. 687-691.

[183] E. Fisher, D. Westlake, and S. Ockers, Effects of hydrogen and oxygen on the elastic moduli of vanadium, niobium, and tantalum single crystals. Physica status solidi (a), 1975. **28**(2): p. 591-602.

[184] U. Hadam and T. Zakroczymski, Absorption of hydrogen in tensile strained iron and high-carbon steel studied by electrochemical permeation and desorption techniques. International Journal of Hydrogen Energy, 2009. **34**(5): p. 2449-2459.

[185] T.-Y. Zhang, F.-X. Jiang, W.-Y. Chu, et al., Effect of hydrogen on the Young's modulus of iron. Metallurgical Transactions A, 1985. **16**(9): p. 1655-1662.

[186] S. Frappart, X. Feaugas, J. Creus, et al., Hydrogen solubility, diffusivity and trapping in a tempered Fe–C–Cr martensitic steel under various mechanical stress states. Materials Science and Engineering: A, 2012. **534**: p. 384-393.

[187] A. Turnbull, Perspectives on hydrogen uptake, diffusion and trapping. International Journal of Hydrogen Energy, 2015. **40**(47): p. 16961-16970.

[188] I. Peñalva, G. Alberro, J. Aranburu, et al., Influence of the Cr content on the permeation of hydrogen in Fe alloys. Journal of Nuclear Materials, 2013. **442**(1-3): p. S719-S722.

[189] H. Hagi, Effect of substitutional alloying elements (Al, Si, V, Cr, Mn, Co, Ni, Mo) on diffusion coefficient of hydrogen in α-iron. Materials Transactions, JIM, 1992. **33**(5): p. 472-479.

[190] I. Peñalva, G. Alberro, F. Legarda, et al., Influence of Cr content on the diffusive transport parameters and trapping of hydrogen in Fe alloys. Fusion Engineering and Design, 2014. **89**(7-8): p. 1628-1632.

[191] T. Depover and K. Verbeken, The detrimental effect of hydrogen at dislocations on the hydrogen embrittlement susceptibility of Fe-CX alloys: An experimental proof of the HELP mechanism. International Journal of Hydrogen Energy, 2018. **43**(5): p. 3050-3061.

[192] B. Malard, B. Remy, C. Scott, et al., Hydrogen trapping by VC precipitates and structural defects in a high strength Fe–Mn–C steel studied by small-angle neutron scattering. Materials Science Engineering: A, 2012. **536**: p. 110-116.

[193] A. Díaz, I. Cuesta, E. Martinez-Pañeda, et al., Analysis of hydrogen permeation tests considering two different modelling approaches for grain boundary trapping in iron. International Journal of Fracture, 2020. **223**(1): p. 17-35.

[194] R. Shi, Y. Ma, Z. Wang, et al., Atomic-scale investigation of deep hydrogen trapping in

NbC/α-Fe semi-coherent interfaces. Acta Materialia, 2020. **200**: p. 686-698.

[195] S. Frappart, A. Oudriss, X. Feaugas, et al., Hydrogen trapping in martensitic steel investigated using electrochemical permeation and thermal desorption spectroscopy. Scripta Materialia, 2011. **65**(10): p. 859-862.

[196] X. Lu and D. Wang, Effect of hydrogen on deformation behavior of Alloy 725 revealed by in-situ bi-crystalline micropillar compression test. Journal of Materials Science & Technology, 2021. **67**: p. 243-253.

[197] X. Fang, M. Rasinski, A. Kreter, et al., Plastic deformation of tungsten due to deuterium plasma exposure: Insights from micro-compression tests. 2019. **162**: p. 132-135.

[198] M. Deutges, I. Knorr, C. Borchers, et al., Influence of hydrogen on the deformation morphology of vanadium (100) micropillars in the a-phase of the vanadium–hydrogen system. Scripta Materialia, 2013. **68**: p. 71-74.

[199] A. Oudriss, J. Creus, J. Bouhattate, et al., Grain size and grain-boundary effects on diffusion and trapping of hydrogen in pure nickel. Acta Materialia, 2012. **60**(19): p. 6814-6828.

[200] Z. Wang, T. Sun, H. Zhang, et al., The interaction between grain boundary and tool geometry in nanocutting of a bi-crystal copper. International Journal of Extreme Manufacturing, 2019. **1**(4): p. 045001.

[201] S.-W. Liang, R.-Z. Qiu, and T.-H. J. B. J. o. N. Fang, Molecular dynamics simulations of nanoindentation and scratch in Cu grain boundaries. 2017. **8**(1): p. 2283-2295.

Curriculum Vitae

Personal information

Date of birth: 23. Oct. 1993

E-mail: raojing1023@gmail.com

Education

Oct. 2017 - Present	**Ruhr-Universität Bochum, Germany**
	Max-Planck-Institut für Eisenforschung GmbH (MPIE), Germany
	Ph.D. candidate (expected graduation date: Apr. 2022):
	Hydrogen mechanics and interfaces Group, Department of Structure an
	Nano-/Micromechanics of Materials
Oct. 2013 - Dec. 2016	**RWTH Aachen University, Germany**
	M.Sc.: Materials Science of Steel, Metallurgical Engineering
	GPA: 1.60/1.0
Sep. 2009 - Jun. 2013	**University of Science and Technology Beijing (USTB), China**
	B.Sc.: Metallurgical Engineering
	GPA: 90.6/100 (1.70/1.0)
	RANK: Top 3 out of 230

Research experience

Oct. 2017 - Present   **Hydrogen effects on the mechanical response of bcc Fe-Cr alloys by in-situ nanoindentation (Ph.D. dissertation)**

Max-Planck-Institut für Eisenforschung GmbH (MPIE), Düsseldorf, Germany;

- Actively participate in developing an innovative in-situ nanoindentation set-up, which can electrochemically charge metals with hydrogen from the backside and collect mechanical data simultaneously (G200).

- Hydrogen-induced hardening of FeCr alloy was observed in nanoindentation, microscratch and micropillar compression tests. The hardening effect was attributed to the hydrogen-assisted increase of dislocation density, which was verified by SEM and TEM analysis.

Jun. 2016 - Dec. 2016	**Study of the local mechanical properties and plasticity mechanisms in a Zn-Al eutectic alloy (Master thesis 1.3/1.0)**
	Institut für Metallkunde und Metallphysik (IMM), RWTH Aachen University, Aachen, Germany;
	• The mechanical properties and microstructure evolution of a Zn-4Al-1Cu-0.3Mg alloy at different temperatures and strain rates were investigated using two nanoindentation machines.
Feb. 2015 - May. 2015	**The influence of the heating rate during ART-annealing on the microstructure and mechanical properties of medium Mn steel Fe-0.2C-5Mn (Study integrated thesis 1.3/1.0)**
	Institut für Eisenhüttenkunde (IEHK), RWTH Aachen University, Aachen, Germany;
	• Based on experimental results of tensile tests and in-situ synchrotron X-ray diffraction (XRD), the influence of heating rate on mechanical properties and microstructure evolution during ART-annealing of medium Mn steel was quantitatively investigated.
Nov. 2012 - Jun. 2013	**Study of electrochemical deposition of branched hierarchical ZnO nanorod arrays on stainless steel mesh to improve photo-electric transformation efficiency of dye-sensitized solar cell (Bachelor thesis)**
	School of Metallurgical and Ecological Engineering, University of Science and Technology Beijing (USTB), Beijing, China;
	• The structure of hierarchical ZnO nanorod arrays on stainless steel mesh has been studied and investigated (SEM, XRD).

Publications

2023	**J. Rao**, C. Wu, M. Rohwerder, G. Dehm, M. J. Duarte. Comparison of the hydrogen diffusion coefficient in FeCr alloy by the Kelvin probe based potentiometric hydrogen electrode method and in situ nanoindentation. (in preparation)
2023	**J. Rao**, S. Lee, G. Dehm, M. J. Duarte. Diffusible hydrogen and its impact on nanohardness in FeCr alloys by in situ nanoindentation, *Materials & Design* (2023)
2023	G. Wu, S. Liu, Q. Wang, **J. Rao**, W. Xia, Y. Yan, J. Eckert, C. Liu. Substantially enhanced homogeneous plastic flow in hierarchically nanodomained amorphous alloys, *Nature communications* (2023)

2021	G. Wu, C. Liu, A. Brognara, M. Ghidelli, Y. Bao, S. Liu, X. Wu, W. Xia, H. Zhao, **J. Rao**, D. Ponge, V. Devulapalli, W. Lu, G. Dehm, D. Raabe, Z. Li. Symbiotic crystal-glass alloys via dynamic chemical partitioning, *Materials Today* 51 (2021) 6-14.
2021	M. J. Duarte, X. Fang, **J. Rao**, W. Krieger, S. Brinckmann, & G. Dehm. In situ nanoindentation during electrochemical hydrogen charging: a comparison between front-side and a novel backside charging approach. *Journal of Materials Science* 56.14 (2021): 8732-8744.
2018	Z. Wu, S. Sandlöbes, **J. Rao**, J. S. L. Gibson, B. Berkels, & S. Korte-Kerzel. Local mechanical properties and plasticity mechanisms in a Zn-Al eutectic alloy. *Materials & Design* 157 (2018): 337-350.

Conferences

2022 poster presentation	"Hydrogen induced hardening effect and the diffusion behavior in bcc FeCr alloys by in situ nanoindentation". Nanomechanical Testing in Materials Research and Development VIII (ECI2022), online
2022 oral presentation	"Hydrogen-induced hardening effect and microstructure evolution in FeCr alloys by in situ nanoindentation". Materials Science and Engineering Conference (MSE2022), online
2022 oral presentation	"The Effect of chemical composition on the Hydrogen diffusion coefficient in Ferritic Fecr Alloys: A Comparison between the Kelvin Probe-Based Potentiometric Hydrogen Electrode Method and a Nanohardness Based Method". 18th International Conference on Diffusion in Solids and Liquids (DSL2022), online
2022 oral presentation	"Diffusible hydrogen and its impact on nanohardness and dislocation structure in Fe-Cr alloys by in-situ nanoindentation". TMS 2022 Annual Meeting & Exhibition (TMS2022), online
2021 oral presentation	"Hydrogen effects on the mechanical response of bcc Fe-Cr alloys by in-situ nanoindentation". 17th International Conference on Diffusion in Solids and Liquids (DSL2021), online.
2020 oral presentation	"Hydrogen effects on the mechanical response of bcc Fe-Cr alloys by in-situ nanoindentation". Materials Science and Engineering Conference (MSE2020), online.
2019 poster presentation	"Hydrogen-microstructure interactions in binary Fe-Cr alloys at small scale". International Workshop on Advanced and In situ

	Microscopies of Functional Nanomaterials and Devices (IAMNano2019), Düsseldorf, Germany.
2019 poster presentation	"Hydrogen-microstructure interactions investigation in binary Fe-Cr alloys at small scale". European Congress and Exhibition on Advanced Materials and Processes 2019 (EUROMAT2019), Stockholm, Sweden.

Internship

May. 2015 - Sep. 2015	**Forschungszentrum Jülich GmbH (FZJ), Germany;** Investigation of correlation between mechanical creep properties and microstructure in high Cr steel by compressive and uniaxial creep tests.
Jun. 2012 - Jul. 2012	**Nr.5 mineral Steel Group Company, Qianan, China** Study and practice in the Basic Oxygen Furnace, Ladle Furnace and Continuous Casting sections.
Jun. 2011 - Jul. 2011	**Shougang Qinhuangdao Steel Company, Qinhuangdao, China** Study and practice in the Sintering, Pelleting and Blast Furnace sections.